# Understanding Live Pole Drains

An open-air laboratory study of the hydrological behaviour of Live Pole Drains

L.C. (Lucas) de Leeuw



# Understanding Live Pole Drains

## An open-air laboratory study of the hydrological behaviour of Live Pole Drains

L.C. (Lucas) de Leeuw

To obtain the degree of Master of Science
at the Delft University of Technology,

to be defended publicly on Friday April 17, 2026.


| | |
|---|---|
| Text: | Lucas de Leeuw |
| Track: | Water Resources Engineering |
| Student number: | 5107318 |
| Main supervisor: | Prof.dr. T.A. Bogaard |
| Second supervisor: | Dr.ir. J.A. van der Werf |
| Additional supervisor: | PhD Candidate F. Berlitz |
| Project Duration: | October, 2025 - April, 2026 |
| Faculty: | Faculty of Civil Engineering and Geosciences |


TU Delft

# Acknowledgements

With this thesis I conclude my master's in Water Resources Engineering. It turned out to be a fitting end to the degree, bringing together instrument design, fieldwork, and the more philosophical side of hydrology that I hope to keep exploring. But what made it truly enjoyable were the people I got to share it with, and I would like to take a moment to thank them here.

My first thanks go to my supervisors, Prof. Dr. Thom Bogaard, Dr. Ir. Job van der Werf, and Fernanda Berlitz.

Thom, thank you for sharing your deep expertise in hydrology and for showing me how seemingly simple field experiments can illuminate the fundamentals of groundwater flow. Your guidance taught me to balance enthusiasm about findings with the rigour that groundwater fundamentals demand, and to recognise the misunderstandings that are easy to fall into. I am also grateful for the energy you brought to the practical side of the work, making even winter fieldwork, with its headtorches and fan heaters, something to look forward to.

Job, thank you for your valuable, actionable feedback on experimental design, and for leaving room for curiosity, which led to the development of the siphonic flow meter based on your initial idea. I am equally grateful for your open door and for the brainstorming sessions and quick visits that were a real source of momentum throughout the project.

Fernanda, thank you for your help in the field, your support in getting me set up in the lab, and the critical questions and attention to detail that pushed me to be more precise. Thank you also for the broader guidance on navigating a thesis, from writing and design to keeping overview and progress on track.

I would also like to thank Jean-Paul de Garde for welcoming me at the Green Village and Flood Proof Holland. And a thank you to Bokuretsion Estifanos from the waterlab for helping me find and obtain all the materials required for the fieldwork.

Lastly, I want to thank my friends, family and housemates who made the past half year very fulfilling. I'd do it again.

*L.C. (Lucas) de Leeuw*
*Delft, April 2026*

# Abstract

Shallow landslides impact people worldwide and are projected to intensify under future climate conditions, leaving slopes vulnerable to further erosion and recurrent failure. Soil bioengineering, a category of Nature-based Solutions (NbS), offers a promising approach to both stabilising and restoring such slopes, but lacks the empirical evidence needed for widespread implementation. This study focuses on Live Pole Drains (LPD), bundles of willow branches installed in slopes to promote subsurface drainage while sprouting to initiate revegetation. While predominantly documented as a measure against superficial erosion, LPD have also been proposed as a measure against shallow landslides, though empirical evidence remains scarce. The central aim was to develop an evidence-based conceptual model of LPD hydrological behaviour, advancing from qualitative perceptual models through experimental investigation. This was carried out using an Open-Air Laboratory (OAL) approach at Flood Proof Holland in Delft, the Netherlands.

Three experiments were conducted: two in which a controlled flux was applied to isolate specific hydrological processes, and one infiltration experiment assessing the lumped effect of LPD on infiltration. The resulting conceptual model characterises LPD as threshold-dependent lateral drains that simultaneously enhance infiltration capacity through root-driven improvements to soil structure. In the current setup, situated above a permeable sand layer, the drainage threshold was rarely met, indicating that the effectiveness of LPD as a slope drainage measure is conditional on the surrounding soil's hydraulic properties. The sandy base layer facilitated generalisation of the underlying processes but prevented the conditions required for full LPD activation.

Future research in settings with a lower-conductance base layer is needed to demonstrate LPD effectiveness under the conditions in which they are intended to operate, with the determination of the activation threshold as an explicit objective. As an additional contribution, a novel siphonic flow meter was developed for low-cost flow measurement within the OAL framework, though further development is required for reliable use under continuous inflow conditions.

# Contents

**Acknowledgements** i

**Abstract** ii

**1 Introduction** 1
- 1.1 Bioengineering as a Nature-based Solution . . . 1
- 1.2 Live Pole Drains . . . 1
- 1.3 Open-Air Laboratories . . . 2
- 1.4 Research objective . . . 3
- 1.5 Thesis outline . . . 4

**2 Perceptual models** 5
- 2.1 Perceptual Model 1 (PM1) . . . 6
- 2.2 Perceptual Model 2 (PM2): Vertical preferential drainage . . . 6
- 2.3 Perceptual Model 3 (PM3): Conditional lateral redistribution under sustained wetness . . . 6
- 2.4 Perceptual Model 4 (PM4) . . . 7

**3 Open-air laboratory setup: configuration and instrumentation** 8
- 3.1 Sensor placement . . . 9
- 3.2 Percolation and LPD drains . . . 10
- 3.3 Weather conditions . . . 10

**4 Point injection into bundles: initial drainage pathway assessment** 11
- 4.1 Hypothesis . . . 11
- 4.2 Methodology . . . 11
- 4.3 Results . . . 13
  - 4.3.1 Flow through drain(s) . . . 13
  - 4.3.2 Soil moisture data . . . 14
  - 4.3.3 Water balance . . . 15
- 4.4 Discussion . . . 16
- 4.5 Conclusion and outlook . . . 19

**5 Six-Day distributed irrigation: response under sustained wetness** 20
- 5.1 Hypothesis . . . 20
- 5.2 Methodology . . . 20
  - 5.2.1 Flux . . . 21
  - 5.2.2 Irrigation . . . 22
- 5.3 Results . . . 23
  - 5.3.1 Water balance . . . 24
- 5.4 Discussion . . . 25
  - 5.4.1 Sensitivity water balance. . . . 27
- 5.5 Conclusion and outlook . . . 28

**6 Mini-Disk Infiltrometer measurements: impacts of LPD on infiltration 29**
6.1 Hypothesis . . . 29
6.2 Methodology . . . 29
6.3 Results . . . 30
6.4 Discussion . . . 32
6.5 Conclusions and outlook . . . 34

**7 Siphonic Flow Meter 35**
7.1 Design and Construction . . . 35
7.2 Discussion . . . 37
7.2.1 Methodological evaluation . . . 37
7.2.2 Practical evaluation . . . 38
7.3 Future Development . . . 39

**8 Synthesis and discussion 40**
8.1 From perceptual to conceptual . . . 40
8.1.1 Numerical modelling of slope effects . . . 41
8.2 Implications for LPD as an NbS for slope stability . . . 42
8.3 The OAL methodology . . . 43
8.4 Siphonic flow-meter . . . 43
8.5 Recommendations . . . 44
8.5.1 Current setup . . . 44
8.5.2 OAL design at FPH . . . 44
8.5.3 LPD research . . . 45

**References 46**

**A Lab protocols 51**
A.1 Calibration of Soil Moisture Sensors . . . 51
A.2 Calibration PVC flow-meter . . . 53
A.2.1 Preparing PVC tubing . . . 53
A.2.2 Calibrating flow-meter . . . 54
A.3 Mini disk infiltrometer . . . 56

**B Flow-meter 57**
B.1 Calibrating PVC flow-meter . . . 57
B.2 Development siphon flow-meter . . . 58

**C Additional data analyses 61**
C.1 LPD in applicability from bioengineering guide (Campbell et al., 2008) . . . 61
C.2 Flux target derivation, injection experiment . . . 62
C.2.1 Storage capacity . . . 62
C.2.2 Rainfall comparison . . . 62
C.2.3 Preferential flow velocities . . . 62
C.2.4 Target flux . . . 62
C.3 Calculation of flux from tank drawdown injection and irrigation experiment . . . 63
C.4 Check absolute values soil moisture . . . 65
C.5 cumulative fluxes sustained irrigation experiment . . . 66
C.6 Salt tracer breakthrough irrigation experiment . . . 67
C.6.1 breakthrough . . . 67
C.7 Observed response (time) after excavating the bottom of the slope . . . 67
C.8 Sensitivity analysis of estimated representative area soil-moisture sensors . . . 67
C.9 Log-normal distribution of hydraulic conductivity values experiment 3 . . . 69
C.10 Log PDF experiment 3 distribution . . . 70

C.11 Sample choice sensitivity in lumped infiltrometer box plots . . . 71
C.12 MODFLOW model setup . . . 71
C.12.1 Schematisation model setup . . . 72
C.12.2 Python code MODFLOW-NWT configuration . . . 73

**D Fieldwork photo logbook** **75**
D.1 OAL setup . . . 75
D.2 Point injection into bundles experiment . . . 76
D.3 Sustained distributed irrigation experiment . . . 78
D.4 Mini-Disk infiltrometer experiment . . . 81

**E Setup information** **82**
E.1 Setup improvements . . . 83

# List of Figures


1.1 LPD representation . . . 2
1.2 Open air LPD in Catterline, UK . . . 3
1.3 Scale model LPD research . . . 3

2.1 Schematisation of the Perceptual Models (PMs) . . . 5

3.1 Schematic overview of OAL LPD . . . 8
3.2 Bundle configuration in experimental setup . . . 9
3.3 Installed sensors LPD setup. . . . 9
3.4 Perforated PVC flow meter . . . 10

4.1 Hypothesised fluxes injection experiment . . . 11
4.2 Point injection experimental runs . . . 12
4.3 Diffuse influx hose . . . 12
4.4 Influx positioned in live bundle . . . 12
4.5 Drain outflow point injection experiment . . . 13
4.6 Soil moisture response injection experiment . . . 14
4.7 Observered leakage injection experiment . . . 16
4.8 Drain configuration observations . . . 16
4.9 Likely flowpaths injection experiment . . . 17
4.10 Potential pressure build-up injection experiment . . . 18
4.11 Calibration sensitivity drain flow injection experiment . . . 19

5.1 Schematisation irrigation experiment setup . . . 20
5.2 Daytime and nighttime irrigation regimes . . . 21
5.3 Flux in irrigation experiment . . . 21
5.4 Experimental design irrigation experiment . . . 22
5.5 Soil-moisture response irrigation experiment . . . 23
5.6 Outflow through drain 2, irrigation experiment . . . 24
5.7 Representative area soil moisture sensors . . . 24
5.8 Cumulative residual water balance, with linear fit. . . . 25
5.9 Irrigation setup limitations . . . 26
5.10 Polynomial vs local differentiation flow estimates . . . 26
5.11 Relative difference between flow estimates . . . 27
5.12 Calibration sensitivity drain flow irrigation experiment . . . 27

6.1 Measurement grid infiltrometer experiment . . . 30
6.2 Hydraulic conductivity estimates on LPD and reference slope . . . 31
6.3 Conductivity estimates by infiltrometer position . . . 31
6.4 Antecedent soil moisture on LPD and reference slope . . . 33

7.1 Design schematic siphonic flow meter . . . 36
7.2 Processing siphonic flow meter pressure data . . . 37

8.1 LPD representation in OAL and MODFLOW-NWT model . . . 41
8.2 Diversion ratio sensitivity to slope, base, and interface conductivity . . . 42

A.1 METER 5TE Sand layer calibration sheet . . . 52
A.2 METER 5TM Sand layer calibration sheet . . . 52
A.3 Design dimensions PVC flow-meter . . . 53
A.4 PVC flow-meter in a control bucket . . . 54
A.5 Calibration PVC flow meter polynomial fits . . . 55
A.6 Calibration PVC flow meter for high flows . . . 55
A.7 Calibration PVC flow meter for low-flows . . . 55

B.1 Calibration PVC flow meter polynomial fits . . . 57
B.2 Preliminary design Pythagoras cup flow meter . . . 58
B.3 Design iterations siphonic flow meter . . . 59
B.4 Inside area siphonic flow meter . . . 60

C.1 Bioengineering measures versatility overview . . . 61
C.2 Water height and pumping flux, injection runs 1 and 2 . . . 63
C.3 Water height and pumping flux, injection runs 3 and 4 . . . 63
C.4 Injection flux, runs 1.1 and 1.2 . . . 63
C.5 Injection flux, runs 1.3 and 1.4 . . . 64
C.6 Polynomial fits to tank drawdown irrigation experiment . . . 64
C.7 Soil moisture comparison with Berlitz long-term measurements . . . 65
C.8 Injection run 1 soil moisture against sandy soil values . . . 65
C.9 Injection run 3 soil moisture against sandy soil values . . . 66
C.10 Cumulative volumes water balance irrigation experiment . . . 66
C.11 Salt tracer injection runs 3 and 4 . . . 67
C.12 Stills from time-lapse response to pumping in dead bundle. . . . 68
C.13 Cumulative storage irrigation experiment . . . 69
C.14 Delta storage irrigation experiment . . . 69
C.15 Log-normal fits to bare slope data . . . 69
C.16 Log-normal fits to LPD slope data . . . 70
C.17 Infiltrometer log-conductivity PDF . . . 70
C.18 Effect of point selection on LPD and bare slope conductivity . . . 71
C.19 MODFLOW-NWT model schematisation . . . 72
C.20 Tornado diagram MODFLOW-NWT . . . 72
C.21 Parameter definition MODFLOW-NWT setup in Python. . . . 73
C.22 Parameter sweep MODFLOW-NWT model setup in Python. . . . 74

D.1 Initial surface vegetation, 24/09/25 . . . 75
D.2 Initial surface vegetation control slope, 24/09/25 . . . 75
D.3 Sprouting of slope one 07/10/25 . . . 75
D.4 Covered slope one 07/10/25 . . . 75
D.5 Dug hole at top end of bundles 13/10/25 . . . 76
D.6 Tank filling, 10/12/25 . . . 76
D.7 Cover ponding, 21/10/25 . . . 76
D.8 Log point injection . . . 76
D.9 No initial flow alongside drain 2, 11/11/25 . . . 77
D.10 Frost, 21/11/25 . . . 77
D.11 Regrowth willow, 24/11/25 . . . 77
D.12 Flow alongside drain, 21/11/25 . . . 77
D.13 Observed leak, 16-12-25 . . . 77
D.14 Clogged hose, 03/12/25 . . . 78
D.15 Drain in risk of submergence, 12/12/25 . . . 78
D.16 Leakage hole, 02/12/25 . . . 78
D.17 Excavated bundle, 10/12/25 . . . 78

D.18 Log sustained irrigation . . . 78
D.19 Tapered top of nightly irrigation tank, 14/12/25 . . . 79
D.20 Nightly irrigation tank filled with bricks, 16/12/25 . . . 79
D.21 Shape nightly irrigation tank, 15/12/25 . . . 79
D.22 Drip irrigation, 14/12/25 . . . 79
D.23 Nightly gravitational irrigation, 14/12/25 . . . 79
D.24 Daily irrigation, 19/12/25 . . . 79
D.25 Observed drip irrigation, 15/12/25 . . . 80
D.26 No flow alongside drainage hole, 15/12/25 . . . 80
D.27 Mushroom, 19/12/25 . . . 80
D.28 Mushrooms, 12/12/25 . . . 80
D.29 Log infiltrometer experiment . . . 81
D.30 Infiltrometer test, 27/11/25 . . . 81
D.31 Stabilised infiltrometers, 05/02/26 . . . 81

E.1 Setup media properties . . . 82
E.2 Smart sensor setup . . . 82
E.3 Observed perforation setup . . . 83
E.4 Modified drain after injection experiment . . . 83

# List of Tables


4.1 Pumped volume experiment run 1.1-1.4. . . . . 13
4.2 Water balance injection experiment . . . . . 15
4.3 Uncertainty drainage injection experiment . . . . . 18

5.1 Pumped influx volume (Day, night and total) irrigation experiment . . . . . 22
5.2 Water balance irrigation experiment . . . . . 24
5.3 Uncertainty drainage irrigation experiment . . . . . 27

C.1 Daily and cumulative change in soil water storage . . . . . 67

# 1

# Introduction

Landslides worldwide cause socio-economic disasters, affecting lives and property (Sidle & Bogaard, 2016). As temperatures, precipitation frequency and duration rise due to climate change, precipitation-triggered, rapid landslides are projected to occur more often (Kumar et al., 2020), highlighting the need for mitigation measures. This study focuses on shallow landslides, as they can be triggered by individual storms and prolonged rain events, generally move more quickly than deep-seated landslides (Sidle & Bogaard, 2016), and offer more feasible mitigation options (Capobianco et al., 2025). Most landslides are directly linked to extreme precipitation events (Bogaard & Greco, 2016), with common triggers including positive pore-water pressure, loss of suction through progressive wetting, and increased overburden weight from infiltrating rainwater (Sidle & Bogaard, 2016). Central to these triggers is subsurface flow, which operates through a complex spectrum of pathways whose interactions remain poorly understood (Blöschl et al., 2019; Jarvis et al., 2016). More broadly, the link between soil physical processes and catchment-scale hydrological behaviour remains elusive (Sidle & Saito, 2024), giving rise to Landslide Hydrology as a dedicated research field (Bogaard & Greco, 2016). Beyond the initial failure, landslide-affected areas remain particularly vulnerable to concentrated flow erosion in the form of rill and gully erosion, which is responsible for the majority of soil loss on hillslopes (Stokes et al., 2014). Ongoing soil instability prevents natural plant establishment (Pacas & Polster, 1999), leaving slopes exposed to further erosion and recurrent failure.

## 1.1. Bioengineering as a Nature-based Solution

Nature-based Solutions (NbS) for mitigating landslides are rising in popularity (Capobianco et al., 2025), as traditional grey civil engineering landslide mitigation measures tend to be too rigid to adapt to climate change (Berlitz et al., 2024; Kumar et al., 2020), and can be disruptive. NbS can adapt to environmental changes, often require low maintenance (Campbell et al., 2008), and have the capacity to grow rather than deteriorate over time (Goldsmith et al., 2014; Pacas & Polster, 1999; Stokes et al., 2014). They also tend to enhance local biodiversity, which can improve soil infiltration and percolation, reduce peak stormwater runoff, and contribute to broader ecosystem services, including human well-being (Berlitz et al., 2024). NbS that use vegetation to repair damage caused by erosion and slope failures are categorised as bioengineering (Norris et al., 2008), and are particularly suited to the shallow landslide contexts described above (Capobianco et al., 2025). Despite the growing attention these approaches receive in research, their implementation remains limited. Their adaptive, evolving nature creates uncertainty about long-term properties, which, alongside limited monitoring and a preference for fast predictable solutions, limits wider adoption (Kumar et al., 2020).

## 1.2. Live Pole Drains

Live Pole Drains (LPD) consist of bundles of live cuttings, typically willows, placed into the soil in shallow trenches and lightly covered (Goldsmith et al., 2014; Pacas & Polster, 1999), as visually depicted in Figure 1.1a. A bundle of live cuttings is placed on top of two dead bundles, as shown in Figure 1.1b, to

support the live bundle and supply nutrients once they decay. These fascines immediately facilitate faster slope drainage by establishing preferential flow paths. Over time, these cuttings will grow above and below the surface, stabilising the soil and stimulating percolation through preferential flow along roots. Transpiration from established cuttings is the strongest hydrological mechanism by which vegetation influences slope stability (Gonzalez-Ollauri & Mickovski, 2017), increasing matric suction ahead of storm events. However, this effect is largely absent under the critical hydrological conditions that trigger slope instability, and in temperate regions occurs predominantly during dry periods of low landslide risk, making it most relevant in tropical and semi-tropical climates (Ghestem et al., 2011). Additional benefits of established LPD include mechanical reinforcement through root networks, rainfall interception on leaves (González-Ollauri & Mickovski, 2014), and the facilitation of broader slope revegetation (Campbell et al., 2008; Pacas & Polster, 1999). In contrast to traditional grey engineering solutions, LPD require no heavy machinery and are well-suited to steep slopes and hard-to-reach locations (Bowyer et al., 2024; Polster & Bio, 1997). They are particularly applicable to natural terrain landslide scars, where re-establishing vegetation cover is critical to preventing recurrent failure (Campbell et al., 2008; Stokes et al., 2014). Although LPD are predominantly documented as a measure against superficial soil erosion, it remains a working hypothesis that their mechanisms extend to the prevention of shallow landslides (Berlitz et al., 2024; Capobianco et al., 2022; Mafian et al., 2009), with effectiveness expected to diminish as failure depth increases. Research on LPD is being conducted in collaboration with Glasgow Caledonian University as part of OPERANDUM, including field-based experiments at Catterline and physical-scale model testing. The scale model experiments specifically have shown promising results for moisture drainage and buffering capacity by LPD (Berlitz et al., 2024).

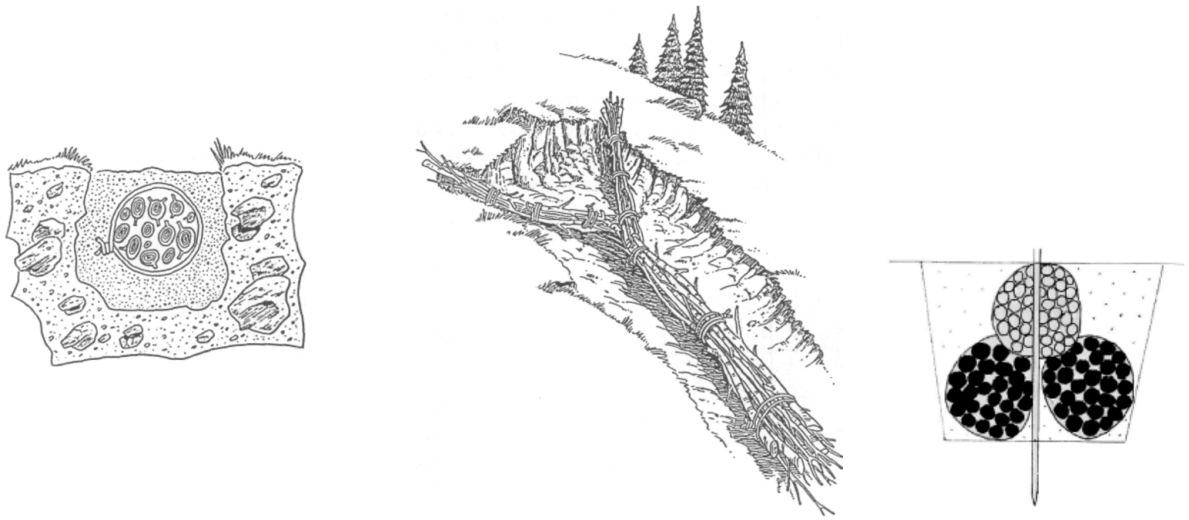



**Figure 1.1:** a) Representation of LPD (Polster & Bio, 1997), b) Live bundles on top of two dead bundles (Norris et al., 2008).

## 1.3. Open-Air Laboratories

Open-air laboratories (OAL) such as those established within the OPERANDUM project and at the Hydrological OAL Petzenkirchen enable a more realistic research environment and facilitate longer-term research compared to conventional laboratory experiments (Blöschl et al., 2016; Bowyer et al., 2024; Gonzalez-Ollauri et al., 2023). The experimental setups combine realistic natural forcing with long-term monitoring, enabling proof-of-concept testing of NbS for mitigating hydrological hazards (Gallotti et al., 2021; Kumar et al., 2020). In addition to providing proof of concept, OAL foster collaboration across research, policy, and practice (Blöschl et al., 2016; Bowyer et al., 2024; Kumar et al., 2020). As such, they represent an important step towards operationalising NbS. While valuable as real-world proof-of-concept applications of NbS, unknown boundary conditions, such as subsurface heterogeneity and uncontrolled seepage, can limit the physical and hydrological interpretability.

## 1.4. Research objective

This study aims to develop an evidence-backed conceptual model of LPD hydrological behaviour and its implications for slope stability. Despite the promising results from earlier scale model experiments (Figure 1.3), the underlying hydrological processes remain poorly understood (Berlitz et al., 2024), and the long-term behaviour and extent of positive externalities are yet unquantified (Seddon et al., 2020). The study primarily investigates LPD from a shallow landslide hydrology perspective, though findings also speak to their effectiveness against superficial erosion. To advance process understanding, this study adopts a more controlled OAL approach. Whereas existing OAL, such as Catterline (Figure 1.2) and HOAL Petzenkirchen, function more as experimental catchments, the setup used here bridges the gap between lab-scale experiments and such catchments, offering a compromise between contextual realism and experimental control. While complete process isolation is not feasible, this setup enables a clearer separation of hydrological fluxes than the Catterline field site, and focuses on three hydrological processes central to slope stability: infiltration, percolation, and subsurface runoff. This understanding is developed and tested experimentally, structured around the following main objective:

**To develop an evidence-based conceptual model of the hydrological behaviour of Live Pole Drains, through experimental investigation**

This is addressed through five sub-objectives:

1. To characterise preferential and lateral subsurface flow through and around LPD, transitioning from perceptual to conceptual understanding of LPD drainage behaviour.
2. To quantify the impact of LPD on infiltration under varying antecedent moisture conditions, transitioning from perceptual to conceptual understanding of flux dynamics around the pole drains.
3. To discuss the implications of LPD hydrological behaviour for their application as a NbS for slope stability.
4. To evaluate the OAL approach as a methodology for hydrological NbS research.
5. To develop and validate instrumentation enabling accurate field-scale quantification of LPD hydrological fluxes.



**Figure 1.2:** Open air LPD in Catterline, UK. (Modified from Cahill (2024)).

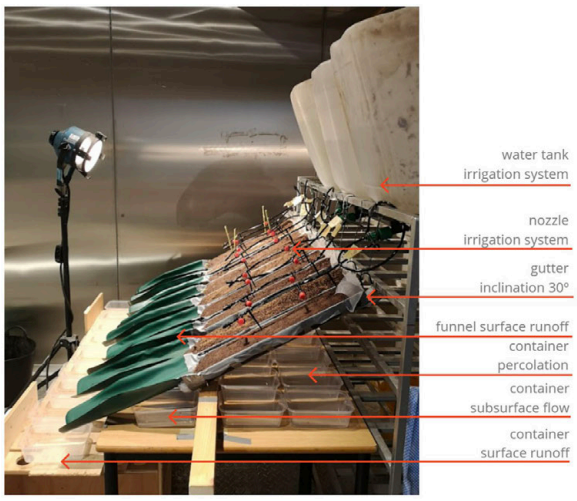



**Figure 1.3:** Scale model research LPD at Glasgow Caledonian University (Berlitz et al., 2024).

## 1.5. Thesis outline

This thesis opens with the presentation of four LPD perceptual models that serve as a conceptual framework for the subsequent hypothesis-testing experiments. Following Pfister and Kirchner (2017) and Blöschl et al. (2016), a hypothesis-testing structure is adopted to systematically evaluate the perceptual models against experimental observations. Mindful of the risks of confirmation bias and retrofitted hypothesis testing, hypotheses were formulated prior to the experimental design and data collection. The first two experiments adopt a process-based, advective framing, in which explicit water fluxes are imposed to quantify water routing through the system; process attribution is central, and individual flow pathways are explicitly resolved. The third experiment takes a contrasting diffusive approach, using infiltrometer measurements to estimate unsaturated hydraulic conductivity as a lumped variable, characterising the overall infiltration response of the system rather than resolving individual flow pathways.

Each experimental chapter presents the associated methodology, results, discussion, and recommendations. The thesis concludes by synthesising findings across all three experiments and the instrument-design work. Their collective relevance is then situated within open-air laboratory hydrological research and the application of 3D printing in hydrological instrument design.

# 2

# Perceptual models

Conceptualising the effects of lateral preferential flow poses a major challenge in hillslope hydrology, and field descriptions of preferential flow are often complex and qualitative (Weiler & McDonnell, 2007). Translating such complexity into predictive models is inherently difficult (Konikow & Bredehoeft, 1992), and K. J. Beven and Chappell (2021) argue that this difficulty stems partly from insufficient perceptual understanding of the underlying processes. They stress the importance of developing rigorous perceptual models, both to ground predictions in observable hydrological processes and to increase confidence that models produce 'the right results for the right reasons', going as far as to suggest that 10 of the 23 unsolved problems in hydrology identified by Blöschl et al. (2019) may be a consequence of a lacking perceptual understanding.

To reduce this complexity and make explicit different perceptions of LPD behaviour, this chapter introduces a set of perceptual models (PMs), schematically presented in Figure 2.1. K. Beven (2012) defines PMs as personal qualitative perceptions of responses, unconstrained by mathematical theory. In this study, PMs serve as a framework for designing targeted experiments, for interpreting experimentally observed flow behaviour and identifying the dominant hydrological mechanisms. As PMs are simplifications of complex subsurface flow behaviour, the experimental work in this thesis examines likely combinations of PMs and assesses their relevance to understanding the hydrological behaviour of LPD.

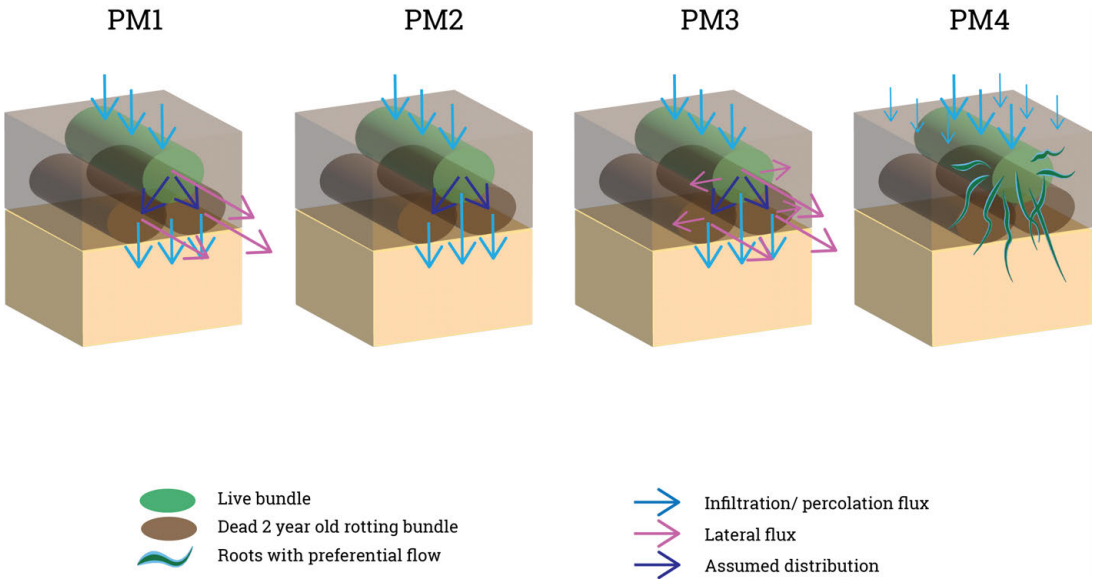



**Figure 2.1:** Schematisation of the Perceptual Models (PMs)

## 2.1. Perceptual Model 1 (PM1): Increased subsurface flow and (distributed) percolation

In soil bioengineering guides by Campbell et al. (2008) and Pacas and Polster (1999), as well as in Goldsmith et al. (2014)'s description of bioengineering case studies, LPD are described as lateral conduits that collect and channel surface runoff, thereby enhancing slope drainage. This interpretation is supported by small-scale experimental studies by Berlitz et al. (2024) and Benschop (2022), which demonstrate that slopes containing LPD exhibit increased subsurface runoff, increased distributed percolation compared to bare slopes, and reduced overall water retention within the soil profile. These experiments further indicate a tendency for percolating water to concentrate near the downslope end of the LPD. Complementary field investigations by Cahill (2024) indicate quick lateral drainage through LPD under imposed lateral flow conditions, confirming their capacity to transmit water efficiently downslope.

Based on these experimental findings, PM1 conceptualises LPD as preferential flow systems that operate both laterally and vertically. Water is conveyed downslope through enhanced subsurface flow along the LPD bundle, while vertical percolation is facilitated by preferential flow pathways associated with roots. The effectiveness of these pathways is expected to increase under higher antecedent soil moisture conditions.

## 2.2. Perceptual Model 2 (PM2): Vertical preferential drainage

PM2 conceptualises LPD as vertical, high-conductivity preferential pathways that transmit infiltrating water predominantly downward, with limited interaction with the surrounding soil matrix. Flow within the bundle is gravity-dominated, and lateral diversion is minimal because the high vertical hydraulic conductivity enables rapid drainage, thereby preventing significant pressure build-up within the LPD. As soil moisture increases beneath the bundle, the vertical drainage flux is expected to increase in accordance with the well-established relationship between hydraulic conductivity and saturation described by Van Genuchten (1980). Lateral redistribution of water from the bundle into the adjacent soil remains limited in this perceptual model due to a strong contrast between the bundle's vertical hydraulic conductivity and the comparatively lower lateral conductivity of the surrounding soil matrix.

## 2.3. Perceptual Model 3 (PM3): Conditional lateral redistribution under sustained wetness

PM3 represents a transitional flow regime between PM2 and PM1, in which LPD primarily function as vertically oriented, high-conductivity pathways under most conditions, but progressively facilitate lateral redistribution once threshold conditions are exceeded. Similar to PM2, vertical flow through the bundle remains the dominant transport mechanism during low to moderate wetting, with gravity-driven drainage limiting pressure build-up and sorptive interaction with the surrounding soil matrix.

Under prolonged or high-intensity wetting, however, increasing soil moisture and hydraulic connectivity within the surrounding matrix reduce the effectiveness of rapid vertical drainage alone. As the soil approaches saturation, lateral hydraulic gradients develop, activating lateral exchange between the bundle and adjacent soil. This behaviour marks the transition toward PM1-type dynamics, in which lateral preferential flow contributes more substantially to downslope redistribution.

In PM3, lateral flow is therefore not continuous but threshold-dependent, emerging only after the soil moisture and conductivity thresholds of the surrounding soil matrix are exceeded. Once activated, lateral redistribution is expected to be spatially constrained and strongly dependent on both the duration and intensity of wet conditions. This conceptualisation is consistent with syntheses of hillslope hydrology that identify lateral preferential flow as a principal component of stormflow response and emphasise its threshold-controlled nature (Uchida et al., 2005; Weiler & McDonnell, 2007).

## 2.4. Perceptual Model 4 (PM4): Indirect hydrological influence via soil structural modification

PM4 conceptualises live pole drains as indirect and diffuse modifiers of soil hydraulic behaviour rather than as discrete preferential flow conduits. Instead of isolating individual flow processes, this perceptual model adopts a lumped perspective in which the hydrological influence of LPD arises from cumulative biological and structural changes in the soil over time. Through root growth and associated biological activity, LPD may progressively modify near-surface soil structure, macroporosity, and infiltration heterogeneity (Gonzalez-Ollauri & Mickovski, 2017).

Under PM4, the hydrological effects of LPD are expressed primarily as changes in infiltration behaviour, hydraulic diffusivity, and spatial variability at the hillslope scale, rather than as identifiable lateral subsurface flow pathways. As such, PM4 does not predict clear or systematic lateral redistribution in integrated flow experiments. Instead, it motivates the use of diagnostic and integrative measurements that capture bulk or effective near-surface hydraulic properties, rather than event-scale flow routing.

The relevance of PM4 is expected to increase with time as LPD mature and biological effects accumulate. In addition to the development of root systems within the live bundle itself, LPD may facilitate the establishment of surrounding vegetation by improving local growth conditions (Campbell et al., 2008; Goldsmith et al., 2014; Pacas & Polster, 1999). This secondary vegetation growth can further enhance preferential infiltration and diffuse soil modification, reinforcing the lumped, emergent hydrological influence represented by PM4 (Stokes et al., 2009).

# 3

# Open-air laboratory setup: configuration and instrumentation

Cahill (2024), in collaboration with the Applied Ecology research group at Glasgow Caledonian University, have designed and constructed an OAL experimental setup at Flood Proof Holland (FPH) in Delft, the Netherlands, as schematically presented in Figure 3.1. The setup consists of three trenches resembling uniform hillslopes: the first enables short-term research on the LPD's behaviour and allows interventions; the second is designated for longer-term research on an undisturbed LPD; and the third serves as a bare reference slope. Comparison of the LPD to a bare slope, presented as trench 3 in Figure 3.1, enables investigation of the modifications in slope hydrological processes caused by the LPD. The setup has a fixed slope; therefore, the influence of varying slopes on LPD behaviour is not investigated. The setup was completed by February 2024, so the LPD have been growing for approximately 18 months at the start of this research. Long-term monitoring, using pre-installed smart sensors, is being conducted by PhD candidate Fernanda Berlitz.

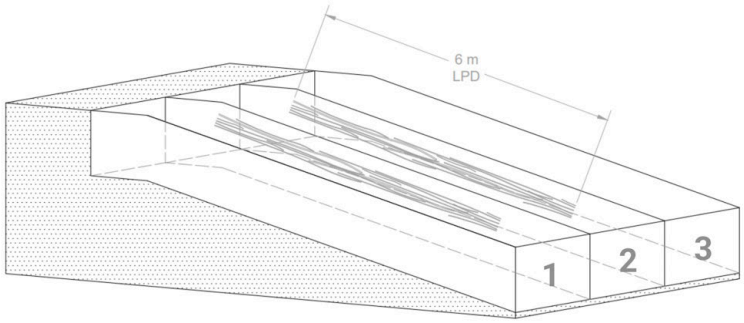



**Figure 3.1:** Schematic overview of OAL LPD. (Modified from Cahill (2024)).

The tank gradient is estimated at $10^{\circ}$ on 29/09/2025. Figure 3.2a illustrates the distribution of the layers, with sand forming the lower part and growing soil the upper part. The LPD consists of bundles of Osier and White Willow of 30 cm in diameter with a length of 6 m (Cahill, 2024), with a live bundle on top of two dead ones, following the configuration shown in Figure 3.2b. Soil properties at installation, as determined by Cahill (2024), are presented in Figure E.1. Notably, while LPD are typically installed in settings with low-permeable soils, the present experimental setup places the LPD on a highly permeable sand layer.



(a) (b) (c)

**Figure 3.2:** (a) Sketch cross-section soil distribution experimental setup (Cahill, 2024), (b) zoomed-in distribution of a live bundle over two dead bundles (Berlitz et al., 2024), and (c) dug hole at the top end of bundles (13/10/25).

To enable low-moisture content measurements in Dutch fall/winter weather conditions, the setup was covered. Requiring the willow sprouts to be pruned, presented in Appendix D.1. The top of the bundle was freed by digging a hole at its top end. The layout of the bundles, at the top of the slope, could then be observed and is presented in Figure 3.2c.

## 3.1. Sensor placement

The setup is equipped with two working, pre-installed percolation drains and six METER ECH2O soil-moisture sensors. The sensors were calibrated for the sand layer beneath the bundle, following the protocol described in Appendix A. All sensors were programmed to log at a 1-minute interval to accurately capture the short-term dynamics of the drainage response. On November 6th, the sensors were installed at a depth of 35 cm at logarithmically increasing intervals along the slope, achieving a greater measurement density near the top of the slope (the point of influx), where changes in soil moisture are most likely. The sensors were placed six days before the first experimental run to allow the soil to redistribute, with a tight seal achieved by repeatedly wetting the soil on top. Due to experimental constraints, sensors could only be installed beneath one of the dead bundles without causing damage to the bundle structure, as depicted in Figure 3.3.

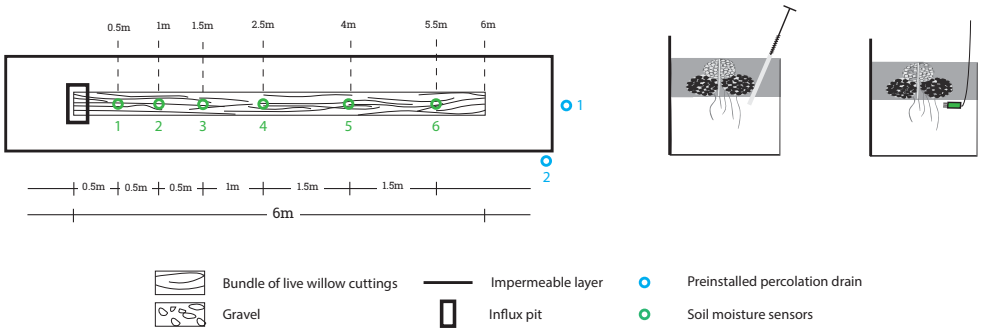



**Figure 3.3:** Installed sensors LPD setup.

## 3.2. Percolation and LPD drains

Flow through the percolation and through the bundle drain was measured with KELLER DCX-22AA pressure sensors in PVC tubes. A smaller tube diameter results in a higher resolution. As large volumes were expected to drain from the setup, these tubes need to self-empty; otherwise, they would overflow. This is achieved through a perforated PVC pipe, as shown in Figure 3.4, which is calibrated for different flow velocities according to the protocol outlined in Appendix A. The sensors were placed in buckets to observe the initial flow through the drain. The height resolution of the pressure sensors is 0.5 $mm$, with an area of 1.257 $mm^2$. The pressure sensors were equally programmed to log at a 1-minute interval, resulting in a volume resolution of the PVC flow-meter of 628 $mm^3$ = 0.628 $ml$ per minute, assuming perfect calibration. The cumulative flow volume through the PVC drains was then determined by converting the time to hours and integrating the flow rate using the trapezoidal rule, as described by Lanzafame et al. (2024).

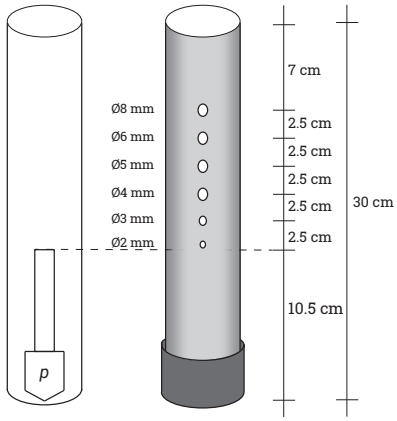



**Figure 3.4:** Perforated PVC flow meter

## 3.3. Weather conditions

The experiments were conducted between December and February under Dutch winter conditions in an outdoor laboratory setting. Low air temperatures and weak solar radiation during this period strongly limited evaporative fluxes. The pruning and covering of the LPD prevented photosynthesis and effectively eliminated transpiration. Slight regrowth was observed only while the black cover was in place, likely due to locally elevated temperatures beneath it; once the cover was removed, vegetation rapidly died back, and no further regrowth occurred. Occasional night frost occurred during the experimental period, but no freezing occurred during the experiments. Consequently, evapotranspiration fluxes were assumed to be negligible, and the experimental conditions represent hydrological behaviour under cold-season conditions.

# 4

# Point injection into bundles: initial drainage pathway assessment

## 4.1. Hypothesis

It is hypothesised that water pumped into the bundle is predominantly conveyed downslope through the bundle, with the fraction transmitted depending on antecedent soil moisture conditions, in line with PM1 behaviour. Under conditions of high antecedent soil moisture, the macropore network is fully hydraulically active, resulting in the entire inflow being discharged into drain 1, shown in Figure 3.3. Under low antecedent soil moisture conditions, only a fraction of the flux is transmitted through the bundle, while the remaining flux percolates into the surrounding soil, where it is partly retained in the soil matrix and partly discharged via drain 2. The location of water input, into a single dead bundle versus into the top live bundle, does not influence lateral redistribution. The fluxes are illustrated in Figure 4.1.

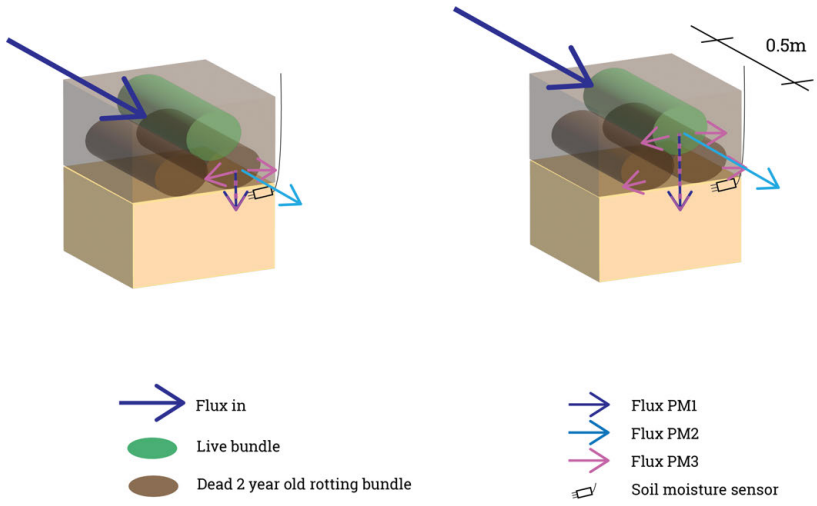



**Figure 4.1:** Hypothesised fluxes injection experiment

## 4.2. Methodology

The injection experiment consisted of four runs, structured as two input locations × two antecedent moisture conditions, as schematised in Figure 4.2. A flux was applied to both the dead bundle, directly above the soil moisture sensors, and the live bundle. As sensors could not be positioned centrally beneath the live bundle due to physical constraints, the dead bundle runs serve as an interpretive baseline, enabling comparison with the live bundle runs. Inter-bundle lateral redistribution was not treated as a separate hydrological mechanism; instead, input location was treated as an experimental boundary condition that may influence how results are expressed but does not alter the underlying hydrological processes being tested.

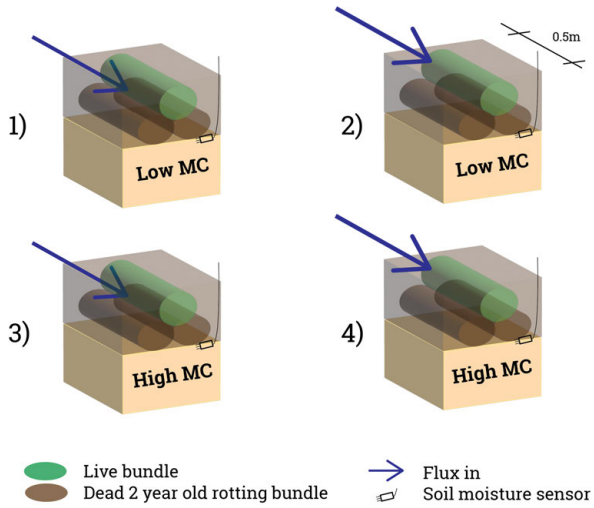



**Figure 4.2:** Four point injection experimental runs, two with varying antecedent moisture content (MC))

Water from a nearby ditch was pumped into the test bundle using a Watson–Marlow 704S peristaltic pump, drawing from 1 $m^3$ storage tanks filled by a Gardena Clear Water Pump 9000 submersible pump. Water was pumped in through a perforated tube, shown in Figure 4.3, to diffuse the flux and prevent localised pressure build-up. The hose was positioned 44 $cm$ into the dead bundle and 37.5 $cm$ into the live bundle, as presented in Figure 4.4, for both antecedent moisture conditions tested.

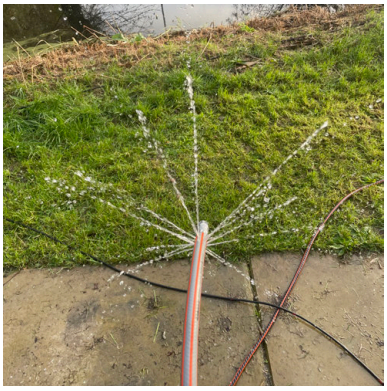


**Figure 4.3:** Diffuse influx hose



**Figure 4.4:** Influx positioned in live bundle

The experiment consisted of four runs, two under low and two under high antecedent moisture conditions, as schematised in Figure 4.2. Low antecedent moisture conditions were established by covering the setup with plastic 35 days before the first experiment run, shown in Figure D.4. Higher antecedent moisture conditions were established by natural rainfall after the cover was removed.

A target inflow rate of approximately 250 $L/h$ was selected based on a combination of storage capacity estimates, time constraints, and plausible preferential flow velocities. The derivation of this target is detailed in Appendix C.2, with the key conclusion being that a 4–5 hour application at this rate delivers approximately 1000–1250 $L$, sufficient to exceed estimated storage capacity and induce measurable drainage. Prior to the experiment, the pump operating at 65 RPM was verified to deliver 266.8 $L/h$, and was maintained at this rate for 5 hours, yielding a total influx of 1334 $L$ per run. To account for any variation in flux as the supply tank emptied, a pressure sensor was placed in the water supply tank. The tank drawdown was fitted with first-order polynomials and converted to flow, assuming a constant tank water surface area, via a volume balance:

$$Q_{\text{out}} = A \frac{\mathrm{d}h}{\mathrm{d}t} \tag{4.1}$$

where $Q_{\text{out}}$ is the flux out of the tank, $A$ the tank cross-sectional area, and $\frac{\mathrm{d}h}{\mathrm{d}t}$ the rate of change of water level over time. The goodness of fit of $R^2 > 0.995$ and the derived flux over time for each run are shown in Appendix C.3. The total volumes pumped per run are listed in Table 4.1. Salt was added as a tracer during runs 1.3 and 1.4 to analyse water retention time in the setup.

| Run | Volume [L] |
|---|---|
| Run 1.1 (low MC, dead bundle) | 1150 |
| Run 1.2 (low MC, live bundle) | 1070 |
| Run 1.3 (high MC, dead bundle) | 950 |
| Run 1.4 (high MC, live bundle) | 990 |

**Table 4.1:** Pumped volume experiment run 1.1-1.4.

Results are interpreted using a simple water balance:

$$P = Q + \Delta S + L \tag{4.2}$$

where $P$ is the applied inflow, $Q$ the measured outflow at drain 2, $\Delta S$ the change in soil water storage, and $L$ is the residual term encompassing all unmonitored losses.

## 4.3. Results

### 4.3.1. Flow through drain(s)

Drain 2 was the only drain to receive any water. Indicating that no water was conveyed through the entire bundle, and immediately disproving the hypothesis of PM1. Figure B.1 shows the outflow from drain 2 across all four experiment runs. Water height in the drain was converted to flux through the drain by lab calibration following the protocol in Appendix A.2.2. Flow rates through drain 2 were consistently higher during run 1.1 than in runs 1.2–1.4. A step-wise increase in flow toward the end of the run is also visible, most prominently in run 1.1, and to a lesser extent in runs 1.2–1.4. Figure 4.5 shows breakthrough of ditch water through the drain consistently occurred after about 50 minutes of switching from tracer to ditch water influx. The observed tracer breakthrough time roughly matches that through drain 2, just under 1 hour, as shown in Figure C.11. As the EC measurement interval was coarse and irregular, this measurement is not precise to the minute.

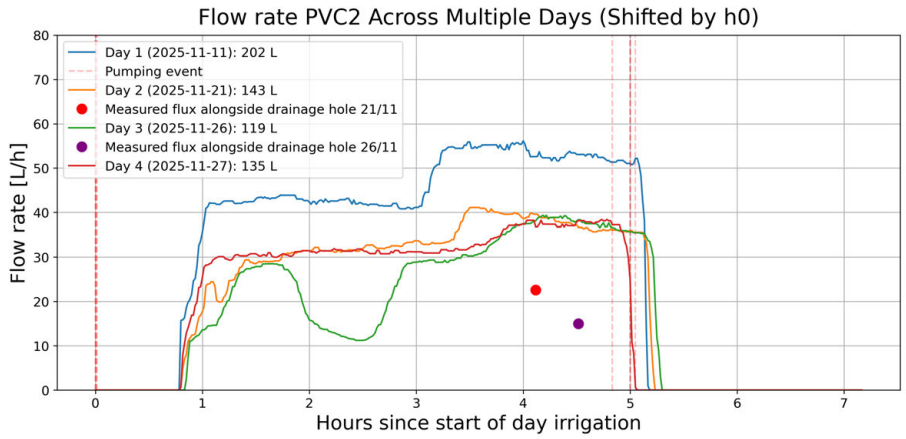



**Figure 4.5:** Flow through drain 2 for run 1-4 combined in one plot, plotted for hours passed since the start of pumping.

The total volume through the drain was determined to be approximately 202$L$, 143$L$, 119$L$, and 135$L$ for runs 1–4, respectively. Run 1.1. shows a higher outflow than all other runs, 202 $L$ compared to the similar 119-143 $L$ during run 1.2-1.4. This decrease is partly attributed to leakage observed from run 1.2 onwards at the point where the drain exits the setup, where water was found to flow alongside rather than through the drain pipe, as shown in Figure D.12. At two instances, the leakage outflow was measured manually, presented as scatter points in Figure 4.5. These measurements indicated that the leakage flow rate exceeded 50% of the flow through the drain during run 1.3, and approximately 40% during run 1.4, suggesting that the actual total outflow was considerably higher than the flux measured through the drain alone.

### 4.3.2. Soil moisture data

Figure 4.6 shows the volumetric water content ($\theta$) [$m^3/m^3$] measured by soil moisture sensor 1 for run 1.1 (dry antecedent conditions) and run 1.3 (wet antecedent conditions). In both runs, $\theta$ increased sharply at the start of pumping, followed by a gradual decline. Soil moisture sensor 1 was the only sensor that responded to inflow, and this response occurred exclusively during inflow to the dead bundle; no response was observed during inflow to the live bundle. All remaining sensors showed no measurable change throughout the experiment, indicating that the wetting front did not propagate laterally beyond the immediate vicinity of the injection point. Run 1.2 and 1.4, water injection into the live bundle, did not result in any SM response, in contrast to the pumping into the dead bundle.

During run 1.1, θ rose from an initial value of approximately 0.035 $m^3/m^3$ to 0.15 $m^3/m^3$ within roughly 40 minutes. Under the wetter antecedent conditions of run 1.3, the sensor registered an increase from 0.07 $m^3/m^3$ to approximately 0.14 $m^3/m^3$ in about 20 minutes. The shorter response time and comparable peak value in run 1.3 are consistent with a higher unsaturated hydraulic conductivity at elevated initial moisture content, allowing the wetting front to reach the sensor more rapidly.

Following the peak, both runs exhibit an approximately exponential decline, with θ decreasing relatively quickly in the first one to two hours before approaching equilibrium only after five or more hours. After run 1.1, the sensor stabilised at approximately 0.07 $m^3/m^3$ rather than returning to the initial dry value of 0.035 $m^3/m^3$, indicating net storage in the sand layer as it wetted toward field capacity. Since evaporation was negligible within the sand layer, this equilibrium value can be interpreted as an in situ estimate of the sand's field capacity, though it could not be quantified precisely from a single sensor location. This also explains why $\Delta\theta$ was effectively zero during subsequent runs: the sand was already at or near field capacity prior to each new inflow event.

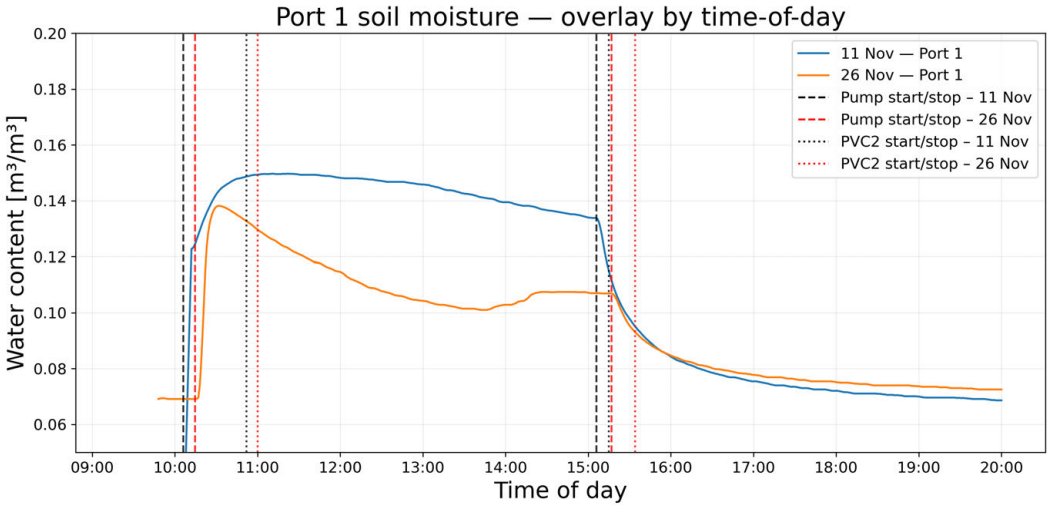



**Figure 4.6:** Soil Moisture data sensor 1 experiment run 1.1 on 11 Nov and 1.3 on 26 Nov on shared x-axis hour of day.

The rapid initial increase indicates that the inflow quickly saturated the soil surrounding the sensor beneath the dead bundle. The subsequent redistribution downward, combined with the lack of response at all other sensor locations along the length of the LPD bundle, suggests that water predominantly infiltrated into the underlying sand layer rather than advancing along the bundle. These observations are consistent with a brief initial phase of behaviour resembling PM1, local saturation and limited lateral flow near the injection point, followed by a transition to PM2, in which vertical percolation into the sand dominates. The response of sensor 1 was significantly lower for run 1.3 with increased antecedent soil moisture than for low antecedent soil moisture, especially after the peak had been reached.

### 4.3.3. Water balance

Table 4.2 summarises the water balance for each experimental run. The applied inflow volume ranged from 950 to 1150 $L$ per run, totalling approximately 4160 $L$ across all four runs. Outflow measured at drain 2 accounted for only 134–213 $L$ per run, corresponding to recovery rates of 14-19%.

**Table 4.2:** Water balance per injection experiment run. $\Delta S$ is estimated from soil moisture sensor 1 only; the residual term $L$ includes all unmonitored losses.

| | $P$ [L] | $Q$ [L] | $\Delta S$ [L] | $L$ [L] | $Q/P$ [%] |
|---|---|---|---|---|---|
| Run 1 | 1150 | 202 | $> 0$ | $\sim$948 | 18 |
| Run 2 | 1070 | 143 | $\approx 0$ | $\sim$927 | 13 |
| Run 3 | 950 | 119 | $\approx 0$ | $\sim$831 | 13 |
| Run 4 | 990 | 135 | $\approx 0$ | $\sim$855 | 14 |
| **Total** | **4160** | **599** | — | **$\sim$3561** | **14** |

As discussed in Section 4.3.2, the sand layer reached field capacity during run 1, after which $\Delta S$ was effectively zero at the monitored locations. Even for run 1, the storage term is small relative to the total inflow. While some storage may have occurred deeper in the sandy layer, this cannot account for the large discrepancy between inflow and outflow. The residual $L$ therefore dominates the water balance in every run, accounting for approximately 83–87% of the applied volume. Standing water was observed adjacent to the setup both during and after the experiments (Figure 4.7), suggesting that this residual reflects leakage through pathways not captured by the PVC drains rather than undetected storage.

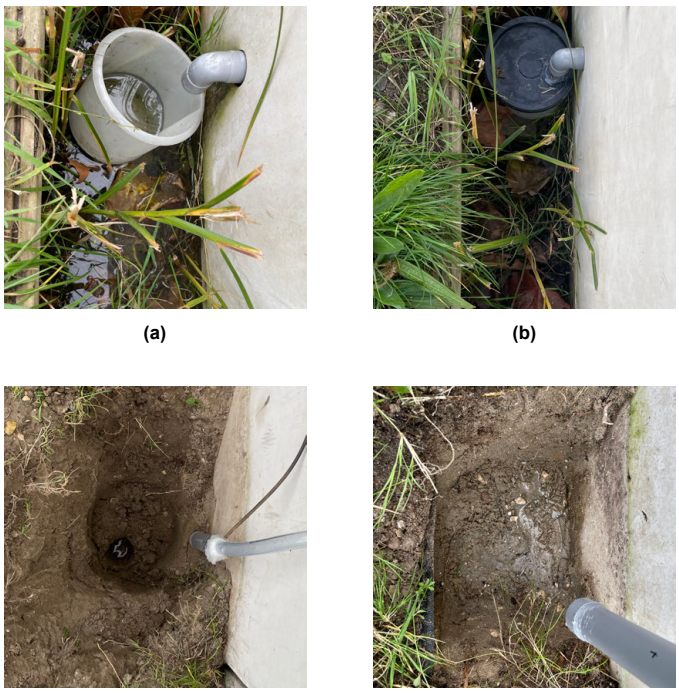



**Figure 4.7:** Observed leakage during and after the experiment: (a) leakage pool during the experiment, (b) dried pool the morning after the experiment, (c) and (d) increased water level next to the setup during the experiment.

## 4.4. Discussion

The results show that, contrary to the hypothesis, no water flowed through the entire bundle, as drain 1 received none; instead, drain 2 was the primary active drain. Drains 3, 4, and 5 (part of the original, schematised in Figure 4.8 remained dry throughout all runs. A closer examination of the designed drain setup found that the drains were constructed slightly differently than designed, allowing water to flow through. The barriers behind the drains, in combination with the drainage tube slope, seem insignificant to generate any flow through these drains. The most plausible flowpath is therefore that water followed the surface of the black plastic, passing through the drains, and reached drain 2, as illustrated schematically in Figure 4.9a, a conclusion further supported by the lack of soil-moisture response at sensor 2-6.

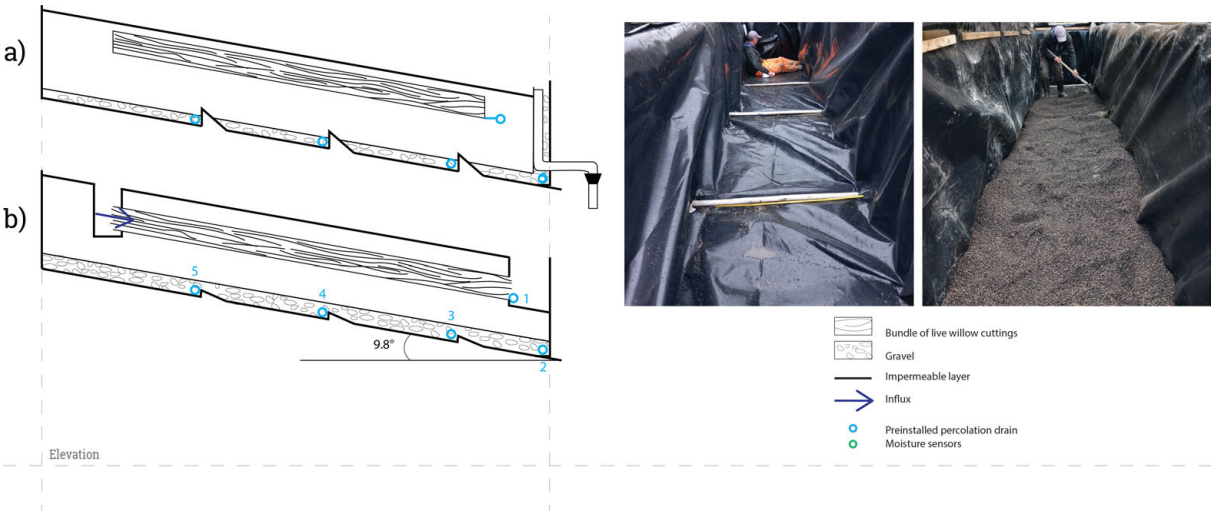



**Figure 4.8:** The observed drains configuration (b) compared to the designed drains (a). Images used in this figure were adapted from Cahill (2024).

When water was applied to the live bundle, no soil moisture response was detected, preventing definitive conclusions about the flowpath. Water potentially percolated vertically between the dead bundles, bypassing the sensors, travelled through the drain and percolated between the sensors, or was distributed primarily toward the bundle lacking sensors, as illustrated in Figure 4.9b. The available measurements do not distinguish between them.

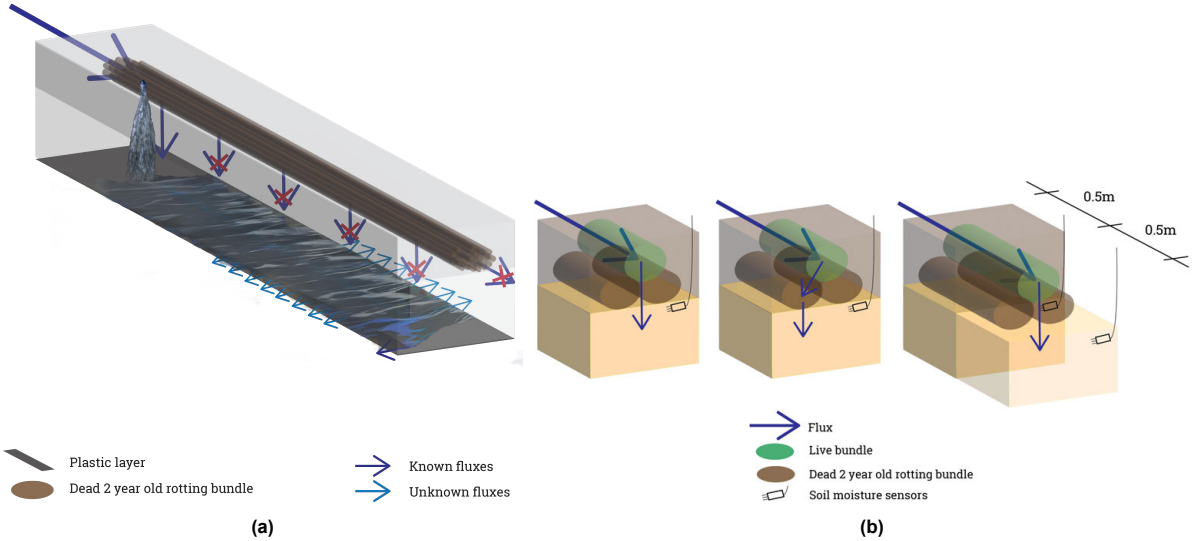



**Figure 4.9:** a) Likely flowpath experiment run 1.1 & run 1.3 b) plausible flowpath run 1.2 & run 1.4.

Water breakthrough at the bottom of the slope was directly observed by excavating a section at the bottom of the slope, as detailed in Appendix C.7. Breakthrough occurred in roughly half the time of the drainage response observed through drain 2 (Figure 4.5), indicating that drain 2 discharge lagged considerably behind actual wetting front arrival. The consistency of the drain 2 breakthrough with the tracer-observed breakthrough of around 60 minutes, detailed in Appendix C.6, further suggests that discharge through drain 2 is likely 'old water', consistent with findings by Tani et al. (2020).

The measured soil moisture values are lower than expected. A porosity of 0.32 measured by Cahill (2024) would suggest a moisture content of 0.32 at full saturation, which is considerably higher than the values observed here. However, Cahill (2024) also measured a field capacity of 0.02 [m3/m3] in the sand layer, and the observed values are consistent with long-term soil moisture data from the other LPD slope measured with Meter TEROS sensors shown in Figure C.7. The observed values are therefore considered physically plausible for the coarse sand.

Figure 4.6 shows that peak soil moisture at sensor 1 was reached within the first hour of wetting front breakthrough. This rapid initial increase could indicate that a degree of bundle flow reached the sensor directly. Following the peak, a gradual decrease in soil moisture was observed in both runs, likely attributable to a combination of percolation threshold activation (Jarvis et al., 2016; McGuire et al., 2024) and progressive preferential flowpath development, both of which would increasingly route water away from the sensor. The overall soil moisture values in run 1.3 were lower than in run 1.1, potentially due to pre-existing preferential flowpaths created during run 1.1 that persisted into run 1.3, although partial closure of these pathways in the intervening days cannot be ruled out.

A local perched water table is a further possible process during injection. If the grown LPD obstructs flow more than anticipated, the high injection flux could cause a local pressure buildup at the base of the bundle (Figure 4.10), accelerating percolation threshold activation (Jarvis et al., 2016; McGuire et al., 2024) and promoting preferential flowpath development below the bundle. However, significant pressure buildup directly above a highly permeable sand layer is unlikely, and no pressure buildup was observed at the surface despite the influx being applied close to it. The decrease in soil moisture after the initial peak (Figure 4.6) may reflect a dissipation of such a perched water table. This process likely acts as a minor contributor alongside the flowpaths discussed above rather than as a dominant mechanism.

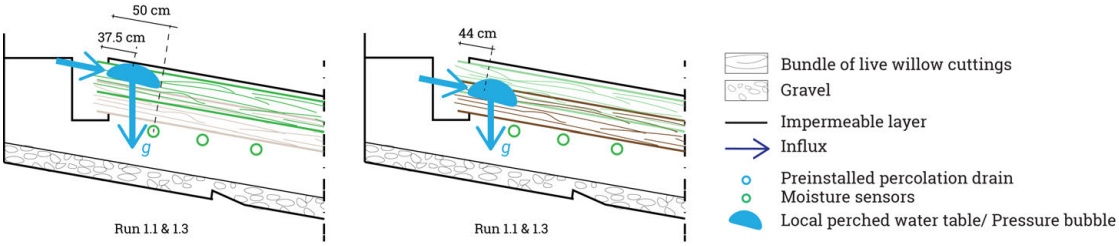



**Figure 4.10:** Potential pressure build-up injection experiment

Several practical limitations affected the experimental conditions across runs. The flow through drain 2 during run 1.1 was notably higher than during runs 1.2–1.3. This is likely attributable to the formation of preferential leakage pathways around the drainage hole following run 1.1, as evidenced by the flow observed alongside the drainage hole from run 1.2 onwards. This effect may have been exacerbated by frost observed on the morning of run 1.2 (Figure D.10), as water retained in the leakage pathway(s) could have expanded upon freezing, further widening existing openings in the plastic outer layer. The stepwise increase in flow measurements through drain 2 across runs could not be attributed to any identified cause. Additionally, the distributed influx hose was found to be partially blocked by algae growth upon inspection after run 1.4 (Figure D.14). As this observation was made only after the final run, the onset of blockage remains unknown. The peristaltic pump is expected to have maintained a consistent discharge volume, as it can overcome the modest increase in back-pressure associated with partial blockage. However, the spatial distribution of the influx may have been affected, potentially altering the flow patterns observed at drain 2.

To assess the robustness of the PVC flow-meter measurements, the sensitivity of the calculated volumes to the choice of calibration fit was evaluated by comparing a third-order polynomial $bx$+ + $cx^2$ + $cx^3$ with an exponential fit $ae^{bx}$, with results presented in Table 4.3 and Figure 4.11. The differences between the two fits are small, suggesting that the PVC flow-meter performed robustly.

**Table 4.3:** Daily pumped volumes and sensitivity to polynomial model choice. The uncertainty band reflects the envelope of the third-order polynomial calibration fit ($bx + cx^2 + cx^3$) to the central polynomial ($ae^{bx}$).

| Day | Date | Central volume [L] | Uncertainty band [L] |
|---|---|---|---|
| Day 1 | 2025-11-11 | 213 | [202, 213] |
| Day 2 | 2025-11-21 | 158 | [143, 158] |
| Day 3 | 2025-11-26 | 134 | [119, 134] |
| Day 4 | 2025-11-27 | 150 | [135, 150] |

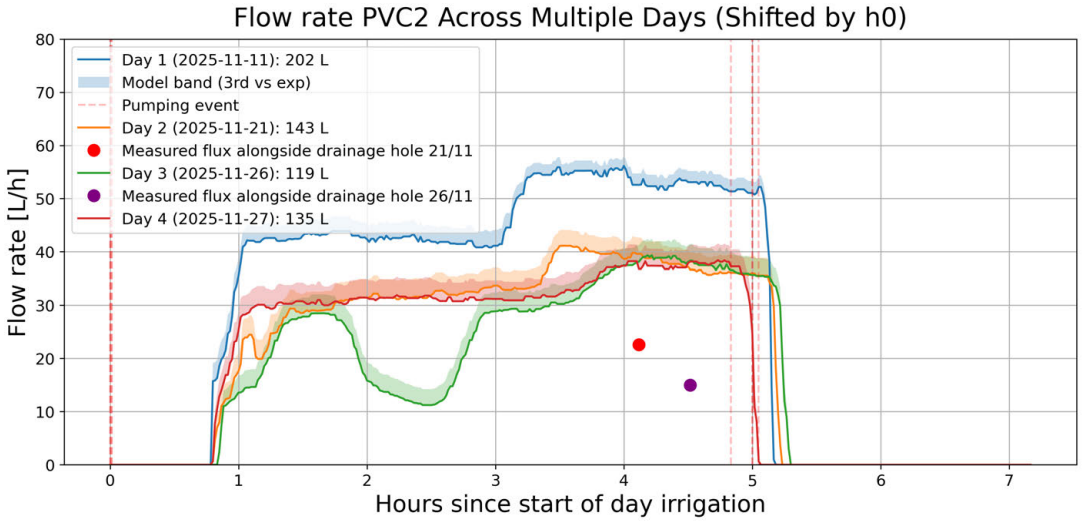



**Figure 4.11:** Sensitivity of the choice of polynomial (2nd/3rd/4th/exponential) in calibration of PVC flow-meter on the flow-measurement, plotted with the third-order polynomial as a reference.

## 4.5. Conclusion and outlook

The hypothesis stated that water entering a bundle is primarily routed through the drain, with antecedent soil moisture controlling whether flux is fully discharged or partially percolates into surrounding soil, and that the location of water input does not influence lateral redistribution between bundles.

Consistent results from the experiment indicate that no water was conveyed through the bundle following PM1 behaviour, as none reached drain 1, and soil-moisture changes were observed only right beneath the applied flux. Contrary to the hypothesis, high antecedent soil moisture resulted in a lower soil-moisture response at the sensor than lower antecedent soil moisture, indicating increased percolation and decreased bundle flow. A leak was observed in the setup, resulting in a loss of ±90% of the applied flux. The rapid breakthrough, combined with the lack of soil moisture response at sensors 2-6, indicated immediate percolation at the influx location. A negligible amount of storage was observed at the setup.

# 5

# Six-Day distributed irrigation: response under sustained wetness

## 5.1. Hypothesis

It is hypothesised that, consistent with the vertical flow dominance observed in the injection experiment, infiltrated water moves predominantly vertically, indicating PM2-type behaviour. However, prolonged irrigation induces localised lateral redistribution of water downslope, detectable as increased soil moisture at depth beyond the irrigated area, indicating PM3-type behaviour. This state-dependent transition from PM2 to PM3 behaviour depends on the activation threshold soil moisture content of the surrounding soil.

## 5.2. Methodology

A second experiment was conducted with the same sensor placement as in the injection experiment, but with a modified irrigation approach: the flux was distributed more evenly over time and reduced in magnitude to promote more gradual infiltration into the soil. The experimental setup is schematised in Figure 5.1.

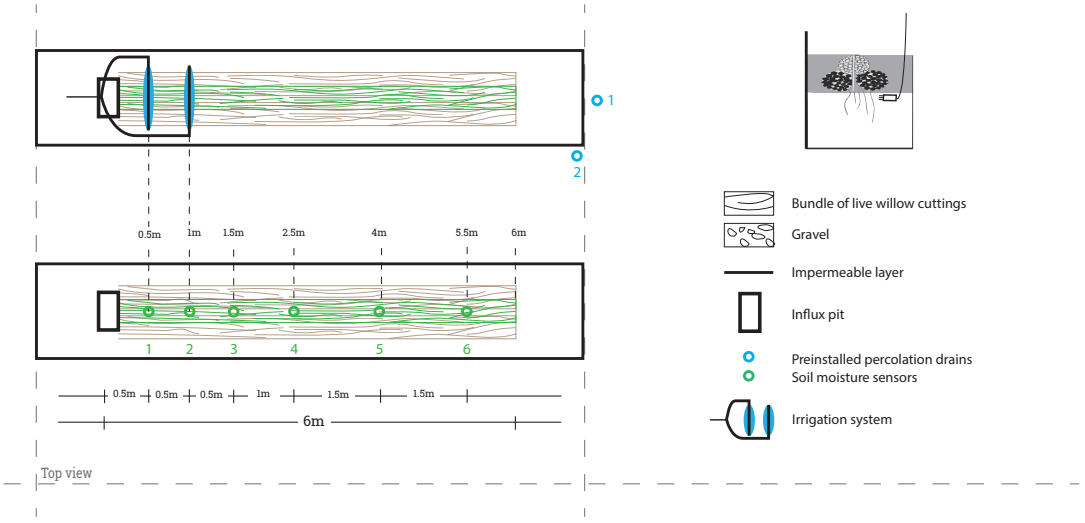



**Figure 5.1:** Schematisation irrigation experiment setup

### 5.2.1. Flux

The experiment spanned six days, with irrigation alternating between a daytime and a nighttime regime, as illustrated in Figure 5.2. The prolonged duration across multiple cycles was intended to capture hysteresis effects in the soil moisture and drainage response (Bordoni et al., 2015). During the day, water was supplied by the peristaltic pump at a controlled rate. The lower nighttime flux was delivered by gravity drainage from an elevated container. As the rain container could not be sealed to maintain a vacuum, it could not be operated as a Mariotte vessel, and the outflow rate therefore decreased over time as the hydraulic head fell with the water level.

The minimum pump capacity of the peristaltic pump corresponds to approximately $24.5\ l/h$, equivalent to a rainfall intensity of $24.5\ mm/h$ over the $1\ m$ irrigated area. For context, this intensity still substantially exceeds the 1000-year return period rainfall event for the Netherlands (Beersma et al., 2019), reflecting the practical constraints of the laboratory setup rather than an attempt to simulate a realistic precipitation scenario. However, LPD are typically applied where runoff is collected from a larger contributing area (Campbell et al., 2008); when viewed in this context, the applied flux constitutes a physically plausible forcing.

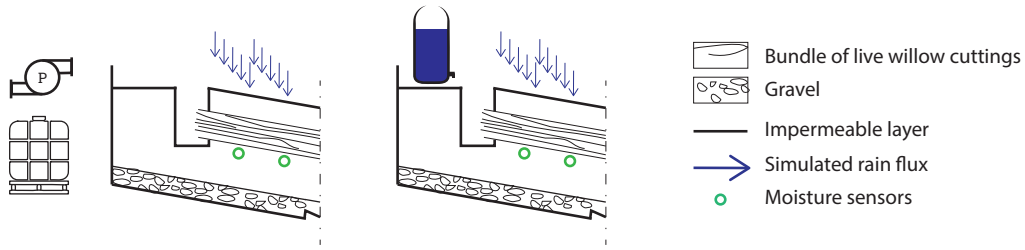



**Figure 5.2:** Daytime and nighttime irrigation regimes

To quantify the inflow, first- and second-order polynomials were fitted to the tank drawdown data, following the same approach as in the injection experiment. The resulting flux over time and the daily and nightly volumes are presented in Figure 5.3 and Table 5.1, respectively.

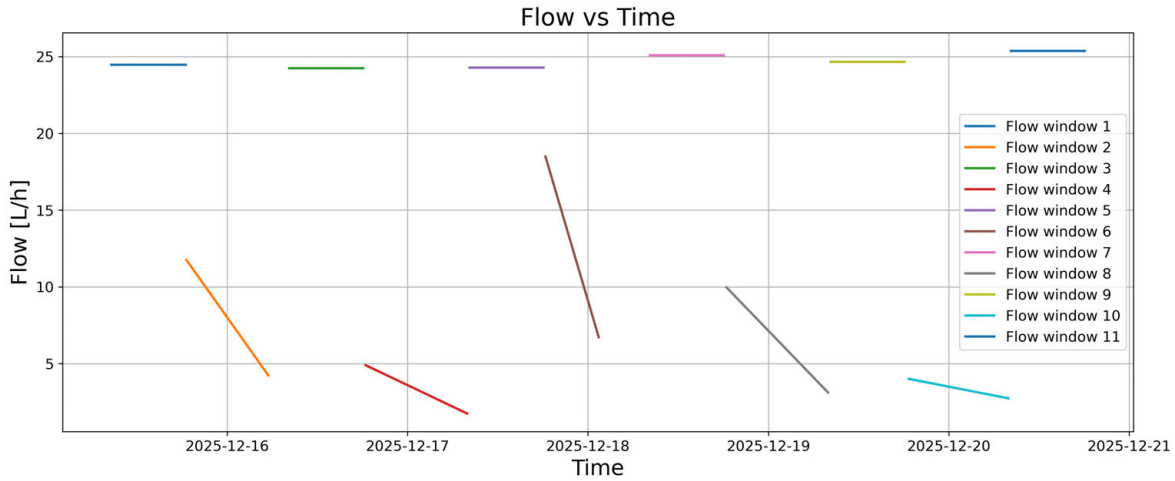



**Figure 5.3:** Flux in irrigation experiment

| Day | Day volume [L] | Night volume [L] | Total volume [L] |
|---|---|---|---|
| 1 | 243 | 87 | 330 |
| 2 | 238 | 45 | 283 |
| 3 | 239 | 89 | 328 |
| 4 | 247 | 88 | 335 |
| 5 | 242 | 45 | 287 |
| 6 | 250 | – | 250 |
| | | Total volume [L] | 1813 |

**Table 5.1:** Pumped influx volume (Day, night and total) irrigation experiment

### 5.2.2. Irrigation

To achieve an even spatial distribution of water across the irrigated area, two irrigation hoses were perforated with a 1.5 mm drill at 1 $cm$ intervals over a 90 $cm$ length. The resulting hoses, along with the nighttime irrigation setup, are shown in Figure 5.4. Equal distribution of outflow was assumed because of irrigation under pressure.



**Figure 5.4:** Drilling of the irrigation hose, resulting 1 cm spaced irrigation holes, and the nighttime irrigation setup.

In an attempt to decrease the gap in the water balance observed in the point influx experiment, the leakage in the setup was investigated by digging up the bottom of the slope, and the observed hole was sealed with a combination of bitumen, 2-component glue, and clay. These are documented in Appendix E.1. The cumulative water balance residual up to day (n) is defined as:

$$R_n = \sum_{i=1}^{n}(L_i) = \sum_{i=1}^{n} P_i - \sum_{i=1}^{n} Q_i - \sum_{i=1}^{n} \Delta S_i \tag{5.1}$$

where ($P_i$) is the total input volume, ($Q_i$) is the measured outflow, ($\Delta S_i$) the storage and ($L_i$) the leakage residual on day (i). The volume discharged through the drain was calculated from the calibrated flux through drain 2, following the same approach as in the injection experiment, and is presented in Figure 5.6.

## 5.3. Results

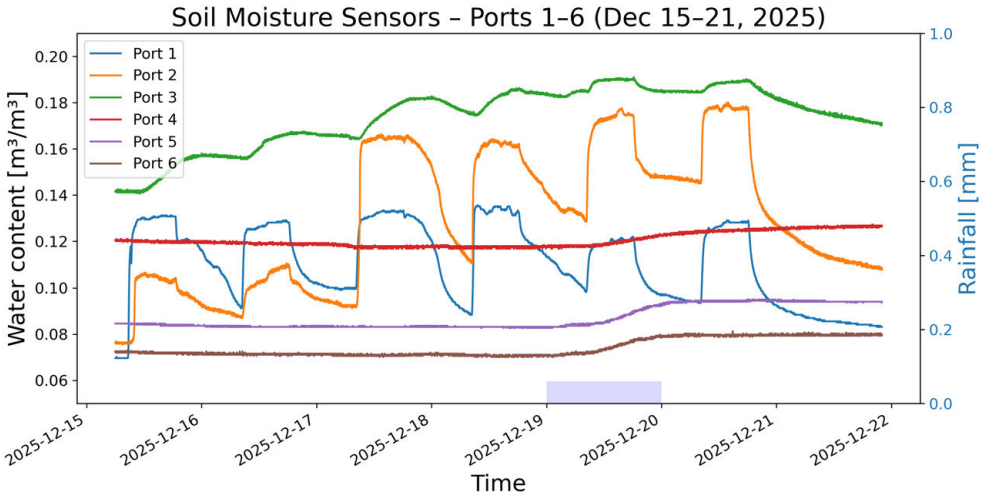



**Figure 5.5:** Soil-moisture data sensor 1-6 [$m^3/m^3$], and rainfall [mm] in a double axes plot, rain-data retrieved from Delft University of Technology (2025).

Soil moisture sensor data from sensors 1 and 2, positioned beneath the 1 $m^2$ irrigated area, are presented in Figure 5.5. Both sensors exhibit a cyclical response that closely mirrors the behaviour observed in the injection experiment, with soil moisture rising rapidly at the onset of each irrigation event and declining sharply once irrigation ceases. Sensor 1 cycled between approximately 0.08 and 0.13 $m^3/m^3$ throughout the experiment, while sensor 2 cycled between 0.08 and 0.17 $m^3/m^3$.

Sensor 2 also exhibits a progressive upward shift in both its inter-cycle baseline and peak moisture values. During the first two days, cycling amplitude and baseline remain modest, but from day 3 onwards, both translate upward together, with the baseline reaching approximately 0.14 $m^3/m^3$ by day 5 before declining again after irrigation ceased on day 6. This behaviour indicates that successive irrigation events deposited more moisture than could drain between cycles, resulting in a gradual accumulation of stored soil moisture in the vicinity of sensor 2, over the course of the experiment.

In contrast to the injection experiment, in which sensor 3 showed no measurable response to any irrigation input, sensor 3 in the irrigation experiment exhibits a clear cumulative increase in soil moisture despite receiving no direct irrigation. Located 0.5 m downslope of the irrigated area, the sensor records a stepwise rise from approximately 0.14 to 0.18 $m^3/m^3$, with each discrete step occurring within a few hours of a corresponding irrigation event. This suggests that moisture arriving at sensor 3 is hydraulically connected to the irrigation cycles and, given the absence of any observed surface flow pathway, is consistent with subsurface lateral transport through preferential flow pathways.

Sensors 4, 5, and 6 positioned progressively farther downslope, showed no measurable response to any of the six irrigation cycles over the six-day experiment. All three sensors responded simultaneously and with approximately equal magnitude to a rainfall event on the fifth day of the experiment (19 December), after which their moisture values remained slightly elevated but stable. The identical timing and magnitude of the rainfall response across sensors 4–6 suggest that these sensors occupy a hydrologically connected zone that, however, remains effectively isolated from the subsurface influence of the irrigated area under the conditions of this experiment.

### 5.3.1. Water balance

Drain 2 discharge is presented in Figure 5.6 and shows a similar response as in the point injection experiment, however had a response time of about 2.5 hours. The 5 hour response time on the first day is due to the filling up of the bottom of the setup before drainage, discussed in Chapter 4.4. The gradual decrease in flow at the end represents the gradual decrease in nightly irrigation flux.

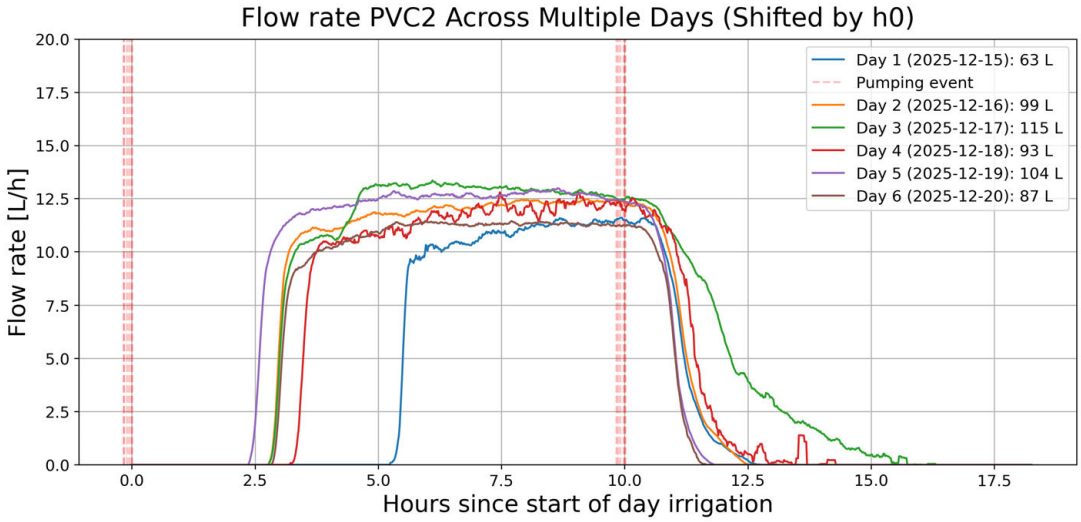



**Figure 5.6:** Outflow through drain 2, irrigation experiment

Soil moisture data from the irrigation experiment indicate a degree of water storage at the sensor locations. To quantify this, the soil moisture readings are assumed to be representative of a cross-sectional area spanning the bundle's total width, with a thickness of 15 cm perpendicular to the slope in both directions, as schematised in Figure 5.7.

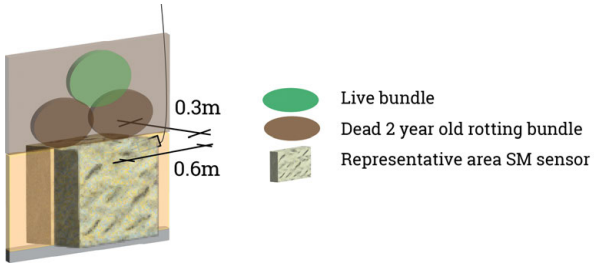



**Figure 5.7:** Representative area soil moisture sensors

The water balance is presented in Table 5.2:

**Table 5.2:** Water balance per day, with $P$ being the pumped volume, $Q$ the flux out through drain 2, $L$ is the residual term including all unmonitored losses and $\Delta S$ the nominal estimated storage around the sensors, detailed in Appendix C.8.

| | $P$ [L] | $Q$ [L] | $\Delta S$ [L] | $L$ [L] | $Q/P$ [%] |
|---|---|---|---|---|---|
| Day 1 | 330 | 63 | $+5.6$ | 261.4 | 19.1 |
| Day 2 | 283 | 99 | $+1.4$ | 182.6 | 35.0 |
| Day 3 | 328 | 115 | $+3.3$ | 209.7 | 35.1 |
| Day 4 | 335 | 93 | $+3.9$ | 238.1 | 27.8 |
| Day 5 | 287 | 104 | $-3.2$ | 186.2 | 36.2 |
| Day 6 | 250 | 87 | $-3.1$ | 166.1 | 34.8 |
| **Total** | **1813** | **561** | $+7.9$ | **1206.2** | **33.0** |

As shown in Figure 5.8, the residual exhibits an approximately linear increase with time, with an $R^2 = 0.997$, implying that the daily imbalance remains approximately constant over the observation period. The interpretation of this linear trend is addressed in Section 5.4.

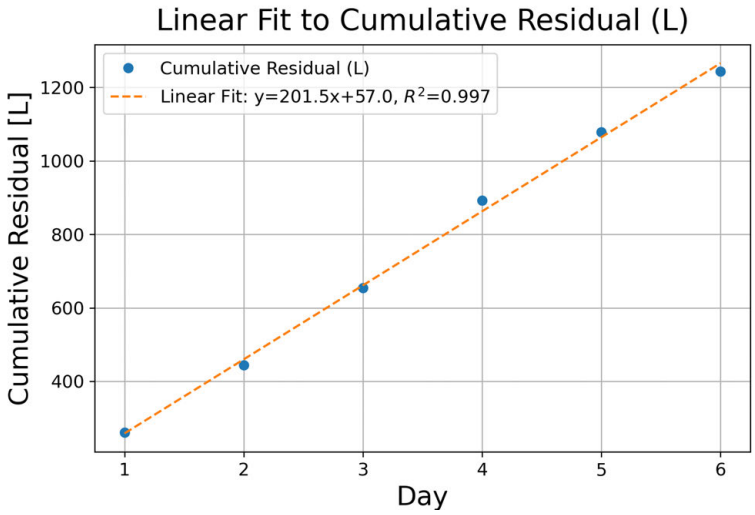



**Figure 5.8:** Cumulative residual water balance, with linear fit.

## 5.4. Discussion

The shifting baseline and maxima at soil moisture sensor 2, compared to a more constant baseline at sensor 1 indicate that the moisture distributed unevenly and concentrated more downslope. The progressive shift in baseline across successive day/night cycles is consistent with hysteretic behaviour (Bordoni et al., 2015), whereby the system retains memory of previous wetting states. Together with the increase in soil moisture at sensor 3, this indicates the presence of lateral subsurface flow in the direction of the bundle. However, surface ponding was observed downslope of the lower irrigation hose, indicating some extent of overland flow. Part of the increased soil moisture at sensor 3 could therefore reflect overland flow rather than subsurface flow through the bundle. The baseline at sensor 2 begins increasing only on the third day of irrigation. This could be attributed either to threshold-dependent activation of a subsurface flowpath, consistent with the well-established threshold dependence of preferential flow across scales (Hendrickx & Flury, 2001; Nieber & Sidle, 2010; Tromp-van Meerveld & McDonnell, 2006), or to an observed subtle shift in irrigation partitioning between the upper and lower hoses at the upstream split (Figure 5.9a), which may have altered the distribution of applied water. In addition, uneven partial clogging of the hoses cannot be ruled out, consistent with observations during the analysis of the point injection experiment.

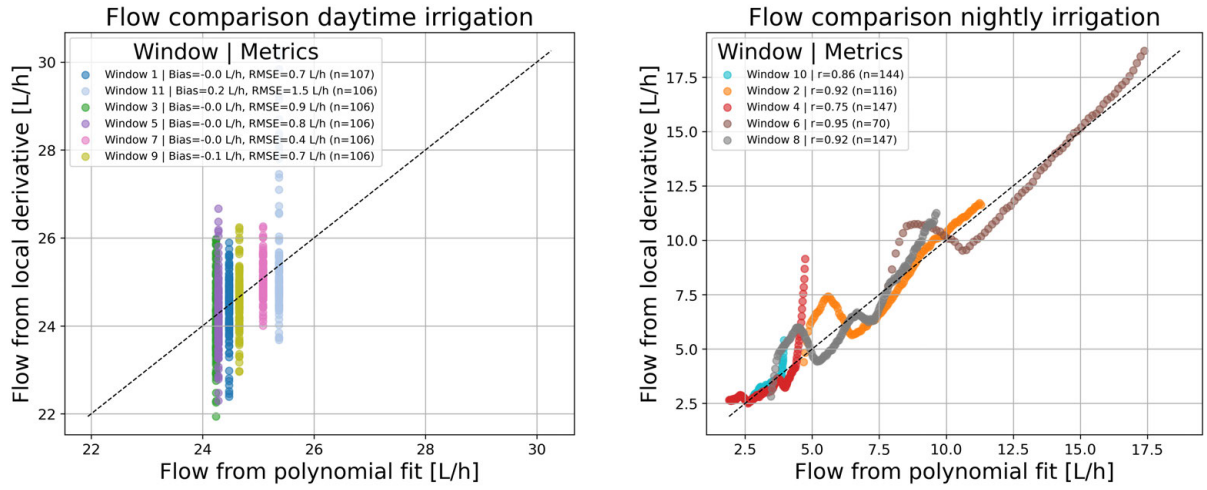
The water balance shows that the leakage decreased due to the repair; however, it did not completely prevent it. Since leakage $L$, including all monitored losses, behaved linearly, it is likely that it consists largely of leakage. As other (temporary) 'loss' processes, such as unmonitored storage, do not behave linearly. The sensitivity of the calculated storage component to the choice of representative width around the sensor is presented in Appendix C.8.



**(a)** **(b)**

**Figure 5.9:** (a) Irrigation split connected to nightly irrigation. (b) Surface ponding downslope of lower irrigation hose (2025-12-16 08:15).

The flux calculated using the local mean of the drawdown data, after application of a 12-point rolling mean, is notably different from the flux calculated from the fitted drawdown. The correlation between the flux calculated using the local derivative and the flux derived from the fitted polynomial functions is shown in Figure 5.10. For the nighttime fluxes, the Pearson correlation coefficient is used, as both time series exhibit variability. In contrast, the daytime flux obtained from the polynomial fit is constant; therefore, correlation metrics are not applicable. Instead, the root mean square error (RMSE) and bias are computed. These metrics are reported in the label of Figure 5.10.




**(a)** Daytime irrigation

**(b)** Nighttime irrigation

**Figure 5.10:** Comparison of flow estimates derived from polynomial fitting and from local differentiation applied to a 12-point rolling mean, for daytime and nighttime irrigation periods.

Figure 5.11 shows that the error is not evenly distributed. The relative difference indicates that the discrepancies are most pronounced during high and low flow conditions. Given that the fitted polynomials exhibit very good agreement with the data, these differences are likely attributable to temporal variations in the effective tank cross-sectional area. In the analysis, the tank cross-section is assumed to be constant (equation 4.1), whereas in reality it tapers slightly toward the top and bottom, as shown in Figures D.21 and D.20.

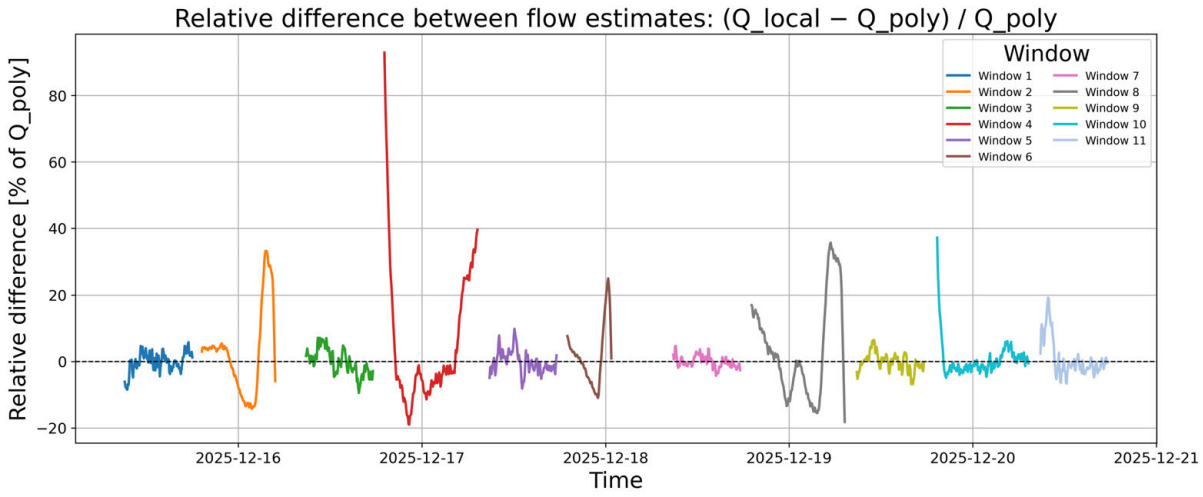



**Figure 5.11:** Relative difference between flow estimates: $(Q_{\text{local}} - Q_{\text{poly}})/Q_{\text{poly}}$.

### 5.4.1. Sensitivity water balance.

As for the injection experiment, the choice of the calibration polynomial for the PVC flow meter affects the flow calculation. This sensitivity, comparing the 3rd order polynomial fit to the exponential fit, both with $R^2 > 0.995$, is presented in Table 5.3 and Figure 5.12.

The sensitivity of the estimated storage component to the chosen representative area width is shown by the bands in Figure C.13, corresponding to thicknesses ranging from 10 to 50 cm.

**Table 5.3:** Daily pumped volumes and sensitivity to polynomial model choice. The uncertainty band reflects the envelope of the third-order polynomial calibration fit ($a + bx + cx^2$) relative to the central exponential fit ($ae^{bx}$).

| Day | Date | Central volume [L] | Uncertainty band [L] |
|---|---|---|---|
| Day 1 | 2025-12-15 | 63 | [63, 81] |
| Day 2 | 2025-12-16 | 99 | [99, 125] |
| Day 3 | 2025-12-17 | 115 | [115, 146] |
| Day 4 | 2025-12-18 | 92 | [92, 116] |
| Day 5 | 2025-12-19 | 104 | [104, 131] |
| Day 6 | 2025-12-20 | 87 | [87, 111] |

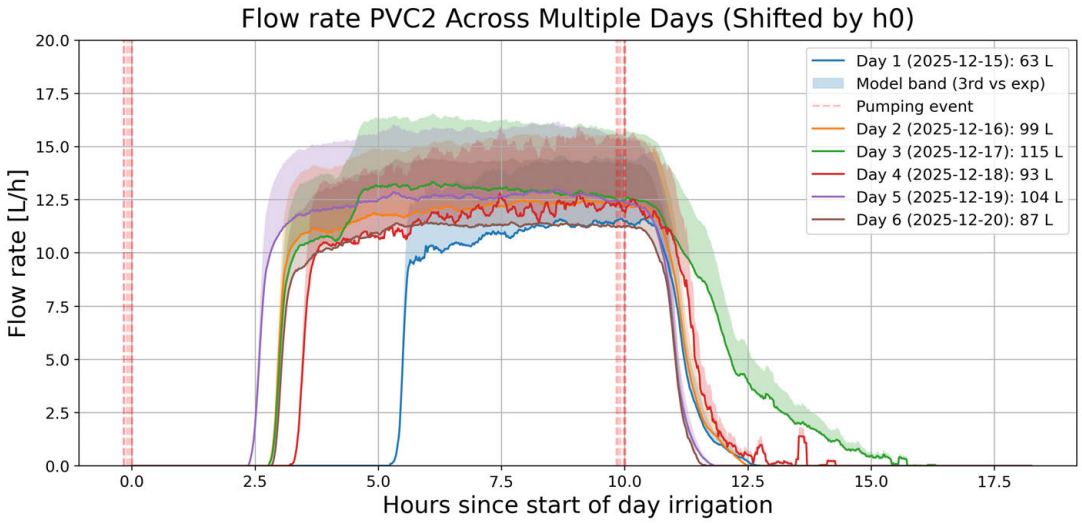



**Figure 5.12:** Sensitivity of the choice of polynomial (2nd/3rd/4th/exponential) in calibration of PVC flow-meter on the flow-measurement, plotted with the third-order polynomial as a reference.

## 5.5. Conclusion and outlook

The sustained distributed irrigation experiment provided evidence in support of both components of the hypothesis. Consistent with the point injection experiment, initial infiltration behaviour was indicative of PM2-type flow, with water moving predominantly vertically through the permeable sand layer, as further evidenced by the rapid breakthrough and initiation of flow through drain 2. The state-dependent activation threshold was reached almost immediately, as evidenced by the increase in soil moisture at sensor 3 downslope of the irrigated area, confirming the hypothesised transition to PM3-type lateral redistribution. The rapid threshold activation is attributed to the distributed nature of the flux in this experiment, supporting the reasoning that the activation threshold is primarily governed by the antecedent soil moisture of the surrounding soil. Storage within the setup was confirmed but proven to be minimal, with an estimated volume of 7.8 L. Leakage remained a significant source of loss, accounting for approximately 67% of total outflow, and, while reduced compared to the injection experiment, the persistent linear residual in the outflow signal provides evidence that leakage was the dominant process driving this baseline loss. Additionally, the flow meter used for drain 2 exhibited greater calibration uncertainty than the same drain in the injection experiment (±20%).

Further research recommendations include: 1) quantifying the LPD activation threshold (Tromp-van Meerveld & McDonnell, 2006). 2) Increased sensor density near the influx alongside the bundle to investigate if the LPD's activation indeed mostly depends on lateral soil moisture, as the results of this study indicate. 3) Subjecting the setup to an even lower and longer irrigation event to resemble actual precipitation events. 4) Improve the irrigation setup to facilitate equal or at least constant distribution of water in the irrigated area. The conclusions of this study are limited by uncertainty in this flux distribution. 5) In future setups, preventing perforation of the impermeable plastic outer layer; instead, applying other drainage systems (like one that automatically pumps when water reaches a certain level). Even three-way repair attempts with 2-component rubber glue, bitumen, and clay did not tightly seal the hole.

# 6

# Mini-Disk Infiltrometer measurements: impacts of LPD on infiltration

## 6.1. Hypothesis

It is hypothesised that the spatial distribution of macropore conductivity and its associated contribution to the infiltration flux is highly influenced by the LPD. Through root growth and biological activity, the LPD increases matrix infiltration capacity. Due to the random variability of hydraulic conductivity on hillslopes (Dunne et al., 1991), this effect is spatially heterogeneous across the slope. It is further hypothesised that, since the live bundle lies directly beneath the soil surface, the LPD's influence is especially pronounced directly above the bundle.

## 6.2. Methodology

A mini-disk infiltrometer was used to estimate the hydraulic conductivity $K(\psi)$ as a function of suction $\psi$. This $K(\psi)$ represents a lumped parameter that integrates the net effect of several interacting soil physical processes, rather than isolating a single mechanism.

Two main flow domains in field infiltration are matrix flow, occurring through the fine-to-medium pore network, and macropore flow, occurring through biopores, cracks, and inter-aggregate channels (K. Beven & Germann, 1982). A 2 $cm$ suction rate was chosen to limit the effects of inhomogeneous wetting of the disk, which K. R. Close et al. (1998) found to be higher for high tensions. The choice of suction rate was also constrained by the experimental time limit. METER Group (2021) recommends 30 $ml$ infiltrated volume, related to the requirement of observing a linear trend in cumulative infiltration (Zhang, 1997). This took about 15 minutes to infiltrate under 2 $cm$ suction and enabled taking 40 point measurements. K. Beven and Germann (1982) indicate that the suction induced by the infiltrometer ensures that only hydraulically connected pores are activated, thereby providing an indication of channelling macroporosity.

The representative diameter of evaluated/regarded pores under suction was calculated using the flow-weighted mean pore diameter equation (Angulo-Jaramillo et al., 2016):

$$R_0 = \frac{\sigma}{\rho_w \, g \, \phi_0} = \frac{\sigma \, \alpha(h_0)}{\rho_w \, g} \tag{6.1}$$

where $R_0$ is the characteristic pore radius (m), $\sigma$ is the surface tension of water (N m$^{-1}$), $\rho_w$ is the density of water (kg m$^{-3}$), $g$ is gravitational acceleration (m s$^{-2}$), $\phi_0$ is the matric flux potential at suction $h_0$ (m$^2$ s$^{-1}$), and $\alpha(h_0)$ is the van Genuchten $\alpha$ parameter evaluated at the applied suction $h_0$ (m$^{-1}$). With $\sigma = 0.07497$ N m$^{-1}$, $\rho_w = 999.97$ kg m$^{-3}$, $g = 9.81$ m s$^{-2}$, and $\alpha = 0.036$ cm$^{-1}$ $= 3.6$ m$^{-1}$ (physical properties of water at 5°C). Carter and Gregorich (2008) reasons that this flow-weighted mean is not the actual pore radius, but just a measure for the pores that are hydraulically active.

$$R_0 \approx 2.75 \times 10^{-5}\,\text{m} = 0.275\,\text{mm}$$

At a suction of 2 $cm$, pores with an equivalent radius larger than 0.275 $mm$ are thus excluded. Therefore, effectively measuring infiltration dominated by matrix flow. A 2 $cm$ suction is low enough to capture the near-saturated hydraulic conductivity relevant to most natural rainfall intensities, while high enough to suppress the most extreme preferential flow paths, which are spatially erratic and not representative of slope-scale infiltration behaviour.

Mini disk infiltrometer measurements are taken according to the protocol in Appendix A following the grid, presented in Figure 6.1. As the infiltrometer measurements are non-invasive and infiltrate minimal water, measurements were taken on slope 2 (Figure 3.1), as prior experiments might have altered soil compaction by subjecting it to volumes of water larger than those of typical rainfall events. The unsaturated hydraulic conductivity was determined using the Zhang (1997) as provided by METER Group (2021), as this method is more reliable than alternatives, under the condition that the Van Genuchten parameter n exceeds the threshold of 1.35, below which this method is invalid (Dohnal et al., 2010). This method assumes homogenous $\alpha$; in this case, a standard value for loam soils was used, based on the Van Genuchten parameter n = 1.56, provided by METER Group (2021).

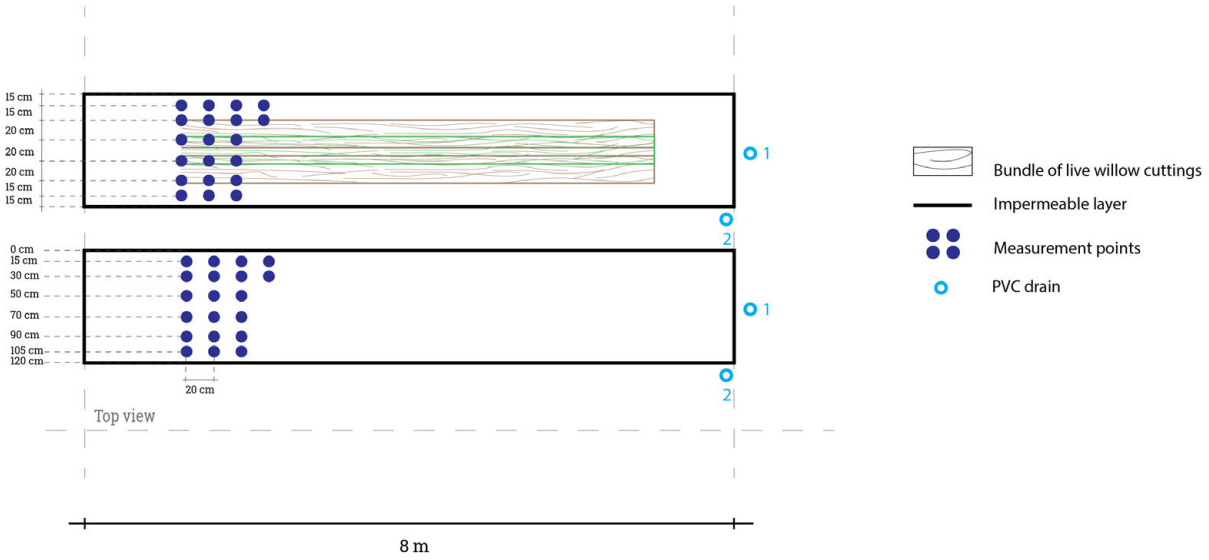



**Figure 6.1:** Measurement grid infiltrometer experiment

## 6.3. Results

The main factor of interest in the results of the $K(-2\text{ cm})$ is the variability across and between the slopes. Figure 6.2 shows that the $K(-2\text{ cm})$ of the bare slope is more concentrated compared to the LPD-slope, which contains higher values, especially in the upper tail. Figure 6.2a specifically shows this increased variance in a box plot, with a 74.7 % increase in interquartile range (IQR) and a median of 3.11 $10^{-4}$ [$cm/s$] compared to 2.78 $10^{-4}$ [$cm/s$] on the bare slope. Indicating, this increased spread mostly stems from the higher values.

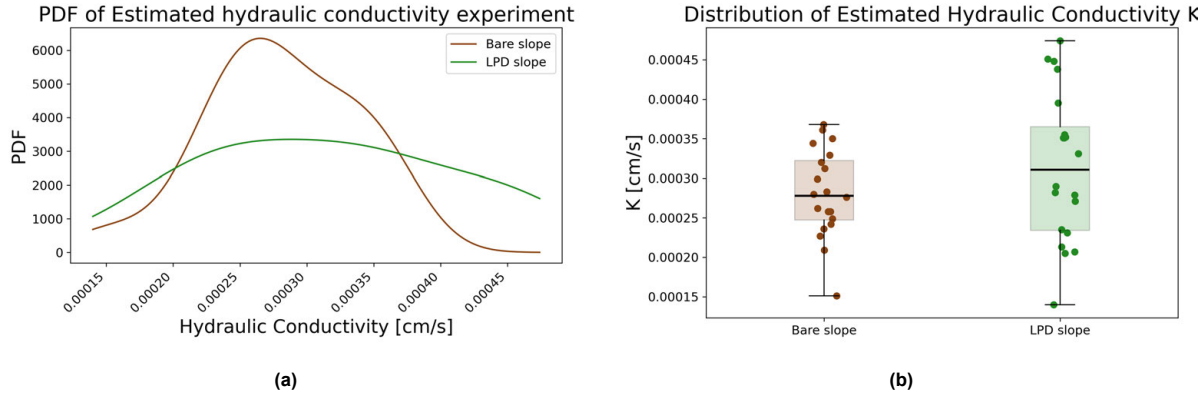



**Figure 6.2:** (a) PDF of the estimated hydraulic conductivity measurements during the infiltrometer experiment. (b) Box plot of the distribution of estimated hydraulic conductivity on the bare slope and the LPD slope. The individual measurements that the box plot is based on are plotted as scatter points to highlight that it is based on a limited number of points.

The increased variability of K observed in Figure 6.2 is quantified by a higher coefficient of variation of $K(-2)$ on the LPD slope (CV = 0.302), than on the bare slope (CV = 0.198)and a greater IQR of raw $K(-2)$ on the LPD slope (IQR $= 1.31 \times 10^{-4}$ m s$^{-1}$) than on the bare slope (IQR $= 7.5 \times 10^{-5}$ m s$^{-1}$). Levene's test indicated that the difference in variance of $\log_{10}(K(-2))$ between slopes is unlikely to have arisen by chance ($p = 0.049$), providing formal statistical support for the greater spread of $K(-2)$ observed on the LPD slope.

The unsaturated hydraulic conductivity on the bare slope was hypothesised to be randomly distributed; measurements directly on top of the live bundle, however, were hypothesised to show increased conductivity. The $K(-2)$ values are presented in Figure 6.3 against their measurement location, which demonstrates that this indeed seems to be slightly higher. However, these are not the main measurements that resulted in the increased spread in the lumped box plots above. The measurements furthest away from the live bundle showed the largest increase. The lumped box plots without these points are given in Figure C.18.

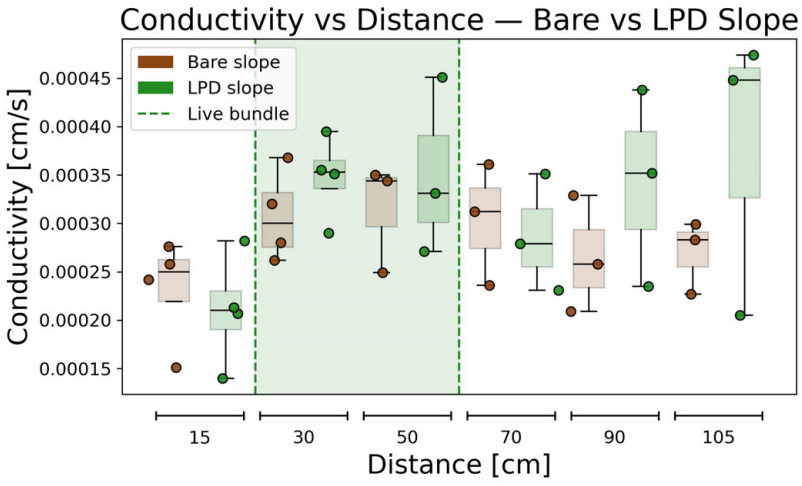



**Figure 6.3:** Box plot of the distribution of estimated hydraulic conductivity plotted against distance from the side of the setup. Note that some boxes are based on as few as three measurements.

## 6.4. Discussion

The distributions of the estimated unsaturated hydraulic conductivity $K(\psi)$ for the bare and LPD slope show consistent output. The IQR for both slopes is small, given that $K$ is logarithmically distributed, shown in Section C.9 and may vary several orders of magnitude over distances of only a few centimetres in structured soils (K. Beven & Germann, 1982). This enables comparison of variability between the slopes, with a roughly 1.5-fold increase in CV on the LPD slope compared to the bare slope. In addition, Levene's test ($p = 0.049$) confirms a significant increase in variance. This should, however, be interpreted with caution, given the limited sample size (n = 20). The applied 2 cm suction suppresses flow through the largest macropores; the increased variability on the LPD slope, characterised by predominantly higher outliers, therefore likely reflects spatially heterogeneous improvements in soil structure. This is consistent with Qin et al. (2022), who attributes higher permeability under vegetation to greater macroporosity, enhanced soil aggregation, and increased biological activity.

Prior to this experiment, vegetation was removed from the slope surfaces, as shown in Figures D.1 and D.2. This may have altered near-surface infiltration behaviour in ways that would not reflect the slopes' natural state, and to which the mini disk infiltrometer is particularly sensitive. Minor topsoil disturbance was also introduced during placement, as lightly twisting and pressing the disk was necessary to ensure adequate hydraulic contact on the slope surface. This was applied consistently across all measurement locations. If systematic surface sealing had occurred, it would likely have produced either extremely low outliers or convergence of $K(\psi)$ estimates across slopes, neither of which was observed. Wind occasionally disrupted hydraulic contact during measurements and in several instances tipped the infiltrometers entirely, though Bagarello et al. (2001) demonstrates that temporary removal does not introduce substantial error. Wind-induced vibration was limited by supporting the infiltrometers with planks, as shown in Figure D.31. The METER Group (2021) Macro applies Zhang (1997)'s estimation method to derive unsaturated hydraulic conductivity, which assumes that the $\alpha$ parameter is spatially homogeneous and representative. This assumption is unlikely to hold strictly in the field; however, since both slopes share the same texture class and the same tabulated value is applied uniformly, its effect on the relative comparison between slopes is assumed to be limited. The method also overestimates $K(\psi)$ (Dohnal et al., 2010), in part because infiltration under a tension infiltrometer includes flow into dead-end macropores that lack continuity throughout the wetting depth (Allaire et al., 2009). A further limitation is that the representative wetting depth is poorly defined, with estimates ranging from 0.05 to 0.07 $m$ (Allaire et al., 2009). Given that the loam layer extends much deeper than this, the measurements may only represent a shallow, poorly defined near-surface zone. This zone, however, is precisely where rainfall first infiltrates, so its hydraulic behaviour remains directly relevant to the processes of interest.

Angulo-Jaramillo et al. (2016) indicate that measurements performed without a contact layer may systematically yield lower infiltration rates due to imperfect disk–soil contact. Since no contact layer was applied on either slope, any resulting downward bias in $K(-2)$ is expected to affect both slopes equally, preserving the validity of relative comparisons between treatments. Furthermore, as K. R. Close et al. (1998), Minasny and McBratney (2000), and Bagarello et al. (2001) detected contact-induced variability using sample sizes smaller than the n=20 employed here, the present sample is considered sufficient to capture the range of contact conditions on both slopes. Contact-induced uncertainty is therefore assumed to contribute comparably to the variance of $K(-2)$ on each slope, and does not systematically explain the greater spread observed on the LPD slope. The small measurement surface of the mini disk infiltrometer has both advantages and disadvantages. On one hand, it captures localised preferential flow pathways that a larger device would average out. On the other hand, edge effects and placement irregularities represent a proportionally larger fraction of the total measurement area, increasing sensitivity to measurement error.

Continuous soil moisture measurements on the LPD and control slopes by F. Berlitz using the smart sensor setup (Appendix E) are shown for the experiment days in Figure 6.4. Antecedent soil moisture on the LPD slope was consistently higher than on the control slope. $K_{unsat}$ is highly sensitivity to soil moisture (Van Genuchten, 1980). An indicative calculation using the Van Genuchten (1980) closed-form expression for relative hydraulic conductivity,

$$\Theta = \frac{\theta - \theta_r}{\theta_s - \theta_r}$$

$$K_r(\Theta) = \Theta^{1/2}\left[1 - \left(1 - \Theta^{1/m}\right)^m\right]^2, \quad m = 1 - \frac{1}{n}$$

together with the Guelph loam wetting parameters from Table 2 of Van Genuchten (1980) ($\theta_r = 0.218$, $\theta_s = 0.520$, $n = 2.03$), a small moisture increase from $\theta = 0.24$ to $\theta = 0.25$ raises $K_r$ from $2.3 \times 10^{-6}$ to $1.2 \times 10^{-5}$. This is a factor of roughly 5. The steep sensitivity of $K_r$ to small moisture changes near residual water content is a general feature of the van Genuchten model, and the Guelph loam parameters serve here only as an illustrative example. The factor 1.2 difference in median $K(-2)$ between slopes might therefore be fully explained by differences in soil moisture alone.

The higher antecedent soil moisture on the LPD slope itself is, however, a consequence of the LPD. The resulting increased median of $K$, therefore, is a hydrological effect. Moisture differences alone, however, do not explain the increased variance on the LPD slope. A uniform moisture difference would shift the entire $K$ distribution rather than selectively inflate its upper tail. Point-based smart sensor measurements cannot determine whether the moisture increase on the LPD slope is spatially uniform or heterogeneous. The structural improvements proposed earlier are themselves a plausible cause of the higher antecedent moisture on the LPD slope, since changes in hydraulic conductivity and water retention will affect how much water the soil holds between events. The difference in antecedent moisture between the two slopes, therefore, does not undermine the infiltrometer results. It is instead consistent with what increased soil structure and aggregation would predict.

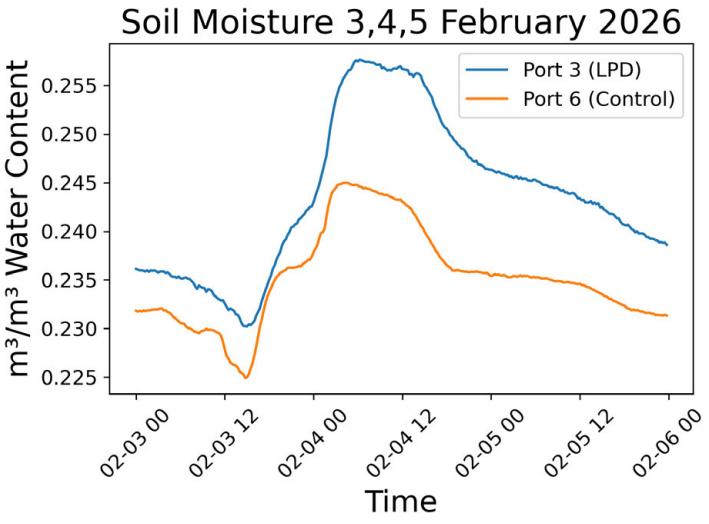



**Figure 6.4:** Soil moisture values from 3,4,5 February from LPD slope 2 and the control slope at the top smart sensor, Figure E.2, at 20 cm depth (*data from personal communication F. Berlitz*).

## 6.5. Conclusions and outlook

Experiment 3 provided partial support for the hypothesis of PM4 behaviour. The LPD slope exhibits a significantly greater variance in $K(2)$, characterised by predominantly higher outliers in the upper tail of the distribution. This pattern is consistent with a spatially heterogeneous increase in macropore conductivity, attributable to root growth and biological activity associated with the LPD. This elevated upper-tail variability is indicative of PM4-type behaviour, in which localised preferential flow pathways disproportionately contribute to the infiltration flux. The higher median $K(-2)$ on the LPD slope further supports the hypothesis of an overall increase in matrix infiltration capacity. The results do not support the hypothesis that the LPD's influence is especially pronounced directly above the bundle.

More infiltrometer measurements, approaching the sample size of 149 used by Gadi et al. (2017) and distributed across a wider range of locations, would improve characterisation of the spatial variability in $K$ on both slopes. The measurement quantity was largely constrained by the need to manually transcribe results; future experiments could therefore employ an automated infiltrometer capable of directly recording pressure changes, as demonstrated in Di Prima et al. (2016) and Casey and Derby (2002). Furthermore, although the comparative nature of this analysis does not strictly require a contact layer, future experiments are recommended to apply one, in line with the consistent recommendations in the literature (Angulo-Jaramillo et al., 2016; Bagarello et al., 2001; K. R. Close et al., 1998; Minasny & McBratney, 2000). Tension infiltrometer measurements could also be combined with dye tracing to better characterise the spatial distribution and variability of wetting fronts (K. R. Close et al., 1998).

In this experiment, measurements were restricted to the top of the slope, despite soil moisture typically increasing downslope on larger hillslopes (Dunne et al., 1991). It would therefore be valuable to investigate whether this pattern holds at the relatively small scale of the OAL, and how any such gradient interacts with the LPD. Additionally, given the strong influence of antecedent moisture conditions on estimated hydraulic conductivity, repeating this experiment across varying moisture conditions would provide valuable insight into the robustness of the observed differences between slopes.

# 7

# Siphonic Flow Meter

Discharge through the drains in the experimental setup was designed to be monitored using tipping buckets. However, tipping buckets presented several practical limitations: they were not readily available for all drains, have a limited dynamic measurement range, and are sensitive to mechanical wear. To address these constraints, this study adopted low-cost, high-measurement-range calibrated PVC pipe flow meters, introduced in Chapter 3.2, to measure discharge. While these provided continuous measurements, they are methodologically sensitive to cumulative error propagation, in which small systematic biases compound over time and degrade measurement accuracy. A novel siphonic flow meter was developed to address these limitations, enabling cumulative flow measurement without the overflow constraints of fixed-volume containers. Given the scope of the present thesis, instrument development was pursued to the extent permitted by practical constraints.

## 7.1. Design and Construction

The siphon flow meter combines continuous pressure sensing with periodic emptying to enable cumulative flow measurement. Figure 7.1 illustrates the device geometry. A pressure sensor mounted within continuously measures water height as inflow accumulates. When the water level reaches the apex of the inverted U-tube, hydrostatic pressure differential initiates auto-siphonage, draining the chamber contents through the outlet. Once the water level recedes to the inlet of the U-tube, air enters the tube, disrupting the continuous water column and terminating flow. The siphon remains inactive until the rising water level again submerges the apex.

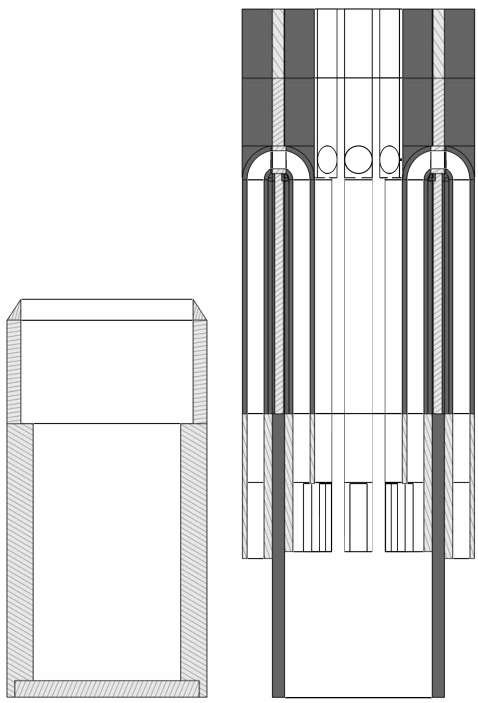


**Figure 7.1:** Siphon flow meter schematic showing the inlet chamber with space for a pressure sensor, inverted U-tube siphon conduit, and outlet. The pressure sensor provides continuous water-level measurements, while the siphon mechanism prevents overflow by periodically resetting the chamber, enabling sustained monitoring. Not to scale.

The raw pressure signal then exhibits a sawtooth pattern: linear increases during chamber filling, punctuated by abrupt drops during siphon discharge events. Post-processing filters out these discharge events, reconstructing a monotonically increasing water height signal that represents the cumulative inflow as if the chamber had infinite capacity:

$$h_{\text{cumulative}}(t) = \begin{cases} \sum_{i=1}^{k} h_i^{\text{reset}} + h_{\text{measured}}(t) & \text{if } t \notin [t_k^{\text{start}}, t_k^{\text{end}}] \\ \sum_{i=1}^{k} h_i^{\text{reset}} + \dot{h}_k \cdot (t - t_k^{\text{start}}) & \text{if } t \in [t_k^{\text{start}}, t_k^{\text{end}}] \end{cases} \tag{7.1}$$

where $h_{\text{measured}}(t)$ is the instantaneous measured chamber height, $k$ is the index of the most recent siphon event, $h_i^{\text{reset}}$ is the chamber height immediately before the $i$-th siphon event, $\dot{h}_k$ is the filling rate estimated from the pressure signal just before the $k$-th siphon event, and $t_k^{\text{start}}$ and $t_k^{\text{end}}$ are the start and end times of the $k$-th discharge period. A synthetic sawtooth raw water height signal and the associated estimated $h_{cumulative}$ are shown in Figure 7.2.

Before applying Equation 7.1, a preprocessing step is required to identify the siphon events and their corresponding time intervals $[t_k^{\text{start}}, t_k^{\text{end}}]$. Two approaches can be used for this detection. The first approach detects $t_k^{\text{start}}$ as the moment the measured water height $h_{\text{measured}}(t)$ begins to decrease, and $t_k^{\text{end}}$ as the moment it starts increasing again, indicating that the siphon has completed and the chamber is refilling. The second approach makes use of the known siphon geometry: $t_k^{\text{start}}$ is identified when $h_{\text{measured}}(t)$ reaches the known maximum water height $h_{\text{max}}$ at which the siphon triggers, and $t_k^{\text{end}}$ is identified when $h_{\text{measured}}(t)$ returns to the known minimum water height $h_{\text{min}}$ corresponding to the end of the siphon discharge. It is hypothesised that the first approach is more robust under field conditions, as turbulent inflow or outflow may cause $h_{\text{measured}}(t)$ to fluctuate around the fixed thresholds $h_{\text{max}}$ and $h_{\text{min}}$, leading to false or missed detections. This hypothesis is to be confirmed through controlled laboratory experiments.

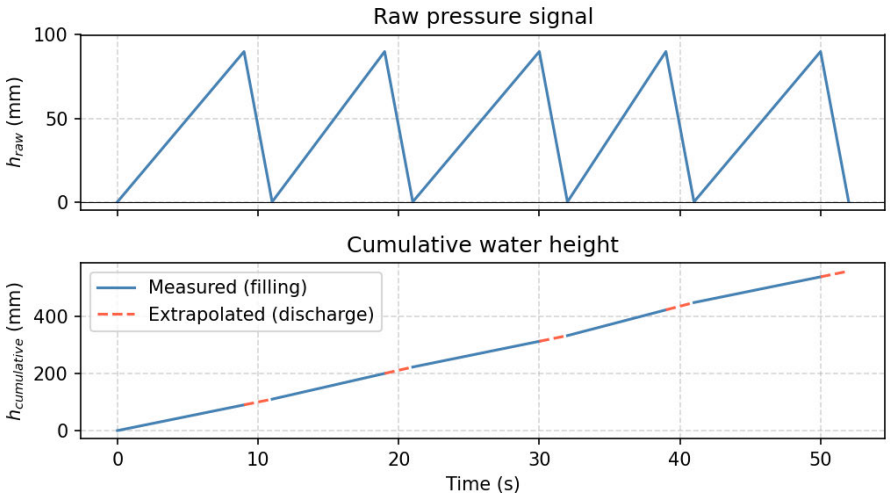



**Figure 7.2:** Conversion of synthetic raw water pressure height ($h$) to associated cumulative water height measurement ($h_{cumulative}$).

Cumulative volume is then determined by the known chamber cross-sectional area of 948.93716 $mm^2$ ($A_{\text{chamber}}$) calculated directly from the 3D model, presented in Figure B.4:

$$V_{\text{cumulative}}(t) = A_{\text{chamber}} \cdot h_{\text{cumulative}}(t) \tag{7.2}$$

Discharge can be derived from the time derivative of the cumulative height record over any measurement interval $\Delta t$:

$$Q(t) = A_{\text{chamber}} \cdot \frac{dh_{\text{cumulative}}}{dt} \approx A_{\text{chamber}} \cdot \frac{\Delta h_{\text{cumulative}}}{\Delta t} \tag{7.3}$$

The prototype was fabricated using fused deposition modelling (FDM) 3D printing with polylactic acid (PLA) filament. Manufacturing parameters were optimised to balance structural integrity with water-tightness: a 0.4 mm nozzle diameter and a 0.15 mm layer height were employed to minimise inter-layer porosity. While this approach enabled rapid prototyping and geometric iteration (see Appendix B.2 for the version history), it introduced material constraints.

## 7.2. Discussion

### 7.2.1. Methodological evaluation

Unlike orifice-based flow meters requiring empirical calibration curves (see Chapter A.2.2), the siphon flow meter's volumetric discharge is geometrically determined by Equation 7.3. This eliminates uncertainty associated with potential calibration drift during deployment. For a PVC flow meter, the systematic uncertainty arises from the pressure sensor resolution and the potential bias between actual flow and calibrated flow. In contrast, for the siphonic flow meter, the accuracy of the flow measurement depends mostly on the pressure sensor's resolution. In principle, a single-dimensional measurement of the fabricated device suffices to calculate the flow.

Water level sensing resolution determines the precision with which the siphon determines the flow. Height resolution of the Keller pressure sensors = 0.5 $mm$, with an area of 948.94 $mm^2$, the volume resolution of the siphonic flow meter = 474.47 $mm^3$ = 0.474 $ml$ per logging interval.]

The extrapolation of water height during siphoning, however, can result in additional error. This uncertainty depends on the flow rate. At very low flow, the chamber filling time becomes much longer than the siphon drainage time, yielding high temporal resolution. Conversely, at high flow rates, the flow will

be much closer to the siphon drainage rate, resulting in a larger blind spot that needs to be extrapolated, and thus higher uncertainty.

As with the PVC orifice flow meter, the logging interval determines how accurately flow dynamics can be captured. Since the device measures groundwater flow, which is generally slow-varying, a relatively coarse interval (e.g., 1 minute) is sufficient and can be easily adjusted for the application via the pressure sensor settings. The siphonic flow meter must be installed level to ensure the apices of the tubes activate evenly.

PLA degrades through hydrolysis under prolonged water exposure (Kubát et al., 2025). Although this typically takes months to years depending on environmental conditions, it fundamentally limits deployment duration. Alternative materials such as ABS, PETG, or polyamide offer better durability but require different printing parameters and may compromise fabrication precision.

### 7.2.2. Practical evaluation

At the millimetre scale of the prototype conduits, it is hypothesised that surface tension was sufficient to maintain a stable water meniscus at the siphon apex, keeping the siphon active. For the siphon to reset, air would need to enter at the submerged lower opening of the pipe. It is reasoned that the diameter of this opening acted as the bottleneck. Under continuous inflow, the resulting flow velocity and hydrostatic conditions were sufficient to prevent air from penetrating the meniscus there, rendering the device non-functional for the intended application. Once the inflow ceased, the balance shifted, allowing air to enter, and the siphon deactivated as intended.

This limitation was strengthened by the anisotropic, layer-wise structure of FDM 3D printing, which introduced surface roughness and promoted water retention along layer interfaces. An attempt was made to mitigate this by applying silicone spray to render the plastic water-repellent, though without measurable success. Minor seepage at layer interfaces was also observed. Post-processing treatments, such as solvent smoothing or epoxy coating, could address these issues, though they add complexity and reduce the rapid-prototyping advantage of the fabrication method.

Together, these represent fundamental scaling and fabrication constraints that were overlooked in the initial design, in which capillary effects were neglected relative to hydrostatic pressure. The device consequently functioned correctly only under intermittent flow conditions, where sufficient time elapsed between discharge events for complete drainage and air re-entry. This precluded its use in the experimental portions of this thesis, which required continuous measurement capability. Successful operation would require either geometric upscaling to reduce capillary dominance or the active incorporation of air-admittance mechanisms to ensure reliable siphon breaking.

## 7.3. Future Development

The siphon flow meter concept offers theoretical advantages in cumulative discharge measurement, particularly in terms of calibration independence and reduced error accumulation. The viability of FDM-printed devices for field hydrological sensing has been demonstrated Kubát et al. (2025), suggesting that the fabrication approach itself is not the fundamental barrier. However, the present prototype reveals that geometric scaling and material selection introduced critical constraints that prevented operational deployment.

Future development should prioritise:

1. **Air-admittance integration**: The main focus of further development should be ensuring that air can reach the siphon apex to ensure siphon termination, despite surface tension effects. This could be done through geometric scaling. By increasing characteristic dimensions to ensure gravitational forces dominate capillary effects, enabling reliable siphon breaking. A larger inside area of the tube would decrease the accuracy. Alternatively, choosing a smoother material would limit surface friction and could allow the siphon to deactivate. Incorporating explicit air valves or vents could also be explored.
2. **Material selection**: Transitioning to more durable polymers such as PETG or nylon would improve UV and hydrolytic resistance, extending the device's suitability for long-term field deployments. A smoother internal surface at the siphon apex could also improve air entry, as noted in recommendation 1, and could be achieved through resin printing or stainless steel machining. Resin printing is more cost-effective, while steel provides superior durability. However, both present sustainability drawbacks: resin involves toxic compounds, and steel production is resource-intensive. This contrasts with the current PLA-based approach, which benefits from being bio-based and recyclable, and should be weighed accordingly in any material transition decision.
3. **Surface treatment**: Despite already having tried coating the device with silicon spray, additional investigation of hydrophobic coatings or post-processing techniques to reduce surface energy and promote complete drainage is recommended.
4. **Connection**: The current device lightly leaks at the connection between the two parts. A screw connection, sealing tape, or printing the sensor in one piece could overcome this. Printing in one piece would require a larger printer than the one available in this study, and would likely face difficulties with unsupported bridges.

# 8

# Synthesis and discussion

The preceding chapters have individually examined distinct aspects of Live Pole Drain (LPD) hydrology through a series of controlled open-air laboratory experiments. Taken together, these contributions are synthesised here in relation to the overarching research objective: to develop an evidence-based conceptual model of the hydrological behaviour of Live Pole Drains through experimental investigation. Building on the four perceptual models (PM1–PM4) defined in Chapter 2, this discussion evaluates the degree to which the experimental findings collectively support a translation from perceptual to conceptual representation of LPD hydrological processes, addressing sub-objectives 1 and 2. In doing so, the implications for LPD functioning in a slope-drainage context are considered (sub-objective 3), alongside reflections on the OAL approach as a methodology for NbS hydrological research (sub-objective 4) and the role of the developed siphonic flow meter in enabling future investigation (sub-objective 5).

## 8.1. From perceptual to conceptual

The point injection and distributed irrigation experiment indicated that LPD bundle flow is threshold-dependent, consistent with PM3. This threshold was partially reached during the irrigation experiment, when soil moisture increased downslope of the irrigated area, interpreted as evidence of bundle flow. This occurred as the distributed irrigation gradually saturated the surrounding soil, suggesting that soil moisture conditions around the bundle govern whether bundle flow is initiated. The point injection experiment, applied directly into the bundle, did not produce bundle flow, possibly because a local perched water table developed, limiting lateral exchange with the bundle. The infiltrometer experiment further revealed secondary behaviour consistent with PM4, demonstrating that LPD enhance the infiltration capacity of the surrounding soil. This was evidenced by higher upper-tail unsaturated hydraulic conductivity values on the LPD slope compared to a bare reference slope, attributed to root growth and associated biological activity.

Together, the alignment of experimental findings with PM3 and PM4 allows these perceptual models to be translated into a conceptual model of LPD hydrological behaviour: one in which drainage through the bundle is activated by a soil moisture threshold, while simultaneously the LPD progressively enhances infiltration capacity through root-driven increases in unsaturated hydraulic conductivity. By providing experimental evidence for this behaviour, this conceptual model contributes to the understanding of subsurface hydrological processes associated with LPD. However, to let these insights inform data-driven methods, the model would need to be developed further towards the more conventional definition of a conceptual model as a 'formalised structure with defined storages and transfer functions' (K. Beven, 2012). Benschop (2022) and Cahill (2024) have proposed such formalised models for LPD hydrology. The findings of this study primarily indicate that a threshold dependency should be incorporated into these models, and that the effectiveness of LPD is highly dependent on the soil composition of the surrounding slope. The influence of antecedent soil moisture conditions on LPD behaviour, whilst hypothesised as a key control, could not be systematically characterised from the experiments in this study. Only indicative evidence was found, suggesting that higher antecedent soil moisture leads to quicker percolation.

Existing design guidelines (Campbell et al., 2008; Pacas & Polster, 1999) do not mention the relevance of a low-permeability base layer or any threshold-dependent behaviour in LPD functioning. This can likely be attributed to that these guidelines are primarily oriented towards practical application rather than mechanistic understanding of LPD hydrology. Nevertheless, the threshold dependency identified in this study potentially carries implications for how LPD are applied. For instance, Goldsmith et al. (2014) describes a case study in which LPD were successfully applied in a sandy soil, combined with live fascines, quality topsoil, and an erosion control blanket, with this combination of bioengineering techniques halting and preventing further erosion. However, the findings of this study raise the question of whether the LPD specifically contributed to the effectiveness observed in that case, given that the sandy substrate may not have provided the low-permeability conditions suggested here as necessary for threshold-dependent bundle flow.

### 8.1.1. Numerical modelling of slope effects

The current experimental setup did not facilitate an empirical assessment of the effects of different slopes and soil composition on LPD hydrological behaviour. Therefore, a simplified numerical modelling approach is used to gain initial insight into these effects. MODFLOW, specifically MODFLOW-NWT solving the Newton-Raphson equation for unconfined flow, was used to set up this model, aligning with Kumar et al. (2021)'s synthesis, which states that MODFLOW is commonly used for 'evaluating the hydrological efficiency of green infrastructure'. The model setup used is presented in Appendix C.12. In this MODFLOW-NWT saturated flow model, flow partitioning is governed by contrasts in saturated hydraulic conductivity and head gradients. Unsaturated dynamics, such as coarser layers becoming less permeable as they desaturate, would further promote lateral diversion but are not captured in this model. A parameter sweep was performed across realistic hillslope angles [1, 5, 10, 15, 20, 30, 40]° and base layer hydraulic conductivities [10, 1, 0.5, 0.1, 0.05, 0.01, 0.005] m/d representing common soil types, with separate plots for interface layer conductivities of 5, 15, and 35 m/d. The resulting diversion ratios are presented in Figure 8.2.

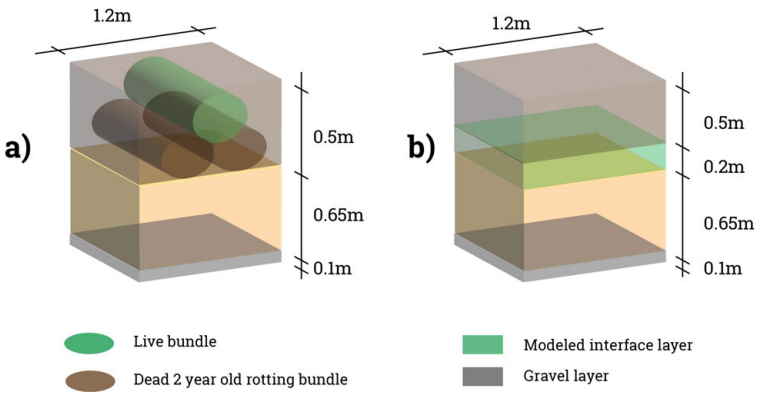



**Figure 8.1:** LPD representation a) in OAL and b) as an interface layer in the MODFLOW-NWT model.

The modelled behaviour is consistent with observations from the experimental evaluation, with no bundle flow occurring for a permeable base layer. The results indicate that the hydraulic conductivity of the base layer is the dominant control on LPD activation: a highly permeable base layer drains faster than it is recharged, maintaining a large infiltration potential and preventing lateral flow through the bundle. For lower base layer conductivities, the diversion ratio increases with slope angle, as the base layer cannot drain fast enough through the gravel layer and the increased gravity gradient promotes lateral flow towards the bundle drain. These results should be considered indicative, given the simplifying assumptions of homogeneous layer properties and the absence of three-dimensional effects.

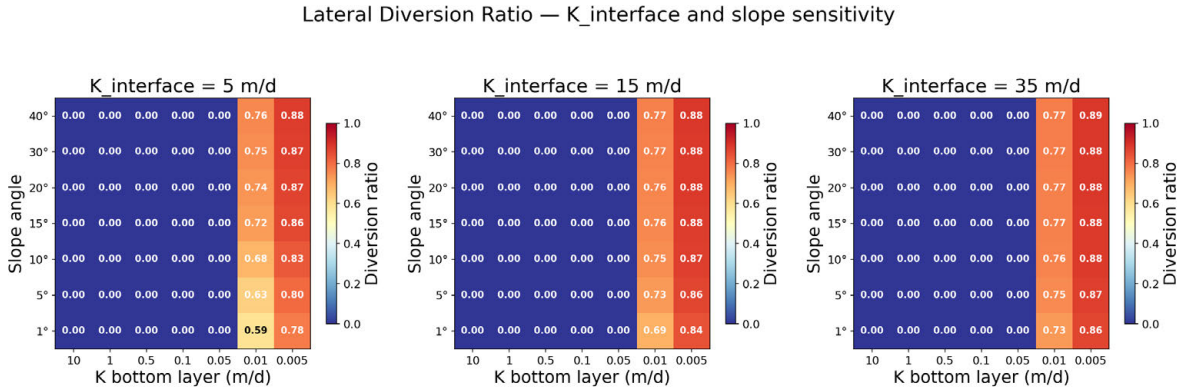



**Figure 8.2:** MODFLOW-NWT modelled diversion ratio sensitivity to slope angle and interface layer hydraulic conductivity [K] $K_{soil} = k_{upper}[m/d]$, recharge=300 mm/d over first 1 m, diversion ratio: 0 = all to sand, 1 = all through interface.

## 8.2. Implications for LPD as an NbS for slope stability

The threshold-dependent lateral drainage observed in this study is consistent with the hypothesised slope-stabilising function of LPD, though the effect was less pronounced than in the laboratory results of Berlitz et al. (2025), where continuous activation and significant discharge along the full length of the drain were observed. This difference is hydrologically logical: the highly permeable sand composition of the current setup facilitates vertical drainage, preventing lateral soil moisture accumulation required to reach the activation threshold. Analysis by Tromp-van Meerveld and McDonnell (2006) demonstrates that such thresholds are a widely observed feature of subsurface flow systems. The effectiveness of LPD as an NbS for slope stability is therefore intrinsically linked to whether these thresholds are met under the prevailing hydrological and topographical conditions. This contrasts with the broad applicability attributed to LPD by Campbell et al. (2008), who characterise them as especially versatile among soil bioengineering techniques (Figure C.1). While this versatility likely holds for their established roles in surface erosion control and landscape restoration, the hypothesis that LPD can additionally function as a shallow landslide mitigation measure remains conditional on the hydraulic properties of the surrounding soil, particularly the underlying layer.

Beyond lateral drainage, the higher median and upper-quantile hydraulic conductivity observed on the LPD slope in Experiment 3 suggests increased infiltration capacity relative to the bare slope. However, the suction-based measurements used in this study capture unsaturated conductivity under moderate conditions and do not directly quantify preferential flow under saturated conditions, a recognised limitation of tension infiltrometer approaches Allaire et al. (2009). As K. Beven and Germann (2013) show, macropore flow associated with root systems plays a dominant role in infiltration during high-intensity rainfall events, while Hortonian overland flow initiation is primarily governed by the lower-quantile hydraulic conductivity. The observed increase in upper-quantile conductivity on the LPD slope, therefore, most directly implies a stabilising effect during high-intensity events, though a reduction in overland flow generation would additionally require an increase in the lower quantile. However, the relationship between root systems and slope stability is not unconditional. The increased permeability associated with root systems, as demonstrated above, is consistent with the findings of Qin et al. (2022), who showed that this same permeability can, under certain conditions, contribute to shallow landslide triggering rather

than slope stabilisation. Pore-water pressure can build up at the ends of roots, where the preferential flow path terminates, coinciding with the zone of reduced mechanical reinforcement beyond the root zone. This suggests that LPD effectiveness depends on the depth of the permeable layer relative to the root zone depth, a critical consideration for shallow landslide-prevention applications.

## 8.3. The OAL methodology

The OAL methodology employed in this study was explicitly positioned between laboratory experimentation and experimental catchment research. The finding that LPD show limited activation above a highly permeable sand layer is itself a product of this controlled setting, and would have been considerably more difficult to isolate in a catchment study, where boundary and initial conditions cannot be fully specified, experiments are not repeatable, and complex process interactions are difficult to disentangle (Blöschl et al., 2016). At the same time, the OAL setting allowed biological processes to develop at realistic scales, as evidenced by the various mushroom species emerging on the LPD slope (Appendix D). The controlled conditions further reduced the risk of NbS failure during the critical initial establishment phase, which Mickovski et al. (2024) identify as a vulnerable period in field implementations where ground and environmental extremes can cause premature failure. The methodology thus fulfilled its intended role, confirming the value of OAL alongside both laboratory experimentation and experimental catchment research. The three approaches are complementary: laboratory studies offer maximum control, OAL isolate processes from confounding subsurface and topographic factors, and catchment studies demonstrate real-world effectiveness.

However, this study also demonstrated that the validity of OAL research depends on the quality of its implementation. The outer boundary proved permeable beyond non-destructive repair, and the limited measurement density (one drain and six soil moisture points) resulted in higher uncertainty than anticipated. Together, these constraints limited the conditions under which LPD could be observed, ultimately hindering insights into fully activated and effective LPD behaviour. The practical limitations observed in this study, particularly the leakage and soil settling, risk undermining confidence in the approach among policymakers and practitioners, independent of the scientific results obtained. This points to the importance of robust implementation, rather than to a limitation of the OAL approach itself.

## 8.4. Siphonic flow-meter

The siphonic flow meter developed in this study represents a promising methodological contribution to low-cost hydrological instrumentation. Low-cost, precise flow meters are widely useful in hydrological research, where instrumentation costs can otherwise limit the spatial density of measurements. Leveraging the accessibility of FDM 3D printing, the siphonic flow meter has clear potential in this regard. The device functions correctly across a single activation cycle, but does not yet operate reliably across consecutive cycles. The primary bottleneck is its inability to deactivate under continuous inflow conditions, and further development is required before deployment.

## 8.5. Recommendations

### 8.5.1. Current setup

As this study is based on a single experimental run, repeating the experiment is recommended to validate the findings. Tracer tests, for instance using soluble tracer pods combined with an auto-sampler, would be a valuable addition, as they could provide more direct evidence of flow pathways and velocities. Endoscopic inspection of the bundle interior could provide direct insight into root growth and channel formation that hydrological measurements alone cannot reveal. While this study focused on the subsurface stabilising mechanisms of LPD, the setup could also serve as a useful proof of concept for their surface erosion prevention capacity, which similarly lacks robust experimental evidence. Overland flow or flooding experiments, along with excavation of the bundles, are necessarily destructive and should therefore be reserved for the end of the project.

The density of soil moisture sensors could be increased, particularly alongside the bundles. This study suggests that the bundle activation threshold is influenced by lateral soil moisture distribution, a factor that the current sensor layout cannot fully capture. Adding pore water pressure and suction sensors could strengthen the interpretability of results, as stress conditions in the unsaturated zone play an important role in slope instability (Godt et al., 2009) and suction is a valuable complement to soil moisture monitoring in characterising hydrological slope behaviour (Bordoni et al., 2015).

The development of the siphonic flow meter shows promise. Together with the low-cost 3D-printed infiltrometer presented by Kubát et al. (2025), it demonstrates the viability of FDM 3D printing for hydrological instrumentation within the OAL framework. Should it not be fully developed in time for future experiments, the PVC flow meter remains a simple, low-cost alternative, though its design would benefit from better distributing hole sizes to match the expected flow range and from more extensive calibration to reduce the uncertainty observed in this study.

### 8.5.2. OAL design at FPH

The main benefit of OAL over experimental catchment research is that it excludes lateral subsurface flows and topography that could unknowingly influence NbS behaviour. The impermeable outer layer was designed to ensure this hydrological isolation, but the 65-80% water loss observed despite sealing perforations with glue, bitumen, and clay limited the interpretation of results. Future iterations could replace perforation-based drainage with an automatic pump triggered by a defined water-level threshold, which would also enable the controlled water-table experiments described by Cahill (2024).

The highly permeable sand layer in the current setup was deliberately chosen to facilitate interpretability, but the inclusion of a low-conductance base layer, such as a clayey horizon, represents a valuable direction for future research. Interflow and subsurface lateral flow, in the sense defined by McGuire et al. (2024), can only develop in the presence of such a layer. A setup that better replicates this natural condition could lower the activation threshold for lateral preferential flow and provide an opportunity to more convincingly demonstrate LPD effectiveness under the conditions in which they are intended to operate. Determining this activation threshold in a representative setting should therefore be an explicit objective of future research.

A frequent argument in favour of experimental catchment research, often referred to as Open-Air Laboratories, is that it fosters collaboration between stakeholders, citizens and the scientific community ('through the life cycle of the NbS') (Gallotti et al., 2021; Gonzalez-Ollauri et al., 2023; Kumar et al., 2020). Cahill (2024) reports the use of collaborative design principles in the design of the LPD OAL, yet during this study, stakeholders were not involved. While stakeholder engagement is more central to full experimental catchments than to smaller-scale OAL setups like the one used here, it would still be valuable to return to the stakeholders involved in the design.

### 8.5.3. LPD research

Following Weiler and McDonnell (2007), the logical next step would be to translate the findings into a physical model, moving towards more quantitative characterisations of lateral preferential flow through LPD. Such a model should explicitly incorporate the threshold behaviour observed in this study.

LPD would benefit from a broader base of successful case studies. Since this study found no evidence against their effectiveness, cautious implementation in low- to medium-risk situations, with the possible exception of highly permeable soils, could help build the practical evidence base needed for wider adoption. Adopting the ”let’s see if it works” mentality documented by Goldsmith et al. (2014) would support this kind of incremental, learning-oriented uptake.

An additional promising application is the use of LPD as a nature-based alternative to concrete French drains, a comparison already drawn by Pacas and Polster (1999). This would make them particularly suited to dissipating localised groundwater pressure. French drains have been shown to effectively reduce soil moisture both near and further from the drain and to redistribute water tables (Rahimi et al., 2024), though their exfiltration performance is similarly dependent on the permeability of the surrounding soil (An et al., 2022).

# References


Allaire, S. E., Roulier, S., & Cessna, A. J. (2009). Quantifying preferential flow in soils: A review of different techniques. *Journal of Hydrology*, *378*(1–2), 179–204. https://doi.org/10.1016/j.jhydrol.2009.08.013

An, J., Copeland, T., & Nam, B. H. (2022). Recycled Concrete Aggregate Drainage Effectiveness in a French Drainage System: A Full-Scale In Situ Study. *Journal of Testing and Evaluation*, *50*(6), 3094–3115. https://doi.org/10.1520/JTE20220144

Angulo-Jaramillo, R., Bagarello, V., Iovino, M., & Lassabatere, L. (2016). *2. The 2 cm Suction Choice: What It Means and How to Defend It*. Springer International Publishing. https://doi.org/10.1007/978-3-319-31788-5

Bagarello, V., Iovino, M., & Tusa, G. (2001). Effect of Contact Material on Tension Infiltrometer Measurements. *Transactions of the ASAE*, *44*(4), 911–916. https://doi.org/10.13031/2013.6256

Beersma, J., Hakvoort, H., Jilderda, R., Overeem, A., & Versteeg, R. (2019). *Neerslagstatistiek en - Reeksen voor het Waterbeheer 2019* (tech. rep. No. ISNBN 978.90.5773.860.9). STOWA. STOWA.

Benschop, E. (2022, August). *Hydrological Characterisation of a Live Pole Draine*.

Berlitz, F., Benschop, E., Mickovski, S. B., & Gonzalez-Ollauri, A. (2024). Testing the hydrological performance of live pole drains (LPD) for mitigation of slope instability. *Ecological Engineering*, *208*, 107360. https://doi.org/10.1016/j.ecoleng.2024.107360

Berlitz, F., Gonzalez Ollauri, A., Bogaard, T., & Mickovski, S. (2025, March 18). *Eco-hydrological characterisation of live pole drains (LPDs) for slope drainage and stability*. https://doi.org/10.5194/egusphere-egu25-6124

Beven, K. (2012). Down to basics: Runoff processes and the modelling process. In *Rainfall-runoff modelling* (pp. 1–23). John Wiley & Sons, Ltd. https://doi.org/https://doi.org/10.1002/9781119951001.ch1

Beven, K., & Germann, P. (1982). Macropores and water flow in soils. *Water Resources Research*, *18*(5), 1311–1325. https://doi.org/10.1029/WR018i005p01311

Beven, K., & Germann, P. (2013). Macropores and water flow in soils revisited: REVIEW. *Water Resources Research*, *49*(6), 3071–3092. https://doi.org/10.1002/wrcr.20156

Beven, K. J., & Chappell, N. A. (2021). Perceptual perplexity and parameter parsimony. *WIREs Water*, *8*(4), e1530. https://doi.org/10.1002/wat2.1530

Blöschl, G., Blaschke, A. P., Broer, M., Bucher, C., Carr, G., Chen, X., Eder, A., Exner-Kittridge, M., Farnleitner, A., Flores-Orozco, A., Haas, P., Hogan, P., Kazemi Amiri, A., Oismüller, M., Parajka, J., Silasari, R., Stadler, P., Strauss, P., Vreugdenhil, M., … Zessner, M. (2016). The Hydrological Open Air Laboratory (HOAL) in Petzenkirchen: A hypothesis-driven observatory. *Hydrology and Earth System Sciences*, *20*(1), 227–255. https://doi.org/10.5194/hess-20-227-2016

Blöschl, G., Bierkens, M. F., Chambel, A., Cudennec, C., Destouni, G., Fiori, A., Kirchner, J. W., McDonnell, J. J., Savenije, H. H., Sivapalan, M., Stumpp, C., Toth, E., Volpi, E., Carr, G., Lupton, C., Salinas, J., Széles, B., Viglione, A., Aksoy, H., … Zhang, Y. (2019). Twenty-three unsolved problems in hydrology (UPH) – a community perspective. *Hydrological Sciences Journal*, *64*(10), 1141–1158. https://doi.org/10.1080/02626667.2019.1620507

Boerlijst, H. (2025, June). *Hydrologisch gedrag van een Live Pole Drain*.

Bogaard, T. A., & Greco, R. (2016). Landslide hydrology: From hydrology to pore pressure. *WIREs Water*, *3*(3), 439–459. https://doi.org/10.1002/wat2.1126

Bordoni, M., Meisina, C., Valentino, R., Lu, N., Bittelli, M., & Chersich, S. (2015). Hydrological factors affecting rainfall-induced shallow landslides: From the field monitoring to a simplified slope stability analysis. *Engineering Geology*, *193*, 19–37. https://doi.org/10.1016/j.enggeo.2015.04.006

Bowyer, P., Alfieri, S. M., Basu, B., Cremin, E., Debele, S., Kumar, P., Lechner, V., Loupis, M., Menenti, M., Mickovski, S., Gonzalez-Ollauri, A., Pfeiffer, J., Pilla, F., Pulvirenti, B., Ruggieri, P., Basu, A. S., Spyrou, C., Unguendoli, S., Zieher, T., & Sabatino, S. D. (2024). Modelled effectiveness of NbS in reducing disaster risk: Evidence from the OPERANDUM project. *Nature-Based Solutions*, *5*, 100127. https://doi.org/10.1016/j.nbsj.2024.100127

Cahill, L. (2024, February). *Design, Construction and Modeling of an Experimental Setup for the long term Eco-hydrological behavior of a Live Pole Drain*.

Campbell, S. D. G., Shaw, R., Sewell, R. J., & Wong, J. C. F. (2008). Guidelines for Soil Bioengineering Applications on Natural Terrain Landslide Scars. (227).

Capobianco, V., Fraccica, A., Anselmucci, F., & Tagarelli, V. (2025). Nature- and bio-based solutions for ecosystem restoration, landslide hazard mitigation, and ground improvement: Research and application novelties. *Ecological Engineering*, *219*, 107710. https://doi.org/10.1016/j.ecoleng.2025.107710

Capobianco, V., Uzielli, M., Kalsnes, B., Choi, J. C., Strout, J. M., Von Der Tann, L., Steinholt, I. H., Solheim, A., Nadim, F., & Lacasse, S. (2022). Recent innovations in the LaRiMiT risk mitigation tool: Implementing a novel methodology for expert scoring and extending the database to include nature-based solutions. *Landslides*, *19*(7), 1563–1583. https://doi.org/10.1007/s10346-022-01855-1

Carter, M. R., & Gregorich, E. G. (Eds.). (2008). *Soil sampling and methods of analysis* (2nd ed). Canadian Society of Soil Science ; CRC Press.

Casey, F. X. M., & Derby, N. E. (2002). Improved design for an automated tension infiltrometer. *Soil Science Society of America Journal*, *66*(1), 64–67. https://doi.org/10.2136/sssaj2002.6400

Delft University of Technology. (2025). *Davis weather station data* (Version 1.0). Delft University of Technology. https://ruisdael-observatory.nl/

Di Prima, S., Lassabatere, L., Bagarello, V., Iovino, M., & Angulo-Jaramillo, R. (2016). Testing a new automated single ring infiltrometer for Beerkan infiltration experiments. *Geoderma*, *262*, 20–34. https://doi.org/10.1016/j.geoderma.2015.08.006

Dohnal, M., Dusek, J., & Vogel, T. (2010). Improving Hydraulic Conductivity Estimates from Minidisk Infiltrometer Measurements for Soils with Wide Pore-Size Distributions. *Soil Science Society of America Journal*, *74*(3), 804–811. https://doi.org/10.2136/sssaj2009.0099

Dunne, T., Zhang, W., & Aubry, B. F. (1991). Effects of Rainfall, Vegetation, and Microtopography on Infiltration and Runoff. *Water Resources Research*, *27*(9), 2271–2285. https://doi.org/10.1029/91WR01585

Gadi, V. K., Tang, Y.-R., Das, A., Monga, C., Garg, A., Berretta, C., & Sahoo, L. (2017). Spatial and temporal variation of hydraulic conductivity and vegetation growth in green infrastructures using infiltrometer and visual technique. *CATENA*, *155*, 20–29. https://doi.org/10.1016/j.catena.2017.02.024

Gallotti, G., Santo, M. A., Apostolidou, I., Alessandri, J., Armigliato, A., Basu, B., Debele, S., Domeneghetti, A., Gonzalez-Ollauri, A., Kumar, P., Mentzafou, A., Pilla, F., Pulvirenti, B., Ruggieri, P., Sahani, J., Salmivaara, A., Basu, A. S., Spyrou, C., Pinardi, N., … Di Sabatino, S. (2021). On the Management of Nature-Based Solutions in Open-Air Laboratories: New Insights and Future Perspectives. *Resources*, *10*(4), 36. https://doi.org/10.3390/resources10040036

Ghestem, M., Sidle, R. C., & Stokes, A. (2011). The Influence of Plant Root Systems on Subsurface Flow: Implications for Slope Stability. *BioScience*, *61*(11), 869–879. https://doi.org/10.1525/bio.2011.61.11.6

Godt, J. W., Baum, R. L., & Lu, N. (2009). Landsliding in partially saturated materials. *Geophysical Research Letters*, *36*(2), 2008GL035996. https://doi.org/10.1029/2008GL035996

Goldsmith, W., Gray, D., & McCullah, J. (2014). *Bioengineering Case Studies: Sustainable Stream Bank and Slope Stabilization*. Springer New York. https://doi.org/10.1007/978-1-4614-7996-3

Gonzalez-Ollauri, A., & Mickovski, S. B. (2017). Hydrological effect of vegetation against rainfall-induced landslides. *Journal of Hydrology*, *549*, 374–387. https://doi.org/10.1016/j.jhydrol.2017.04.014

Gonzalez-Ollauri, A., Mickovski, S. B., Anderson, C. C., Debele, S., Emmanuel, R., Kumar, P., Loupis, M., Ommer, J., Pfeiffer, J., Panga, D., Pilla, F., Sannigrahi, S., Toth, E., Ukonmaanaho, L., & Zieher, T. (2023). A nature-based solution selection framework: Criteria and processes for addressing hydro-meteorological hazards at open-air laboratories across Europe. *Journal of Environmental Management*, *331*, 117183. https://doi.org/10.1016/j.jenvman.2022.117183

González-Ollauri, A., & Mickovski, S. B. (2014). Integrated Model for the Hydro-Mechanical Effects of Vegetation Against Shallow Landslides. *EQA - International Journal of Environmental Quality*, 37–61 Pages. https://doi.org/10.6092/ISSN.2281-4485/4535

Hendrickx, J. M. H., & Flury, M. (2001, January). Uniform and Preferential Flow Mechanisms in the Vadose Zone. National Academy Press, National Research Council.

Jarvis, N., Koestel, J., & Larsbo, M. (2016). Understanding Preferential Flow in the Vadose Zone: Recent Advances and Future Prospects. *Vadose Zone Journal*, *15*(12), 1–11. https://doi.org/10.2136/vzj2016.09.0075

K. R. Close, G. Frasier, G. H. Dunn, & J. C. Loftis. (1998). TENSION INFILTROMETER CONTACT INTERFACE EVALUATION BY USE OF A POTASSIUM IODIDE TRACER. *Transactions of the ASAE*, *41*(4), 995–1004. https://doi.org/10.13031/2013.17272

Konikow, L. F., & Bredehoeft, J. D. (1992). Ground-water models cannot be validated. *Advances in Water Resources*, *15*(1), 75–83. https://doi.org/10.1016/0309-1708(92)90033-X

Kubát, J.-F., Zanna, F., Mildner, M., & Sněhota, M. (2025). Low-Cost Autonomous 3D-Printed Mini Disk Infiltrometer. *Journal of Hydrology*, *663*, 134212. https://doi.org/10.1016/j.jhydrol.2025.134212

Kumar, P., Debele, S. E., Sahani, J., Aragão, L., Barisani, F., Basu, B., Bucchignani, E., Charizopoulos, N., Di Sabatino, S., Domeneghetti, A., Edo, A. S., Finér, L., Gallotti, G., Juch, S., Leo, L. S., Loupis, M., Mickovski, S. B., Panga, D., Pavlova, I., … Zieher, T. (2020). Towards an operationalisation of nature-based solutions for natural hazards. *Science of The Total Environment*, *731*, 138855. https://doi.org/10.1016/j.scitotenv.2020.138855

Kumar, P., Debele, S. E., Sahani, J., Rawat, N., Marti-Cardona, B., Alfieri, S. M., Basu, B., Basu, A. S., Bowyer, P., Charizopoulos, N., Gallotti, G., Jaakko, J., Leo, L. S., Loupis, M., Menenti, M., Mickovski, S. B., Mun, S.-J., Gonzalez-Ollauri, A., Pfeiffer, J., … Zieher, T. (2021). Nature-based solutions efficiency evaluation against natural hazards: Modelling methods, advantages and limitations. *Science of The Total Environment*, *784*, 147058. https://doi.org/10.1016/j.scitotenv.2021.147058

Lanzafame, R., van Woudenberg, T., & Verhagen, S. (2024). *Modelling, uncertainty and data for engineers (mude) textbook* [Licensed under CC BY 4.0]. Retrieved January 2026, from https://mude.citg.tudelft.nl/book

Mafian, S., Huat, B. B. K., Barker, D. H., Rahman, N. A., & Singh, H. (2009). Live Poles for Slope Stabilization in the Tropical Environment.

McGuire, K. J., Klaus, J., & Jackson, C. R. (2024). JAMES BUTTLE REVIEW: Interflow, subsurface stormflow and throughflow: A synthesis of field work and modelling. *Hydrological Processes*, *38*(9), e15263. https://doi.org/10.1002/hyp.15263

METER Group. (2021, November). *MINI DISK INFILTROMETER*. Pullman, WA, USA. https://publications.metergroup.com/Manuals/20421_Mini_Disk_Manual_Web.pdf

Mickovski, S., Gonzalez-Ollauri, A., Sorolla, A., Löchner, A., & Emmanuel, R. (2024). A case history of co-design and co-deployment of a nature-based solution (NbS) against erosion and slope instability. *Ecological Engineering*, *209*, 107406. https://doi.org/10.1016/j.ecoleng.2024.107406

Minasny, B., & McBratney, A. B. (2000). Estimation of sorptivity from disc-permeameter measurements. *Geoderma*, *95*(3–4), 305–324. https://doi.org/10.1016/S0016-7061(99)00096-8

Nieber, J. L., & Sidle, R. C. (2010). How do disconnected macropores in sloping soils facilitate preferential flow? *Hydrological Processes*, *24*(12), 1582–1594. https://doi.org/10.1002/hyp.7633

Nimmo, J. R. (2021). The processes of preferential flow in the unsaturated zone. *Soil Science Society of America Journal*, *85*(1), 1–27. https://doi.org/10.1002/saj2.20143

Niswonger, R. G., Panday, S., & Ibaraki, M. (2011). *MODFLOW-NWT, a Newton formulation for MODFLOW-2005* (Report No. 6-A37). https://doi.org/10.3133/tm6A37

Norris, J. E., Stokes, A., Mickovski, S. B., Cammeraat, E., Van Beek, R., Nicoll, B. C., & Achim, A. (Eds.). (2008). *Slope Stability and Erosion Control: Ecotechnological Solutions*. Springer Netherlands. https://doi.org/10.1007/978-1-4020-6676-4

Pacas, C., & Polster, D. F. (1999). Restoration of the Vermilion Wetlands. *Roads Rails and Environment 4*, 28.

Pfister, L., & Kirchner, J. W. (2017). Debates—Hypothesis testing in hydrology: Theory and practice. *Water Resources Research*, *53*(3), 1792–1798. https://doi.org/10.1002/2016WR020116

Polster, D. F., & Bio, R. P. (1997). Restoration of Landslides and Unstable Slopes: Considerations for Bioengineering in Interior Locations.

Qin, M., Cui, P., Jiang, Y., Guo, J., Zhang, G., & Ramzan, M. (2022). Occurrence of shallow landslides triggered by increased hydraulic conductivity due to tree roots. *Landslides*, *19*(11), 2593–2604. https://doi.org/10.1007/s10346-022-01921-8

Rahimi, A., Liaghat, A., Ebrahimian, H., & Ashrafi, A. (2024). Performance of surface, subsurface and trench-type drainage systems in paddy fields for non-rice farming. *Irrigation and Drainage*, *73*(4), 1437–1452. https://doi.org/10.1002/ird.2971

Seddon, N., Chausson, A., Berry, P., Girardin, C. A. J., Smith, A., & Turner, B. (2020). Understanding the value and limits of nature-based solutions to climate change and other global challenges. *Philosophical Transactions of the Royal Society B: Biological Sciences*, *375*(1794), 20190120. https://doi.org/10.1098/rstb.2019.0120

Sidle, R. C., & Bogaard, T. A. (2016). Dynamic earth system and ecological controls of rainfall-initiated landslides. *Earth-Science Reviews*, *159*, 275–291. https://doi.org/10.1016/j.earscirev.2016.05.013

Sidle, R. C., & Saito, H. (2024). The elusive link between soil physics and catchment hydrology. *Hydrological Processes*, *38*(6), e15200. https://doi.org/10.1002/hyp.15200

Stokes, A., Atger, C., Bengough, A. G., Fourcaud, T., & Sidle, R. C. (2009). Desirable plant root traits for protecting natural and engineered slopes against landslides. *Plant and Soil*, *324*(1–2), 1–30. https://doi.org/10.1007/s11104-009-0159-y

Stokes, A., Douglas, G. B., Fourcaud, T., Giadrossich, F., Gillies, C., Hubble, T., Kim, J. H., Loades, K. W., Mao, Z., McIvor, I. R., Mickovski, S. B., Mitchell, S., Osman, N., Phillips, C., Poesen, J., Polster, D., Preti, F., Raymond, P., Rey, F., … Walker, L. R. (2014). Ecological mitigation of hillslope instability: Ten key issues facing researchers and practitioners. *Plant and Soil*, *377*(1–2), 1–23. https://doi.org/10.1007/s11104-014-2044-6

Tani, M., Matsushi, Y., Sayama, T., Sidle, R. C., & Kojima, N. (2020). Characterization of vertical unsaturated flow reveals why storm runoff responses can be simulated by simple runoff-storage relationship models. *Journal of Hydrology*, *588*, 124982. https://doi.org/10.1016/j.jhydrol.2020.124982

Tromp-van Meerveld, H. J., & McDonnell, J. J. (2006). Threshold relations in subsurface stormflow: 1. A 147-storm analysis of the Panola hillslope. *Water Resources Research*, *42*(2), 2004WR003778. https://doi.org/10.1029/2004WR003778

Uchida, T., Tromp-van Meerveld, I., & McDonnell, J. J. (2005). The role of lateral pipe flow in hillslope runoff response: An intercomparison of non-linear hillslope response. *Journal of Hydrology*, *311*(1–4), 117–133. https://doi.org/10.1016/j.jhydrol.2005.01.012

Van Genuchten, M. Th. (1980). A Closed-form Equation for Predicting the Hydraulic Conductivity of Unsaturated Soils. *Soil Science Society of America Journal*, *44*(5), 892–898. https://doi.org/10.2136/sssaj1980.03615995004400050002x

Watson, K. W., & Luxmoore, R. J. (1986). Estimating Macroporosity in a Forest Watershed by use of a Tension Infiltrometer. *Soil Science Society of America Journal*, *50*(3), 578–582. https://doi.org/10.2136/sssaj1986.03615995005000030007x

Weiler, M., & McDonnell, J. J. (2007). Conceptualizing lateral preferential flow and flow networks and simulating the effects on gauged and ungauged hillslopes. *Water Resources Research*, *43*(3), 2006WR004867. https://doi.org/10.1029/2006WR004867

Zhang, R. (1997). Determination of Soil Sorptivity and Hydraulic Conductivity from the Disk Infiltrometer. *Soil Science Society of America Journal*, *61*(4), 1024–1030. https://doi.org/10.2136/sssaj1997.03615995006100040005x

# A

# Lab protocols

## A.1. Calibration of Soil Moisture Sensors

Materials:

- Desiccation chamber
- Soil drying containers
- Soil Moisture Sensors + data logger
- Large scale (resolution 0.1 g or better up to 10kg)
- Soil sampler with known volume
- Drying oven
- 2mm sieve + mortal
- 4 litres of soil sample
- Calibration bucket
- ruler

The protocol by Cahill (2024) serves as a basis, which in turn is based on the METER video tutorial: https://www.youtube.com/watch?v=eq_2VhcXxfI. **Note**: Calibration was conducted using oven-dried and rewetted soil rather than naturally air-dried samples, which may slightly alter dielectric properties. Given the highly sandy texture of the soil, this is not expected to meaningfully affect the results.

Method:

1. Collect a representative soil sample, around 4 litres.
2. Air dry sample in large tray
3. Remove rocks and other large objects and grind the soil
4. Sieve soil through a 2 mm sieve
5. Measure the weight of the clean dry calibration bucket
6. Layer soil in a bucket to achieve a similar bulk density to the in-situ soil, compacting it slightly every layer.
7. Reserve a sample of soil and weigh tin and soil+tin.
8. Oven dry sample again and weigh to determine water content.
9. Weigh the entire calibration bucket with soil before inserting the sensor.
10. Take a height measurement from the lid down to the base of the soil to maintain the same bulk density. (volume change correction)
11. Insert soil moisture sensor, fully covered in soil and take a RAW reading.

12. Repeat inserting and taking a reading a few times to ensure consistent insertion quality.
13. Remove soil from bucket, add 5 ml of water per 100 ml of (sandy) soil and mix well
14. Repeat steps 5 to 8 times to create calibration points. Maintain bulk density by packing the soil until the same height from the lid down to the base of the soil.
15. Oven dry reserved samples at 105 $^{\circ}C$ for 24 hours to determine water content.
16. Use spreadsheet at meter.ly/soil-specific-calibration to record data

Below, the calibration sheets for METER ECH2O 5TM and 5 TE are added for the sandy soil underneath the bundle. (small bits of planting soil were deliberately left in the sample, as root growth and general soil/water dynamics are hypothesised to lightly mix the soil layers.)

For the soil + container weights the cumulative weight of extracted soil is added. (between 1 & 2 35.4 is taken out, between 2 & 3 12.82 g is taken out, between 3 & 4 12.36 g is taken out, between 4 & 5 5.57 g is taken out, and between 5 & 6 27.61 g is taken out.

| | |
|---|---|
| **Soil ID:** | Slope1 upper side, top 30cm of soil |
| **Soil Volume ($cm^3$)** | 4900 |
| **Container Weight (g)** | 147.0 |
| **Dry Soil Weight (g)** | 6943.2 |
| **Bulk Density ($g\,cm^{-3}$)** | 1.42 |
| **Sensor Model** | ECH2O 5TE |

| Soil + Container Weights | | wet wt | water wt | *w* | θ | Sensor Measurements | |
|---|---|---|---|---|---|---|---|
| | | | | | | Sensor 1 | Sensor 2 |
| **Points** | **g** | **g** | **g** | **g g-1** | **$m^3\,m^{-3}$** | **RAW** | **RAW** |
| **Air dry** | 7103 | 6956.0 | 12.77 | 0.0018 | 0.0026 | 2.84 | 2.98 |
| **Point 2** | 7330.4 | 7183.4 | 240.17 | 0.0346 | 0.0490 | 4.48 | 4.44 |
| **Point 3** | 7550.22 | 7403.2 | 459.99 | 0.0663 | 0.0939 | 6.92 | 6.92 |
| **Point 4** | 7776.58 | 7629.6 | 686.35 | 0.0989 | 0.1401 | 8.56 | 8.66 |
| **Point 5** | 8004.15 | 7857.2 | 913.92 | 0.1316 | 0.1865 | 10.8 | 10.76 |

| Gravimetric Water Content Calculations of Air Dry Sample | | |
|---|---|---|
| | **Values** | **Units** |
| **Wet Soil + Tin** | 127.71 | g |
| **Dry Soil + Tin** | 127.48 | g |
| **Tin Weight** | 2.21 | g |
| **Gravimetric WC, *w*** | 0.001836034 | $g\,g^{-1}$ |

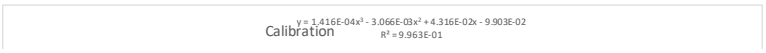



**Figure A.1:** METER calibration sheet ECH2O 5TE sensor for sand layer underneath bundle.

| | |
|---|---|
| **Soil ID:** | Slope1 upper side, top 30cm of soil |
| **Soil Volume ($cm^3$)** | 4900 |
| **Container Weight (g)** | 147.0 |
| **Dry Soil Weight (g)** | 6943.2 |
| **Bulk Density ($g\,cm^{-3}$)** | 1.42 |
| **Sensor Model** | ECH2O 5TM |

| Soil + Container Weights | | wet wt | water wt | *w* | θ | Sensor Measurements | |
|---|---|---|---|---|---|---|---|
| | | | | | | Sensor 1 | Sensor 2 |
| **Points** | **g** | **g** | **g** | **g g-1** | **$m^3\,m^{-3}$** | **RAW** | **RAW** |
| **Air dry** | 7103 | 6956.0 | 12.77 | 0.0018 | 0.0026 | 2.8 | 3.14 |
| **Point 2** | 7330.4 | 7183.4 | 240.17 | 0.0346 | 0.0490 | 4.64 | 4.4 |
| **Point 3** | 7550.22 | 7403.2 | 459.99 | 0.0663 | 0.0939 | 7.42 | 7.34 |
| **Point 4** | 7776.58 | 7629.6 | 686.35 | 0.0989 | 0.1401 | 9.2 | 9.36 |
| **Point 5** | 8004.15 | 7857.2 | 913.92 | 0.1316 | 0.1865 | 11.74 | 11.9 |

| Gravimetric Water Content Calculations of Air Dry Sample | | |
|---|---|---|
| | **Values** | **Units** |
| **Wet Soil + Tin** | 127.71 | g |
| **Dry Soil + Tin** | 127.48 | g |
| **Tin Weight** | 2.21 | g |
| **Gravimetric WC, *w*** | 0.001836034 | $g\,g^{-1}$ |

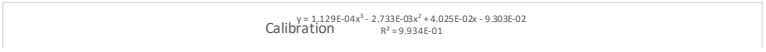



**Figure A.2:** METER calibration sheet ECH2O 5TM sensor for sand layer underneath bundle.

## A.2. Calibration PVC flow-meter

### A.2.1. Preparing PVC tubing

Materials:

- 40 mm & 50 mm ⌀ perforated PVC tube
- 40 mm & 50 mm ⌀ cap
- Drill with 1 mm, 2 mm, 3 mm, 4 mm, 5 mm, 6 mm, 8 mm drill bits
- Vaseline
- Ruler
- Silicon caulk + caulking gun
- Heat gun

Method:

1. Apply a silicone sealant to the joint between the PVC body and the cap to ensure a watertight seal.
2. Drill the holes according to the specifications shown in Figure A.3.
3. Ensure that no burrs, threads, or surface irregularities remain around the openings, as these may affect flow after calibration. Smooth the edges using a fine file.

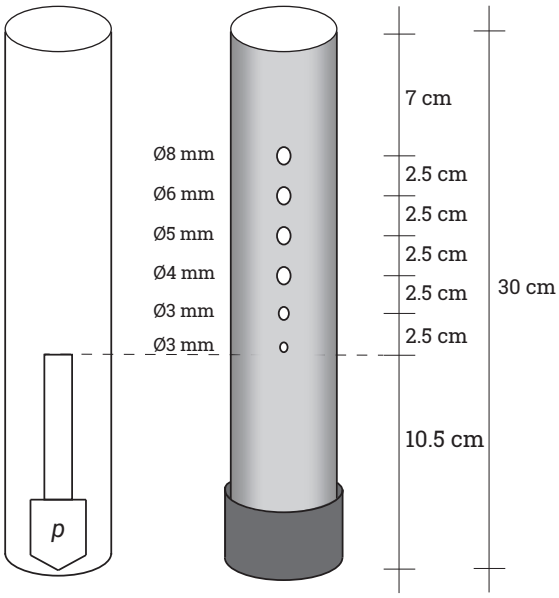



**Figure A.3:** Design dimensions PVC flow-meter

### A.2.2. Calibrating flow-meter

Materials:

- 10 l bucket
- 40 mm & 50 mm ∅ perforated PVC tube
- Scale up to 10 kg (≥1 g accuracy)
- Pump/tap with constant low flux
- Stopwatch
- Water pressure sensor
- Measuring glass

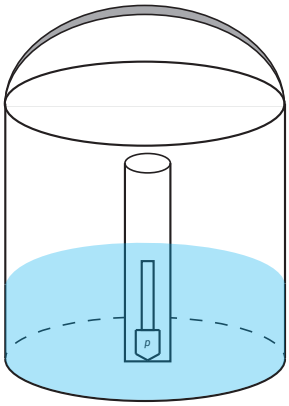


**Figure A.4:** PVC flow-meter in a control bucket

Method:

1. Weigh the empty bucket + flow-meter.
2. Establish flow of 1 l/min with tap/pump, measuring glass, and stopwatch.
3. Place a water pressure sensor in the tube and start logging with an interval of 15 s.
4. Place the flux into the bucket + PVC tube and wait until it reaches equilibrium; note the time and the weight of the control bucket + flow meter + water.
5. After 30 s note weight of the control bucket + flow-meter + water again.
6. Repeat steps 2 to 4 with flows of 2 l/min, 3 l/min up to 12 l/min.
7. Gather data from the pressure sensor and link water pressure equilibria to input flow.
8. Check flow through tap with weight measurements.

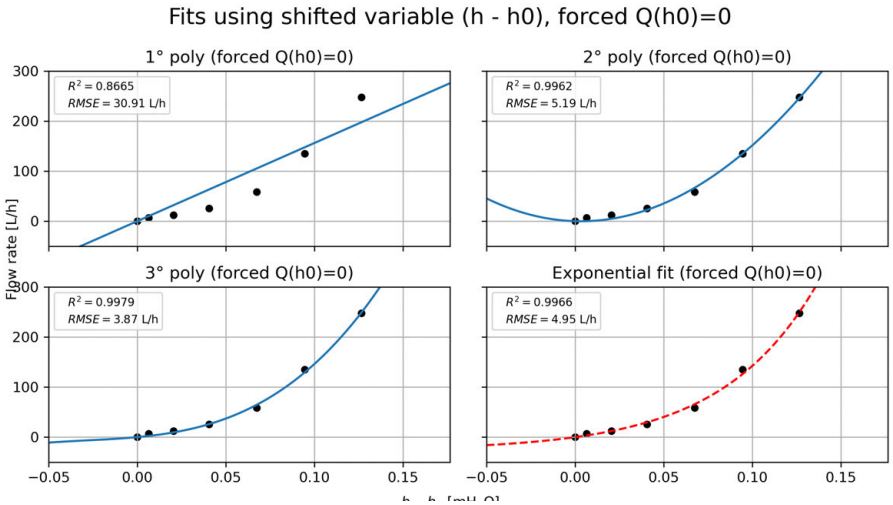



**Figure A.5:** Calibration PVC flow meter polynomial fits




**Figure A.6:** Calibration PVC flow meter for high flows using the tap.

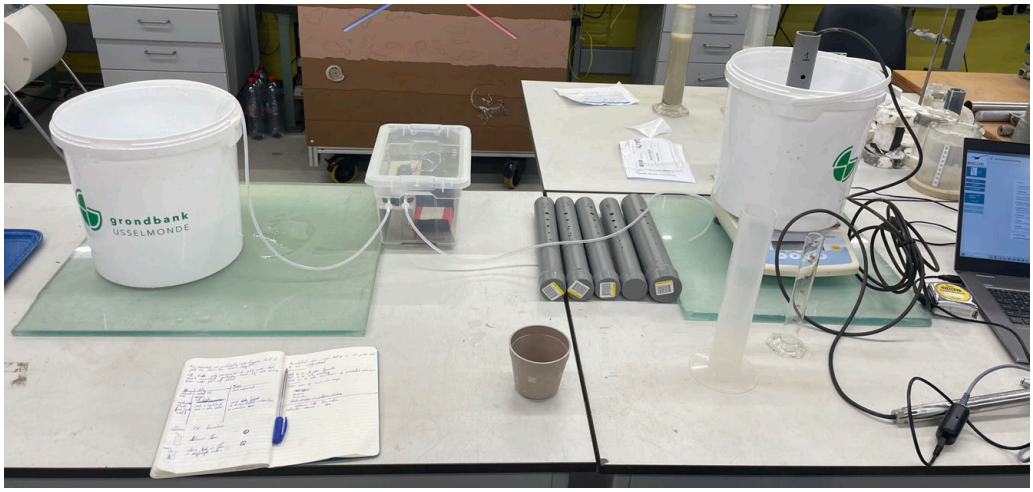



**Figure A.7:** Calibration PVC flow meter for low-flows using a peristaltic pump.

## A.3. Mini disk infiltrometer

Materials:

- METER Mini disk infiltrometer with a 2.25 cm disk radius
- Stopwatch
- Tap water
- Logging sheet

The protocol for taking mini disk infiltrometer measurements was adapted from METER Group (2021). The default suction rate of 2 cm was chosen as a balance between limiting the effects of inhomogeneous infiltration due to measuring at a slope and focusing on matrix flow over macropore flow (Angulo-Jaramillo et al., 2016). A measurement grid needs to be defined before starting the experiments.

1. Flush the stainless steel disk with water
2. Fill the Mariotte chamber with water
3. Fill the reservoir with tap water
4. Install the air inlet pipe into the Mariotte chamber at 2 cm suction.
5. Level the soil at measurement location and fill hollows with sieved soil (Angulo-Jaramillo et al., 2016)
6. Note start water level
7. Log water level every minute
8. Repeat step 5-7 for the predefined measurement grid, refilling the reservoir every other repetition

# B

# Flow-meter

## B.1. Calibrating PVC flow-meter

The PVC flow-meters were calibrated according to the protocol in Appendix A for 6 different flow rates (L/h): 3.15, 6.81, 12.15, 25.80, 58.29, 135.16, 247.59. Standard polynomial and exponential fits were fitted through this data, shown in Figure B.1. As the domain of PVC2 in experiments was smaller than the calibration domain, the fit metric is calculated and evaluated on the actual used domain in Figure B.1.

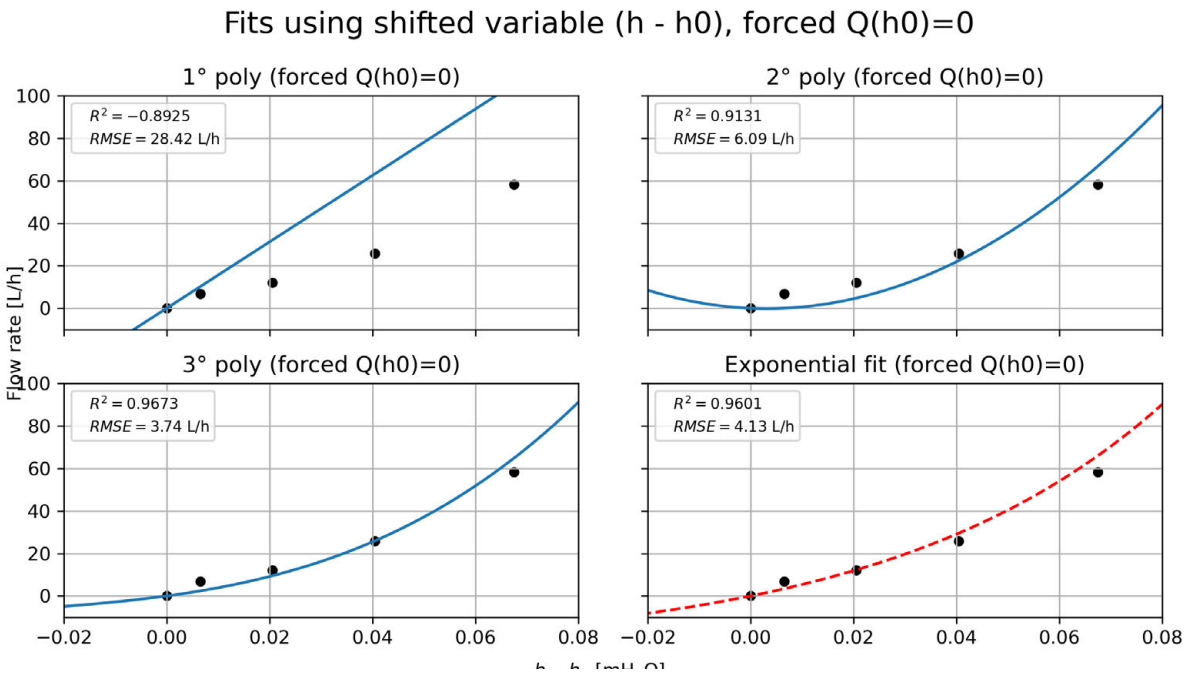
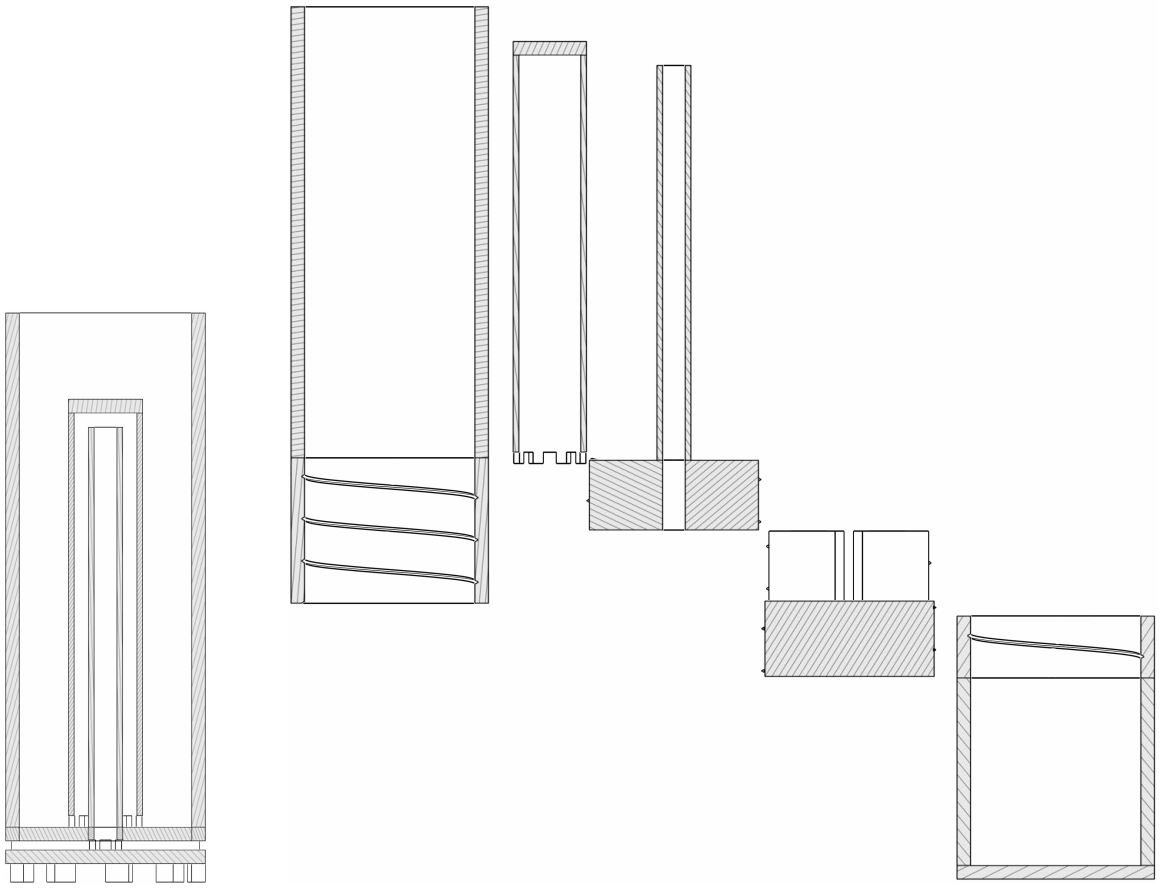



**Figure B.1:** Calibration PVC flow meter polynomial fits

## B.2. Development siphon flow-meter



**(a)** Version 1 **(b)** version 2

**Figure B.2:** Design process of a 3D printed Pythagoras cup–inspired flow meter. Not to scale.

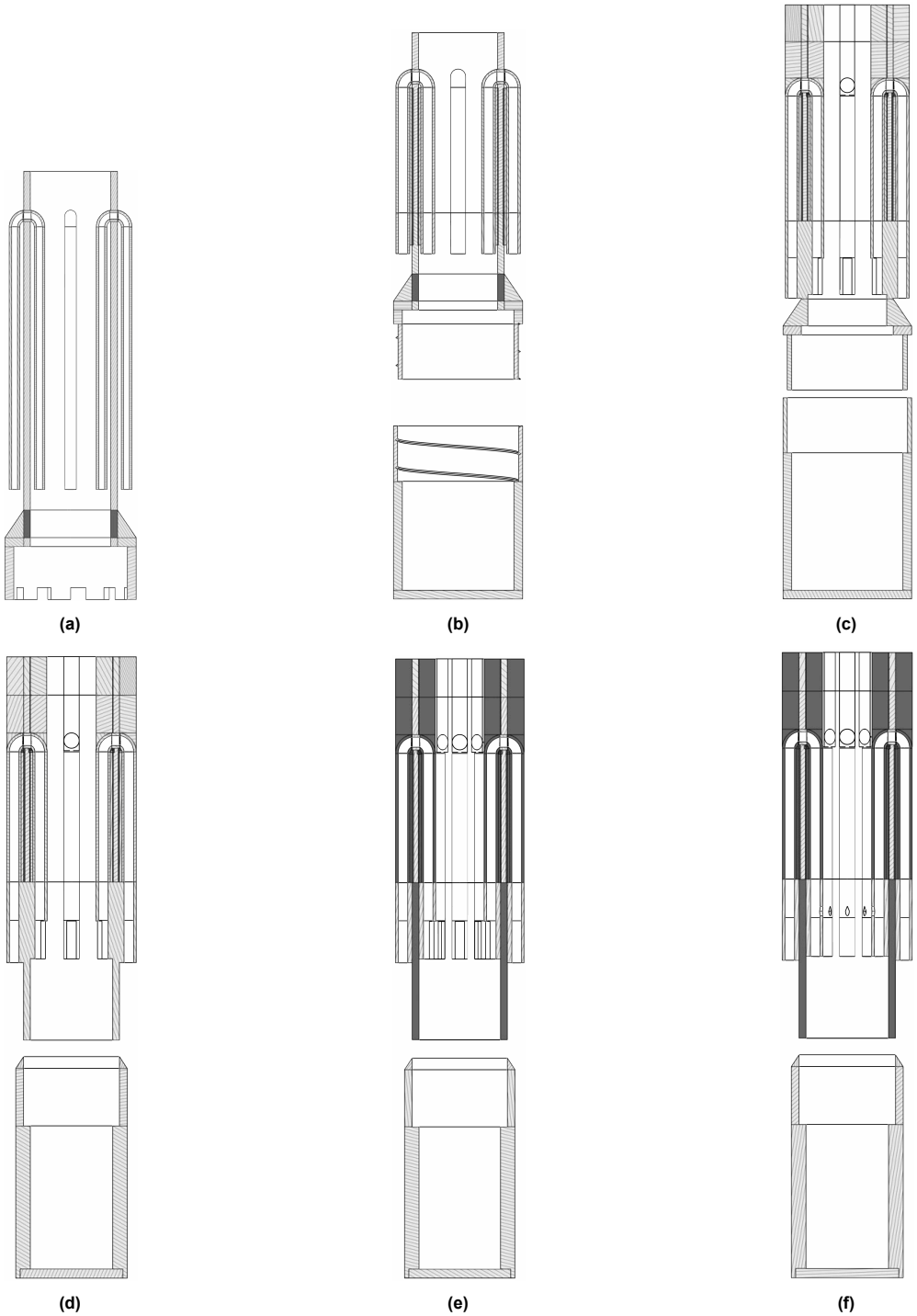



**Figure B.3:** Design iterations of the 3D printed siphonic flow meter. Not to scale.

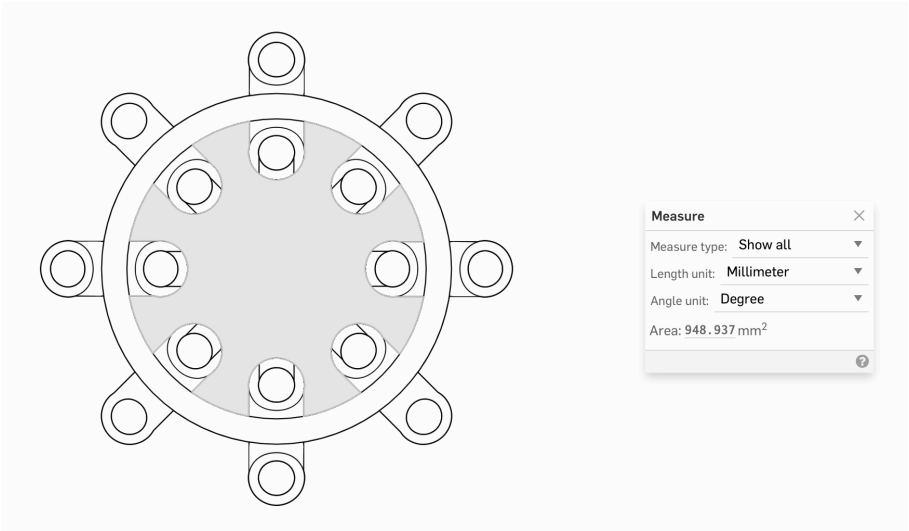



**Figure B.4:** Inside area siphonic flow meter

# C

# Additional data analyses

## C.1. LPD in applicability from bioengineering guide (Campbell et al., 2008)

Campbell et al. (2008)'s guide to bioengineering solutions presents a multitude of bioengineering solutions for slope stability. As shown in Figure C.1, LPD are applicable in widely varying site and soil conditions, more so than alternative solutions.

| Factor or Failure Process | Intensity or Type of Condition | Soil Bioengineering Measure | | | | | | | | | |
|---|---|---|---|---|---|---|---|---|---|---|---|
| | | Live Stakes | Live Fascines/ Pole Drains | Bender Fences | Live Gully Repair | Brush-layers | Hedge-layers | Branch-packing | Live Crib-walls | Joint Plant-ing | Veg Gabions |
| Slope Gradient | Steep | | • | | • | | | • | • | | • |
| | Moderate | • | • | • | • | • | • | • | • | • | • |
| | Gentle | • | • | • | n/a | n/a | n/a | n/a | • | • | • |
| Slope Height | High | • | • | | • | • | • | | | | |
| | Low | • | • | • | | • | • | • | • | • | • |
| Soil Depth | Deep | • | • | | • | • | • | • | n/a | • | n/a |
| | Moderate | • | • | • | • | • | • | • | n/a | • | n/a |
| | Shallow | | • | • | • | | | | | | |
| Soil Permeability | High | | | | | • | | • | n/a | n/a | n/a |
| | Moderate | • | • | • | • | • | • | • | n/a | n/a | n/a |
| | Low | • | • | • | • | • | • | • | n/a | n/a | n/a |
| Soil Erodibility | High | | • | | • | • | | | n/a | • | n/a |
| | Moderate | | • | • | • | • | • | • | n/a | • | n/a |
| | Low | • | • | • | • | | • | • | n/a | | n/a |
| Soil Strength | Moderate | • | • | • | • | • | • | n/a | n/a | • | n/a |
| | Low | n/a | | • | | • | • | n/a | n/a | | n/a |
| Moisture | Sub-surface | • | • | | • | • | • | • | • | • | • |
| | Surface | | • | • | • | • | • | | | | |
| Surficial Erosion | - | • | • | • | • | • | • | | | • | |
| Mass Movement | Shallow | • | • | • | | • | • | • | • | • | • |
| | Moderate | | | | | • | | • | • | • | • |

Legend:
• Recommended soil bioengineering measures
n/a Not applicable

Notes:
(1) The above is extracted from Gray & Sotir (1996).
(2) Tension crack repair and berm construction are modified soil bioengineering measures in form of live stake and pole drain respectively.

**Figure C.1:** "Suitability of Different Soil Bioengineering Measures for Slopes Based on Soil and Site Conditions", modified from Campbell et al. (2008).

## C.2. Flux target derivation, injection experiment

The target inflow rate of approximately 250 L/h was determined based on four considerations: estimated system storage capacity, practical time constraints, observed rainfall precedents, and plausible preferential flow velocities through the bundle.

### C.2.1. Storage capacity

Laboratory tests conducted by Cahill (2024) indicate mean porosities of 0.60 for the planting soil and 0.35 for sand. According to the design overview, the system incorporates 13.1 $m$ of sand and 3.275 $m$ of loam in a 1:4 loam-to-sand ratio. Based on these porosities, the storage capacities are approximately 4.6 $m$ in the sand layer and 2.0 $m^3$ in the planting soil, yielding a total potential storage of approximately 6,600 litres under full saturation.

As the soil was expected to be at field capacity at the start of the experiment, the effective available storage is reduced. Assuming an additional storage capacity between field capacity and saturation of 0.20 for sand and 0.28 for loam, the available storage at the start of the experiment is estimated at approximately 3,500 litres for the full system. The width of a single dead bundle is 30 cm, representing 20 % of the total system width. Accordingly, the sand layer beneath one bundle can store approximately 0.5 $m$ between field capacity and saturation. Across the three bundles, covering twice the width of a single bundle, this equates to roughly 1,000 litres of available storage.

For comparison, Boerlijst (2025) reported an outflow of 80 $L$ from a total inflow of 573 $L$, implying storage of 493 $L$. This lower value likely reflects a wetter initial condition in their setup, where the soil was not at field capacity. The soil moisture sensors installed in the current experiment allow a more precise estimation of pre-experimental storage conditions.

### C.2.2. Rainfall comparison

A rainfall event on 04/10/25 delivered approximately 300 $mm$ over three days, equivalent to 3,600 litres on the slope and 1,080 litres directly on the 60 $cm$ bundle, producing measurable outflow through the drainage bundle. This observation provides empirical confirmation that drainage responses can be expected once cumulative inflow exceeds approximately 1,000 litres.

### C.2.3. Preferential flow velocities

Nimmo (2021) report that field-observed preferential flow velocities typically range from $10^{-4}$ to $310^3$ m/s across a wide variety of soils and transport conditions, with velocities exceeding $10^{-2}$ $m/s$ being uncommon. For a bundle diameter of 30 $cm$ with approximately 40% void space, these velocities correspond to flow rates of between 10 and 288 $L/h$ through the bundle matrix.

### C.2.4. Target flux

To complete the experimental procedure within a single working day, water application was limited to four to five hours, leaving sufficient time for drainage observation. Considering the storage capacity estimate of approximately 1,000 litres, the rainfall precedent, and the upper range of plausible preferential flow rates, a target inflow rate of approximately 250 $L/h$ was selected. This value lies near the upper bound of observed preferential flow rates while remaining practical within the experimental timeframe. Over a 4–5 hour application period, this rate delivers 1,000–1,250 $L$, which is sufficient to exceed the estimated storage capacity and induce measurable drainage.

## C.3. Calculation of flux from tank drawdown injection and irrigation experiment

First-order polynomials were fitted to the daily irrigation drawdown, assuming a constant cross-section and constant pump capacity. Nightly irrigation was assumed to decrease exponentially; therefore, second-order polynomials were fitted to the nightly drawdown $mH_2O$ pressure data. $R^2$ was used as a fit metric and shown in Figure C.6, indicating consistent good fits ($R^2 > 0.995$).

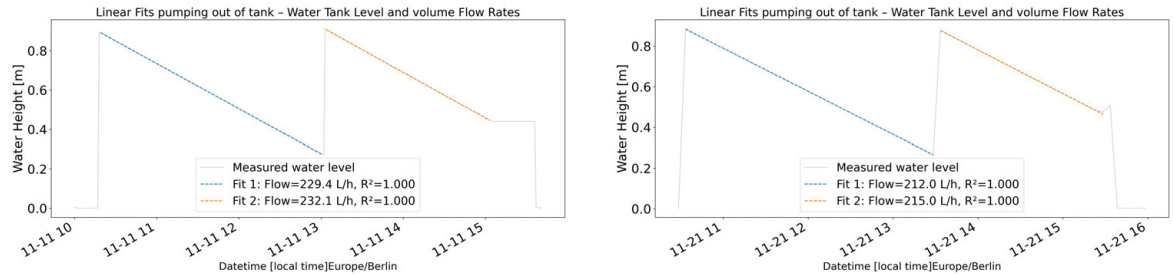



**Figure C.2:** Water height tanks runs one and two, with derived pumping flux.

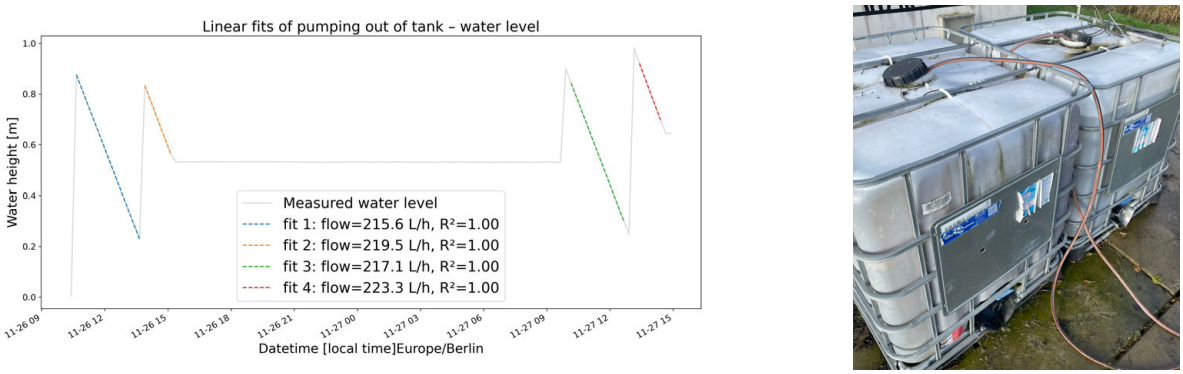



**Figure C.3:** Water height tanks run 3 and 4, with derived pumping fluxes (left) and water supply tanks ($1m^3$) with pressure sensor (right).

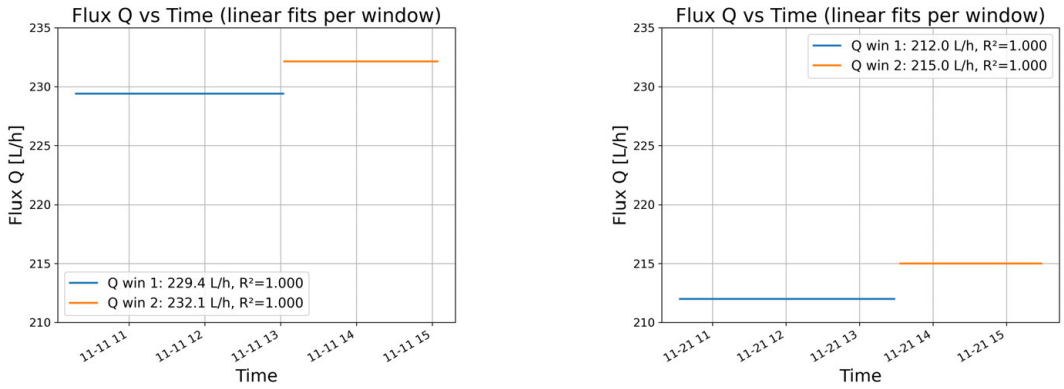



**Figure C.4:** Flux out of tank during experiment run 1.1 and 1.2.

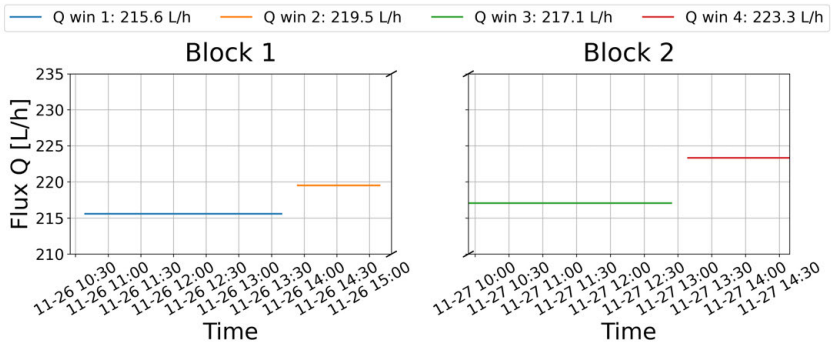



**Figure C.5:** Flux out of tank during experiment run 1.3 and 1.4.

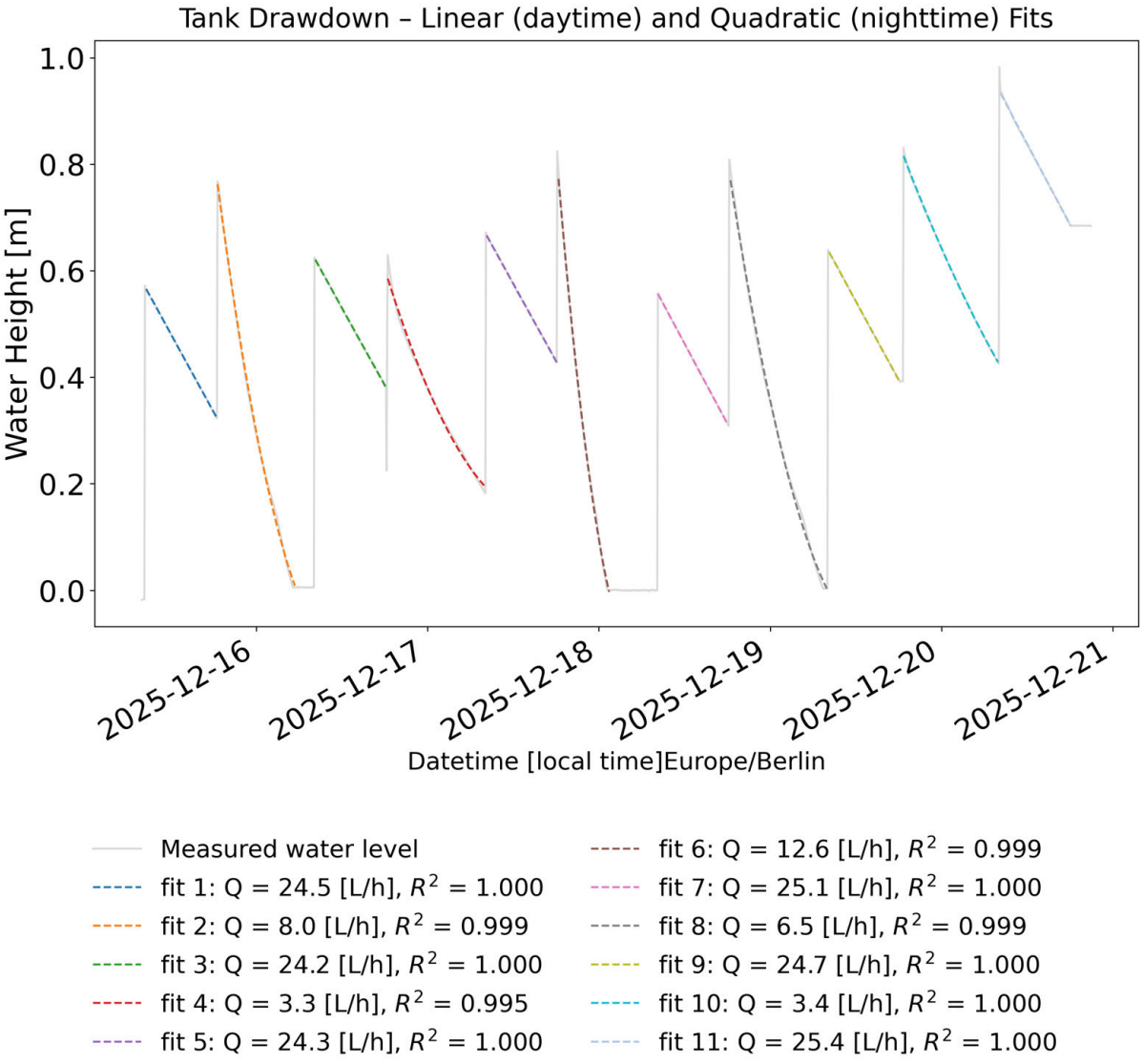



**Figure C.6:** Polynomial fits to tank drawdown $mH_2O$ $(mm)$ measurements, with $R^2$ as fit metric.

## C.4. Check absolute values soil moisture

The volumetric soil-moisture values measured in this study were lower than expected, ranging from 0.025 to 0.20, even under extreme wetting conditions involving the pumping of several thousand litres of water. Under such conditions, saturation of the sand layer would normally be anticipated. Laboratory tests indicate a porosity of 0.32 (Cahill, 2024), which implies a higher potential volumetric water content than observed in the field. As shown in Figure C.7, the recorded values are consistent with soil-moisture data collected by F. Berlitz during a long-term monitoring campaign. The long-term dataset by F. Berlitz was recorded between January 2024 and January 2026 at 15-minute intervals, whereas the present study covers November–December 2025 with a 1-minute sampling interval. These data originate from the sensor installed at a depth of 50 cm on the top of the slope, as shown in Figure E.2, thereby increasing confidence in the reliability and comparability of the measurements obtained in the present study.

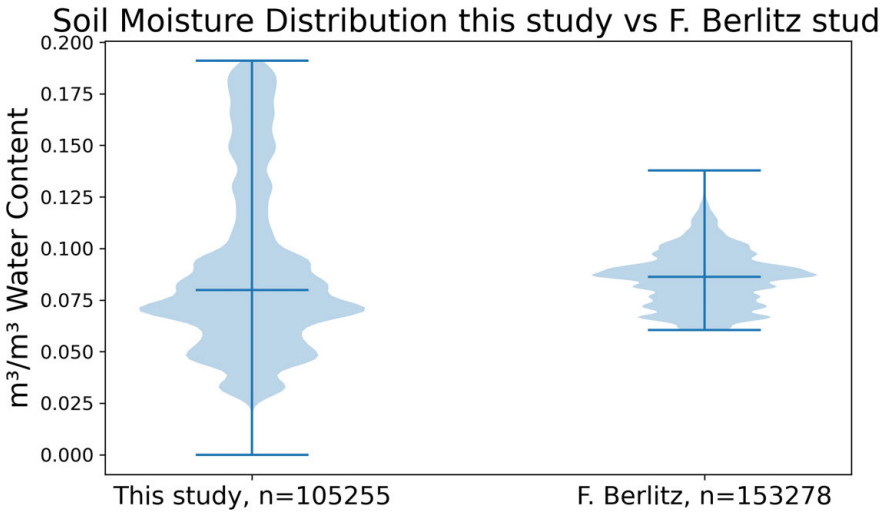



**Figure C.7:** A comparison between the soil-moisture values from this study compared to the long-term monitoring soil-moisture values by long-term measurement campaign F. Berlitz.

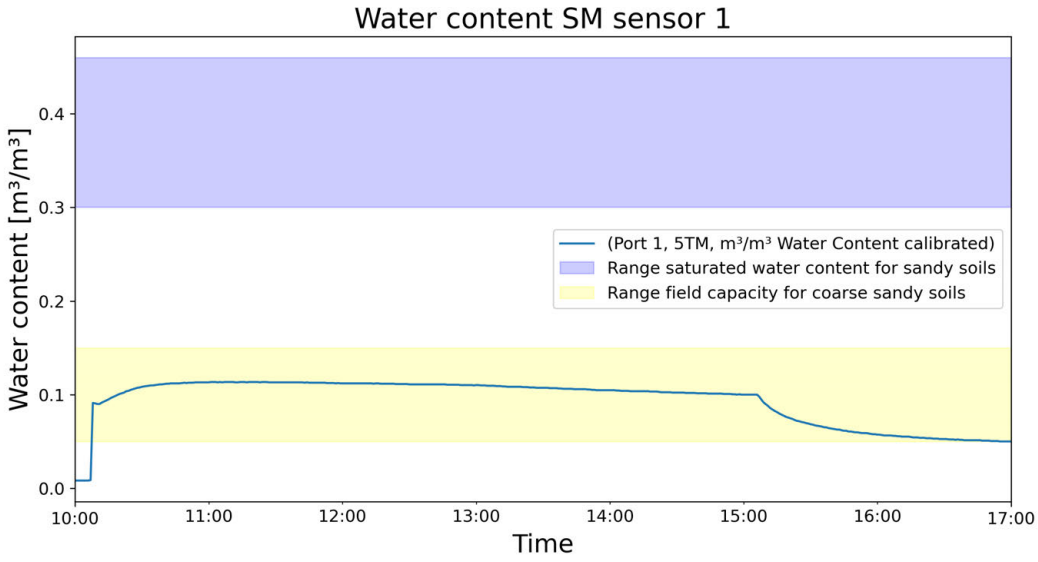



**Figure C.8:** Soil moisture readings sensor 1, run 1, compared to common values of sandy soils for full saturation and field capacity.

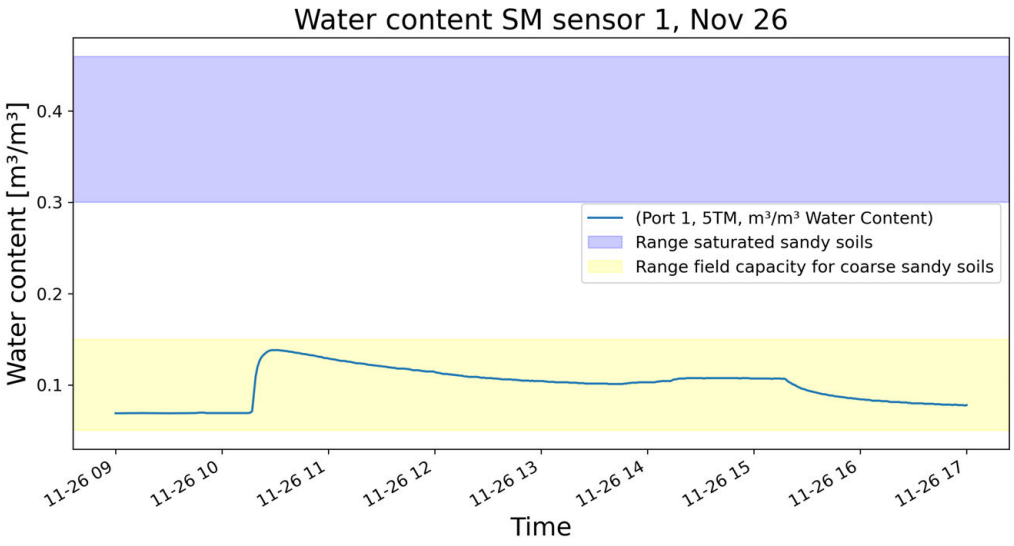



**Figure C.9:** Soil moisture readings sensor 1, run 3, compared to common values of sandy soils for full saturation and field capacity.

## C.5. cumulative fluxes sustained irrigation experiment

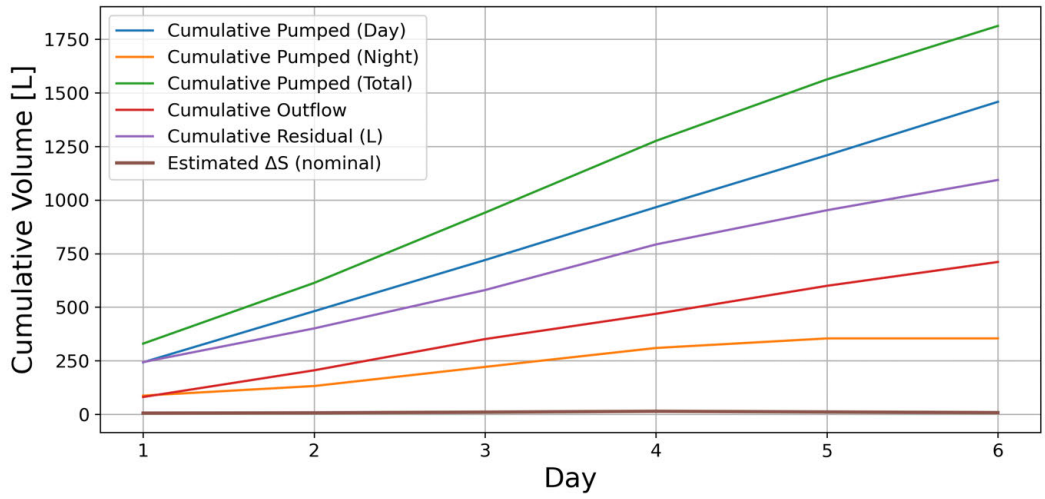
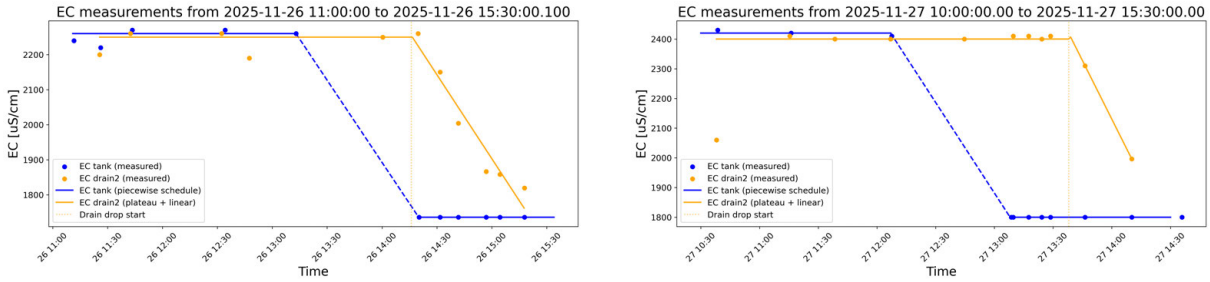



**Figure C.10:** Cumulative volumes water balance irrigation experiment

## C.6. Salt tracer breakthrough irrigation experiment

### C.6.1. breakthrough

The hydraulic breakthrough of irrigation water was consistently observed after approximately 45 min, and flow ceased within 10–20 min following the termination of pumping. Salt tracer experiments conducted during runs 1.3 and 1.4 indicated EC response times on the order of 60–80 min, shown in Figure C.11. This delay likely relates to ”old” water effects (Weiler & McDonnell, 2007). Given the small number of EC samples and their irregular, relatively coarse temporal spacing, the tracer experiment primarily provides an order-of-magnitude indication of breakthrough timing. Within this context, the tracer-derived response times are considered broadly consistent with the drain 2 breakthrough observations.




**(a)** Salt tracer test, with random sampling, on 26 November 2025.

**(b)** Salt tracer test, with random sampling, on 27 November 2025.

**Figure C.11:** Salt tracer tests during run 1.3 and run 1.4 of injection experiment, with .

## C.7. Observed response (time) after excavating the bottom of the slope

Figure C.12 presents this response using a time-lapse recording with one frame captured every 4 seconds. Water was observed entering the excavated hole after approximately 24 minutes, corresponding to the interval $12 \times 120/60 = 24$ minutes calculated from the time-lapse sequence. In comparison, flow through drain 2 began around 46 minutes after the start of pumping, consistent with the timing recorded by the pressure sensor in the drain (start pumping: 10:45 h; sensor detection: 11:33 h). During this period, the preferential flow along the plastic underlay appeared evenly distributed, with no evidence of localised preferential channels or discrete breakthrough points.

## C.8. Sensitivity analysis of estimated representative area soil-moisture sensors

Representative area is presented in Figure 5.7, and the representative widths for the uncertainty bands are $w_{min} = 0.1$ m, $w_{nom} = 0.3$ m, $w_{max} = 0.5$ m. ($L = 0.65$ m and $z = 0.6$ m.)

**Table C.1:** Daily and cumulative change in soil water storage

| Date | $\Delta S_{nom}$ [L] | $\Delta S_{lo}$ [L] | $\Delta S_{hi}$ [L] | Cum.$_{nom}$ [L] | Cum.$_{lo}$ [L] | Cum.$_{hi}$ [L] |
|---|---|---|---|---|---|---|
| 2025-12-16 | +5.6 | +1.9 | +9.3 | +5.6 | +1.9 | +9.3 |
| 2025-12-17 | +1.4 | +0.2 | +2.5 | +7.0 | +2.3 | +11.6 |
| 2025-12-18 | +3.3 | +0.9 | +5.7 | +10.3 | +3.4 | +17.1 |
| 2025-12-19 | +3.9 | +1.3 | +6.5 | +14.2 | +4.7 | +23.6 |
| 2025-12-20 | −3.2 | −5.3 | −1.1 | +11.0 | +3.7 | +18.4 |
| 2025-12-21 | −3.1 | −5.1 | −1.0 | +7.9 | +2.6 | +13.2 |
| 2025-12-22 | −0.1 | −0.2 | −0.1 | +7.8 | +2.6 | +13.0 |

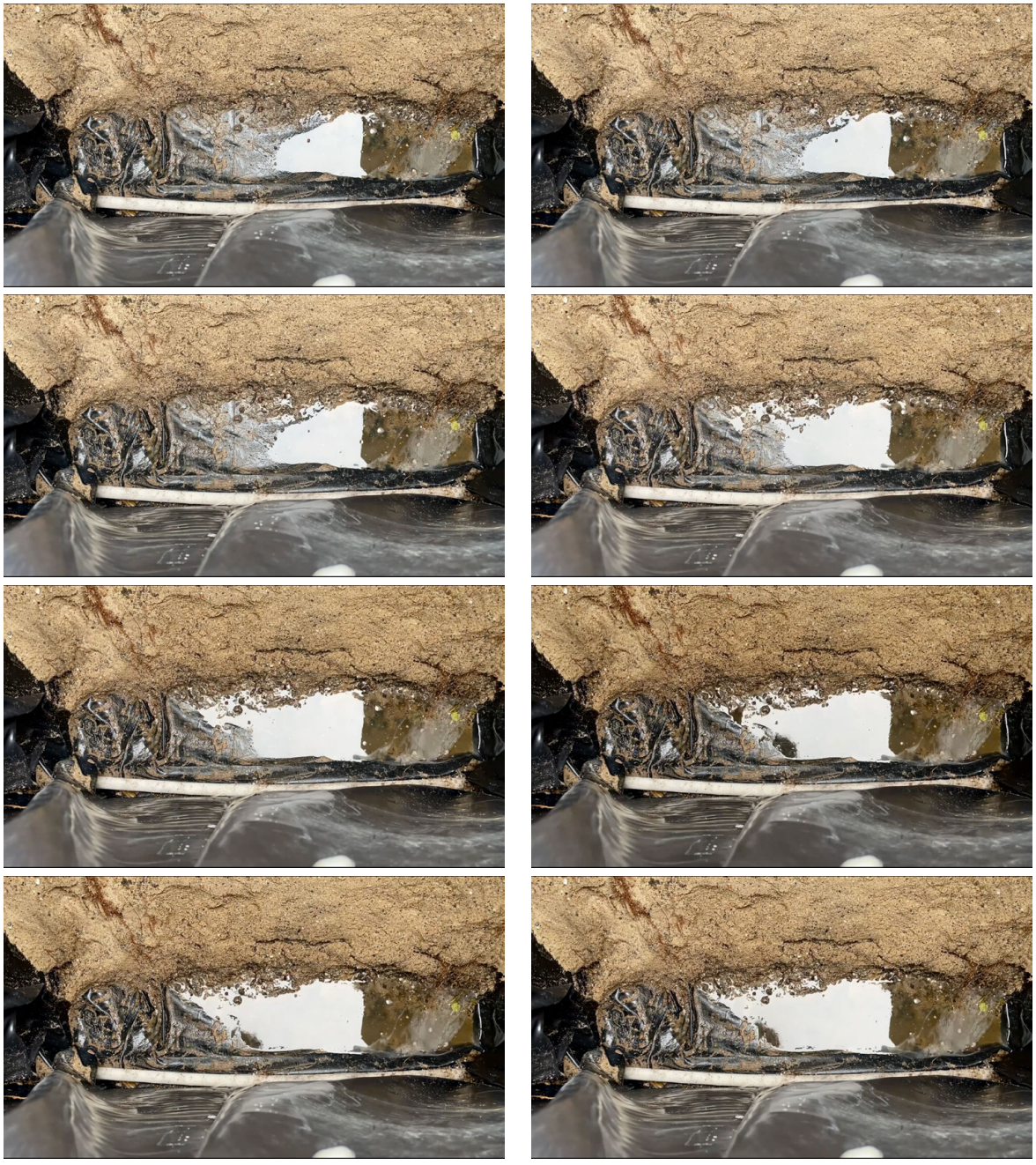


**Figure C.12:** Stills from time-lapse response to pumping in dead bundle.

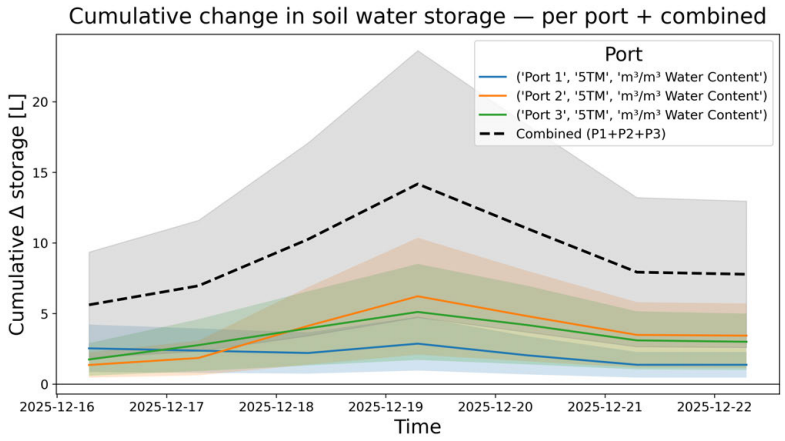



**Figure C.13:** Cumulative storage at sensors and combined, with bands for choice of representative area around sensors

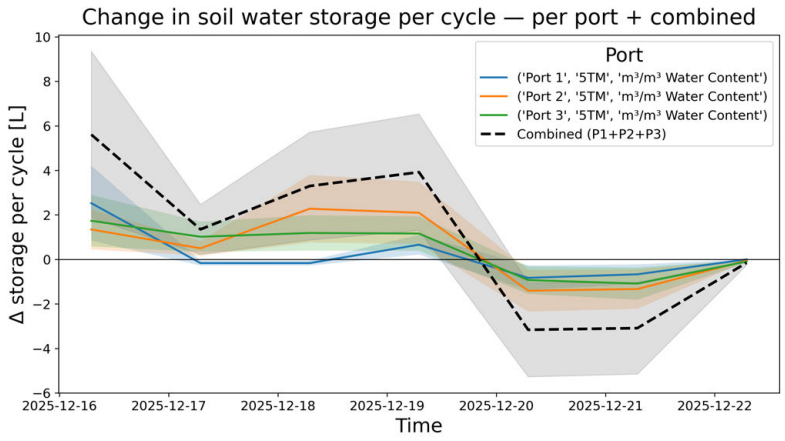



**Figure C.14:** Delta storage per day at sensors and combined, with bands for choice of representative area around sensors

## C.9. Log-normal distribution of hydraulic conductivity values experiment 3

Given the limited number of measurements, no strong conclusions can be drawn about the underlying distribution. That said, the data does not contradict the log-normal distribution assumed here, which is consistent with what is commonly reported in literature (Angulo-Jaramillo et al., 2016), (Watson & Luxmoore, 1986).

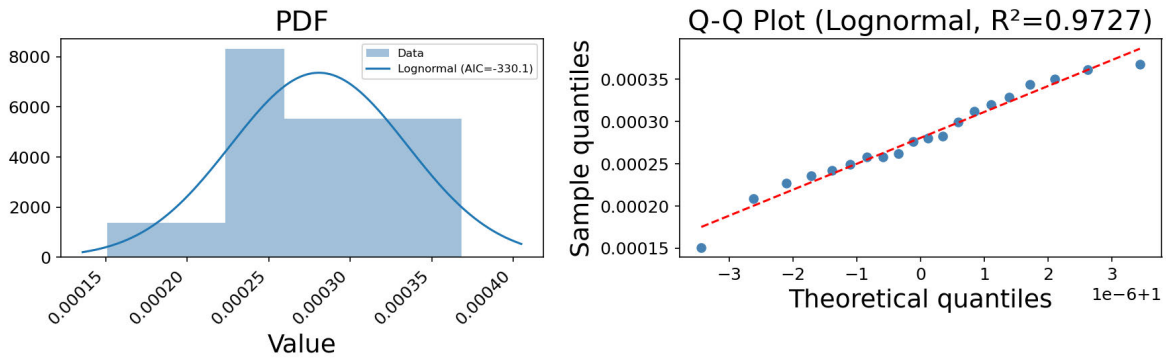



**Figure C.15:** Log-normal distribution fits over measured bare slope data.

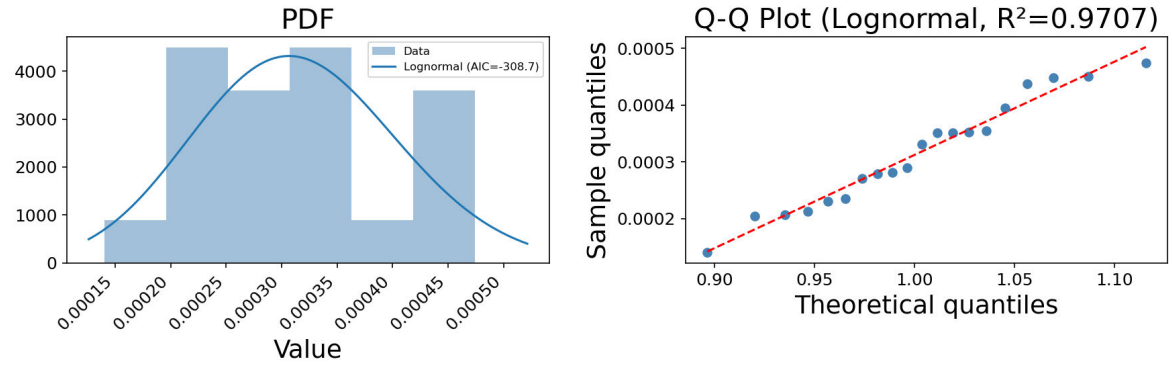



**Figure C.16:** Log-normal distribution fits over measured LPD slope data.

## C.10. Log PDF experiment 3 distribution

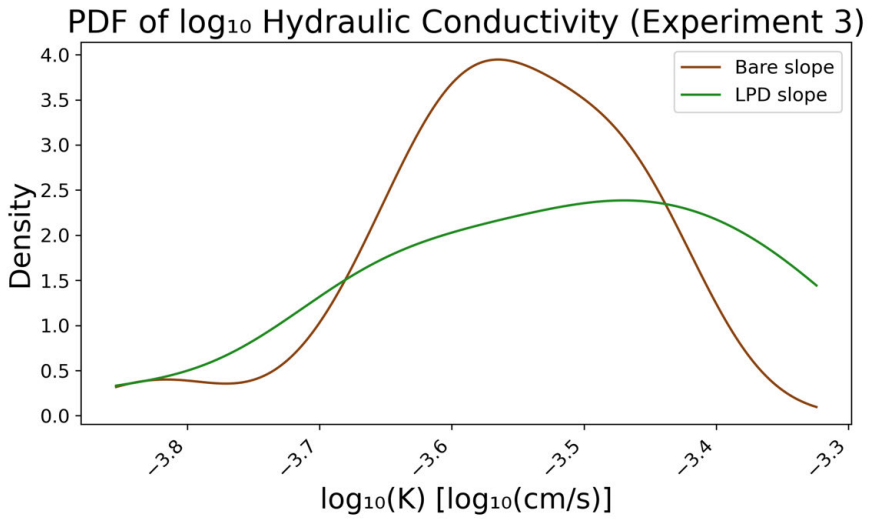



**Figure C.17:** PDF of the log estimated hydraulic conductivity during the infiltrometer experiment

## C.11. Sample choice sensitivity in lumped infiltrometer box plots

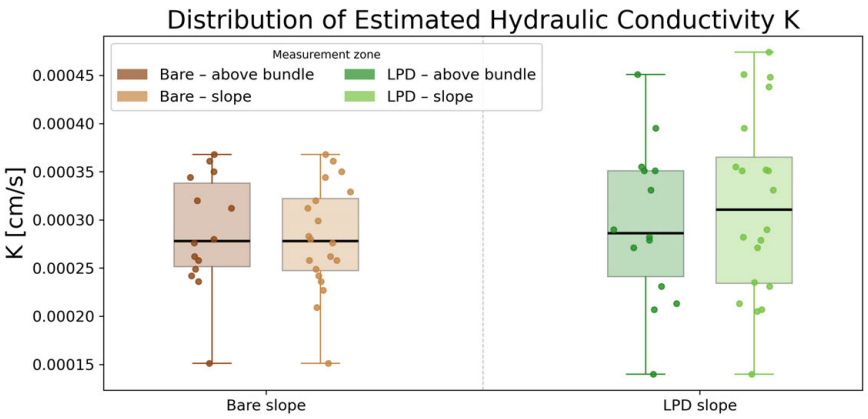



**Figure C.18:** Distribution comparison between the estimated hydraulic conductivity measurements on the LPD and bare slope. Both are plotted with and without the measurement points furthest away from the live bundle. Which were observed in Figure 6.3 to mainly show the increased upper tail variation.

## C.12. MODFLOW model setup

The model solves the 2-D saturated groundwater flow equation in a vertical $x$–$z$ cross-section using MODFLOW-NWT with the Upstream Weighting (UPW) package and Newton–Raphson solver, which together provide robust convergence for partially saturated cells (Niswonger et al., 2011). The domain is a single-row, unit-width slice discretised into 100 columns of $\Delta x = 0.06\,\mathrm{m}$ (total length $6\,\mathrm{m}$), with four isotropic, unconfined layers: soil ($0.50\,\mathrm{m}$, $K = 0.27\,\mathrm{m/d}$), a thin interface layer ($0.20\,\mathrm{m}$), sand ($0.65\,\mathrm{m}$), and a gravel base layer ($0.10\,\mathrm{m}$, $K = 1000\,\mathrm{m/d}$). Recharge of $q_R = 0.300\,\mathrm{m/d}$ is applied to the upslope $1\,\mathrm{m}$ of the top surface, representing $300\,\mathrm{L}$ irrigated over $1\,\mathrm{m}^2$ similar to the irrigation experiment. The upslope and downslope boundaries are no-flow walls, with two MODFLOW drain cells at the downslope end, placed at the bottom of the interface and gravel layers to represent the PVC collection drains; drain conductance is set deliberately high ($C_d = 100\,\mathrm{m}^2/\mathrm{d}$), mimicking free-flowing drains. The model is run as a transient to an effective steady state ($1000\,\mathrm{d}$, 100 time steps, multiplier 1.5).

A parameter sweep is performed over slope angle $\alpha \in \{1, 5, 10, 15, 20, 30, 40\}°$, sand conductivity $K_{\mathrm{sand}} \in \{10, 1, 0.1, 0.01, 0.001\}\ \mathrm{m/d}$, and interface conductivity $K_{\mathrm{interface}} \in \{5, 15, 35\}\ \mathrm{m/d}$. The primary output metric is the lateral diversion ratio, $R_{\mathrm{div}} = Q_{\mathrm{interface\ drain}}/(Q_{\mathrm{interface\ drain}} + Q_{\mathrm{sand\ drain}})$, extracted from the MODFLOW cell-budget file, where $R_{\mathrm{div}} = 1$ indicates all water exits through the interface layer and $R_{\mathrm{div}} = 0$ indicates full infiltration into the sand.

### C.12.1. Schematisation model setup

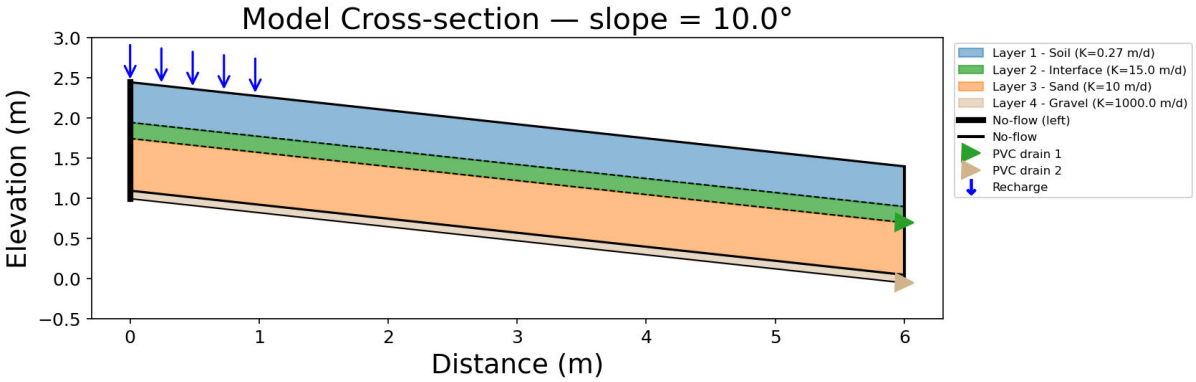



**Figure C.19:** MODFLOW-NWT model schematisation

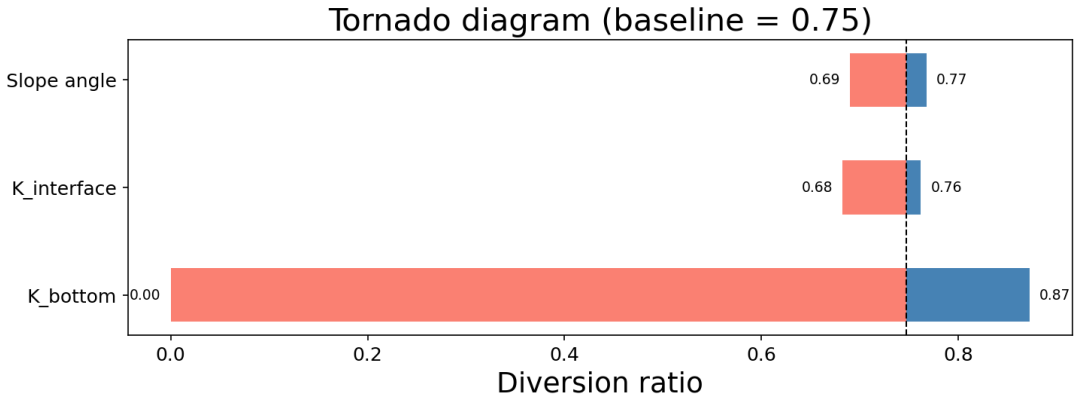



**Figure C.20:** Tornado diagram MODFLOW-NWT

## C.12.2. Python code MODFLOW-NWT configuration

In [2]:
```python
# Parameters
slope_angle_deg = 10.0
k_upper = 0.27                # upper soil [m/d]
k_interface = 15.0            # interface layer — isotropic K [m/d]; sensitivity sweep uses [5, 15, 35]
k_lower = 10                  # sand [m/d]
k_gravel = 1000.0              # gravel layer [m/d]
recharge_rate = 0.300

length = 6.0
thickness_upper = 0.50        # soil
thickness_interface = 0.20    # thin interface layer
thickness_lower = 0.65       # sand
thickness_gravel = 0.10      # gravel layer


# Grid
nlay = 4
nrow = 1
ncol = 100
delr = length / ncol
delc = 1.2

x_centers = np.arange(ncol) * delr + delr / 2.0
slope = np.tan(np.radians(slope_angle_deg))
base_elev = 1.0

# Layer elevations
total = thickness_upper + thickness_interface + thickness_lower + thickness_gravel
top = (base_elev + total - slope * x_centers).reshape(nrow, ncol)
botm_1 = base_elev + thickness_interface + thickness_lower + thickness_gravel - slope * x_centers
botm_2 = base_elev + thickness_lower + thickness_gravel - slope * x_centers
botm_3 = base_elev + thickness_gravel - slope * x_centers
botm_4 = base_elev - slope * x_centers
botm = np.array([botm_1, botm_2, botm_3, botm_4]).reshape(nlay, nrow, ncol)

# K arrays — isotropic (vka = hk)
hk = np.zeros((nlay, nrow, ncol))
hk[0, :, :] = k_upper
hk[1, :, :] = k_interface
hk[2, :, :] = k_lower
hk[3, :, :] = k_gravel

vka = hk.copy()
```

**Figure C.21:** Parameter definition MODFLOW-NWT setup in Python.

In [3]:

```python
# Parameter sweep: slope angle vs K_sand
# Closed left boundary (experimental setup)

sweep_angles  = [1, 5, 10, 15, 20, 30, 40]
sweep_k_lower = [10, 1, 0.5, 0.1, 0.05, 0.01, 0.005]
k_interface_values = [5, 15, 35]

model_ws = 'model_runs/closed4L'
os.makedirs(model_ws, exist_ok=True)

na, nk, nki = len(sweep_angles), len(sweep_k_lower), len(k_interface_values)
all_infiltration      = np.full((nki, na, nk), np.nan)
all_lateral_interface = np.full((nki, na, nk), np.nan)

n_rch = int(np.ceil(1.0 / delr))
recharge_array = np.zeros((nrow, ncol))
recharge_array[:, :n_rch] = recharge_rate
total_recharge = recharge_rate * n_rch * delr * delc

drn_eps = 1e-4
drn_conductance = 100.0

for ki, k_int in enumerate(k_interface_values):
    print(f"\n=== K_interface = {k_int} m/d (isotropic) ===")

    for i, angle in enumerate(sweep_angles):
        for j, kl in enumerate(sweep_k_lower):
            s = np.tan(np.radians(angle))
            total_thick = thickness_upper + thickness_interface + thickness_lower + thickness_gravel
            t  = (base_elev + total_thick - s * x_centers).reshape(nrow, ncol)
            b1 = base_elev + thickness_interface + thickness_lower + thickness_gravel - s * x_centers
            b2 = base_elev + thickness_lower + thickness_gravel - s * x_centers
            b3 = base_elev + thickness_gravel - s * x_centers
            b4 = base_elev - s * x_centers
            bm = np.array([b1, b2, b3, b4]).reshape(nlay, nrow, ncol)

            hk_s = np.zeros((nlay, nrow, ncol))
            hk_s[0, :, :] = k_upper
            hk_s[1, :, :] = k_int
            hk_s[2, :, :] = kl
            hk_s[3, :, :] = k_gravel
            vka_s = hk_s.copy()

            strt_s = np.zeros((nlay, nrow, ncol))
            for lay in range(nlay):
                strt_s[lay, 0, :] = bm[lay, 0, :] + 0.01

            drn_s = {0: [
                [1, 0, ncol - 1, bm[1, 0, ncol - 1] + drn_eps, drn_conductance],
                # [2, 0, ncol - 1, bm[2, 0, ncol - 1] + drn_eps, drn_conductance],
                [3, 0, ncol - 1, bm[3, 0, ncol - 1] + drn_eps, drn_conductance],
            ]}

            name = f'sweep_ki{ki}_a{angle}_k{j}'
            m = fp.modflow.Modflow(name,
                           exe_name='/Users/lucasdeleeuw/Documents/MODFLOW/bin/mfnwt',
                           version='mfnwt',
                           model_ws=model_ws)

            fp.modflow.ModflowDis(m, nlay=nlay, nrow=nrow, ncol=ncol,
                          delr=delr, delc=delc, top=t, botm=bm,
                          nper=1, perlen=[1000.0], nstp=[100], tsmult=[1.5],
                          steady=[False])
            fp.modflow.ModflowBas(m, ibound=np.ones((nlay, nrow, ncol), dtype=int), strt=strt_s)
            fp.modflow.ModflowUpw(m, hk=hk_s, vka=vka_s, ipakcb=53,
                           laytyp=[1, 1, 1, 1], ss=1e-5, sy=0.2)
            fp.modflow.ModflowRch(m, rech=recharge_array)
            fp.modflow.ModflowDrn(m, stress_period_data=drn_s, ipakcb=53)
            fp.modflow.ModflowNwt(m, headtol=1e-2, fluxtol=1000,
                           maxiterout=500, options='COMPLEX')
            fp.modflow.ModflowOc(m, stress_period_data={(0, 99): ['save head', 'save budget']},
                          compact=True)

            m.write_input()
            ok, _ = m.run_model(silent=True)

            if ok:
                c = fp.utils.CellBudgetFile(os.path.join(model_ws, f'{name}.cbc'))
                drn_cbc = c.get_data(text='DRAINS')[-1]
                Q_interface_drain = 0.0
                Q_sand_drain      = 0.0
                for rec in drn_cbc:
                    lay = (rec['node'] - 1) // (nrow * ncol)
                    if lay == 1:
                        Q_interface_drain += abs(rec['q'])
                    elif lay == 3:
                        Q_sand_drain += abs(rec['q'])

                all_infiltration[ki, i, j]      = Q_sand_drain      / total_recharge
                all_lateral_interface[ki, i, j] = Q_interface_drain / total_recharge

            inf   = f"{all_infiltration[ki,i,j]:.2f}"      if not np.isnan(all_infiltration[ki,i,j])      else "FAIL"
            lat_i = f"{all_lateral_interface[ki,i,j]:.2f}" if not np.isnan(all_lateral_interface[ki,i,j]) else "FAIL"
            print(f"  {angle:2d}°  K_sand={kl:8.3f}  sand_drain={inf}  interface_drain={lat_i}")
```

**Figure C.22:** Parameter sweep MODFLOW-NWT model setup in Python.

# D

# Fieldwork photo logbook

## D.1. OAL setup



**Figure D.1:** Photo showing surface vegetation before the start of this study, 24/09/25



**Figure D.2:** Closer look at surface vegetation before the start of this study, 24/09/25



**Figure D.3:** Sprouting of slope one 07/10/25



**Figure D.4:** Covered slope one 07/10/25



**Figure D.5:** Dug hole at top end of bundles 13/10/25



**Figure D.6:** Filling of tank with submersible pump, pumping from the surface of the ditch to limit sediment intake, 10/12/25



**Figure D.7:** Ponds on covered slope after heavy rainfall, 21/10/25

## D.2. Point injection into bundles experiment

| Date | Activity |
|---|---|
| 11/11/2026 | 10:06 start injection experiment run 1, 15:06 stopped pumping |
| 21/11/2026 | 10:23 start injection experiment run 2, 15:23 stopped pumping |
| 26/11/2026 | 10:14 start injection experiment run 3, 15:16 stopped pumping |
| 27/11/2026 | 09:50 start injection experiment run 4, 14:40 stopped pumping |

**Figure D.8:** Point injection experiment runs with dates



**Figure D.9:** No flow observed alongside drain 2 during run 1.1, 11/11/25



**Figure D.10:** Frost observed in the morning of run 1.2, 21/11/25



**Figure D.11:** Slight regrowth of willow observed on 24/11/25

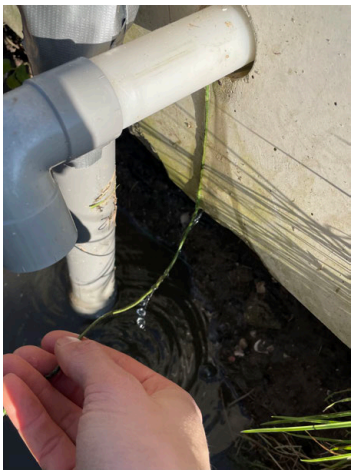


**Figure D.12:** Flow alongside drain 2, during injection experiment, run 2 on 21/11/25



**Figure D.13:** Observed leak, 16-12-25



**Figure D.14:** After finishing Experiment 1, the distributed inlet hose was observed to be filled with algae, covering all holes, 03/12/25



**Figure D.15:** PVC tube below ground level with risk of submergence, 12/12/25



**Figure D.16:** Leakage hole, 02/12/25



**Figure D.17:** Excavated bundle, 10/12/25

## D.3. Sustained distributed irrigation experiment

| Date | Activity |
|---|---|
| 15/12/2026 | 08:32 Start irrigation experiment 18:37 switched to nightly irrigation |
| 16/12/2026 | 08:13 Start irrigation experiment 18:13 switched to nightly irrigation |
| 17/12/2026 | 08:09 Start irrigation experiment 18:09 switched to nightly irrigation |
| 18/12/2026 | 08:14 Start irrigation experiment 18:15 switched to nightly irrigation |
| 19/12/2026 | 08:05 Start irrigation experiment 18:06 switched to nightly irrigation |
| 20/12/2026 | 08:05 Start irrigation experiment 18:06 switched to nightly irrigation |

**Figure D.18:** Irrigation experiment with dates



**Figure D.19:** Tapered top of nightly irrigation tank, 14/12/25



**Figure D.20:** Bottom of nightly irrigation tank filled with bricks, 16/12/25



**Figure D.21:** Shape nightly irrigation tank at setup after sunset, 15/12/25



**Figure D.22:** Drip irrigation, 14/12/25



**Figure D.23:** Nightly gravitational irrigation, 14/12/25



**Figure D.24:** Daily irrigation, 19/12/25



**Figure D.25:** Observed drip irrigation, 15/12/25



**Figure D.26:** No flow alongside drainage hole, 15/12/25



**Figure D.27:** Mushroom, 19/12/25



**Figure D.28:** Mushrooms, 12/12/25

## D.4. Mini-Disk infiltrometer experiment

| Date | Activity |
|---|---|
| 04/02/2026 | Infiltrometer experiment (cold (4degrees) little wind and slightly sunny |
| 05/02/2026 | Infiltrometer experiment (cold (2degrees) windy |

**Figure D.29:** Infiltrometer experiment with dates



**Figure D.30:** Infiltrometer test, 27/11/25



**Figure D.31:** Infiltrometers stabilised using wooden planks during the windy second day of the infiltrometer experiment, 05/02/26

# E

# Setup information

| | Planting soil | | Sand | Gravel |
|---|---|---|---|---|
| | wet sieve | dry sieve* | | |
| **d10** | <0.063 | 0.15 | 0.3 | 1.7 |
| **d50** | 0.2 | 0.5 | 0.59 | >4.75 |
| **d90** | >1.94 | >4.75 | 4.75 | >4.75 |
| **Bulk density [g/cm$^3$]** | 0.96 | | 1.81 | 1.60 |
| **Porosity [-]** | 0.64 | | 0.32 | 0.40 |
| **Organic Matter [%]** | 7% | | 0.13% | 0.20% |
| **Clay [%]** | 15% | | <0.1% | <0.1% |
| **Silt [%]** | 10% | | <0.1% | <0.1% |
| $k_{[sat]}$ **[m/s]** | 1.4e-5 | | 2e-3 | >2 |
| **Field Capacity [m$^3$/m$^3$]** | 0.2 | | 0.02 | 0.04 |

**Figure E.1:** "Selected Media properties. d10, d50, and d90: maximum diameter [mm] of passing percentage. Sand and gravel (*Note: for the planting soil, dry sieve analysis of the oven-dried sample had clumps of fines of >2 $mm$, therefore the wet sieve results are more representative)" Cahill (2024).

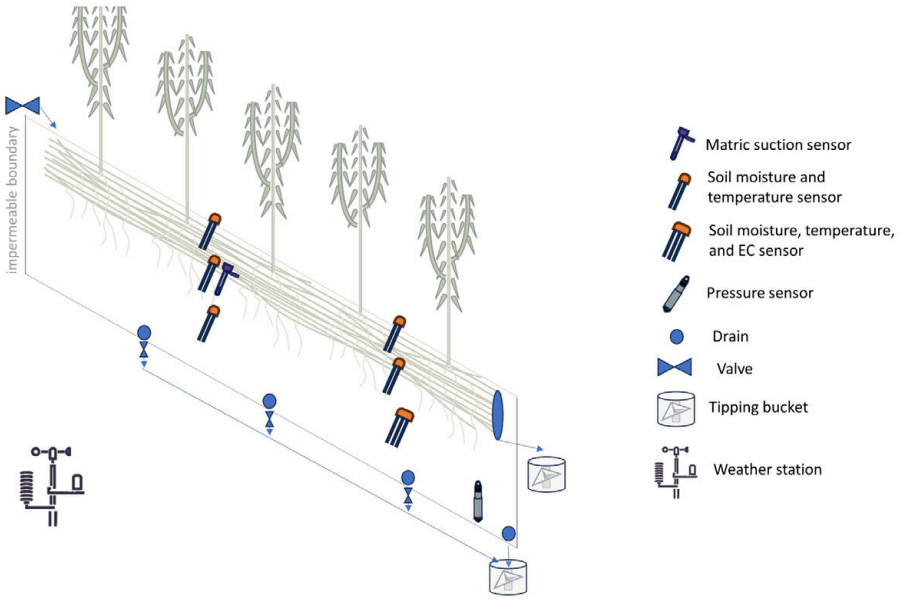



**Figure E.2:** Overview of smart-sensor placement at experimental setup (Cahill, 2024)

## E.1. Setup improvements

On 02/12/2025, the location where drainage tube 2 perforates the plastic boundary was observed to be non-water-tight, as anticipated based on the injection experiment results. However, after adding 15 $L$ of water twice, the water moved away from the observed leak, and no water moved through or around the drainage tube. Indicating the presence of another leak. The observed leakage was sealed with a 2-component epoxy rubber glue, fabric tape, and rubber sealing paste, and then closed with a 5 $cm$ layer of clay. As a precaution, a clay layer was also applied on the opposite side to seal any potential unseen holes.



**Figure E.3:** Observed leak around drain on 02/12/2025 and sealing of known and unknown punctures with clay.

Figure E.4 shows the shortened PVC drain 2, with its lowest perforation above the ground-level, in preparation for the sustained irrigation experiment to prevent submergence. This is considered feasible, as water height never exceeded the third hole during any run. It is, however, conditional on the applied flux remaining comparable to that of the injection experiment, and on the leakage pathway not being fully sealed.



**(a)** **(b)**

**Figure E.4:** PVC drain 1 (a) initially during point injection experiment, and (b) shortened for sustained irrigation experiment.